Institute of Thermoelectricity, Academy of Sciences and Ministry of Education and Science of Ukraine

Journal of THERMOELECTRICITY

International Research

Founded in December, 1993

published 6 times a year

No. 1 *2022*

Editorial Board

International Editorial Board

Founders – National Academy of Sciences, Ukraine
Institute of Thermoelectricity of National Academy of Sciences and Ministry of Education and Science of Ukraine

Certificate of state registration № КВ 15496-4068 ПР

ISSN: 1607-8829

DOI: 10.63527/1607-8829-2022-1

Address of editorial office:
Ukraine, 58002, Chernivtsi, General Post Office, P.O. Box 86.
Phone: +(380-372) 90 31 65.
Fax: +(380-3722) 4 19 17.
E-mail: jt@inst.cv.ua
http://www.jt.inst.cv.ua

Signed for publication 24.03.2022. Format 70×108/16. Offset paper №1. Offset printing.
Printer's sheet 11.5. Publisher's signature 9.2. Circulation 400 copies. Order 5.

Printed from the layout original made by "Journal of Thermoelectricity" editorial board
in the printing house of "Bukrek" publishers,
10, Radischev Str., Chernivtsi, 58000, Ukraine

CONTENTS

DOI: 10.63527/1607-8829-2022-1-5-17

A.O. Snarskii

A.O. Snarskii , D.Sc (Phys-Math)*, Prof.*
V.V. Fedotov, senior lecturer

National Technical University of Ukraine "Igor Sikorsky Kyiv Polytechnic Institute",
37 Peremohy Prosp.,
Kyiv, 03056, Ukraine,
e-mail: asnarskii@gmail.com

V. V. Fedotov

THERMOELECTRIC COMPOSITES WITH DIFFERENT PERCOLATION THRESHOLDS

A modification of the mean-field approximation is considered for describing the behaviour of effective kinetic coefficients, including for thermoelectric composites. The proposed modification makes it possible to describe randomly heterogeneous media with different percolation thresholds at arbitrary values of local kinetic coefficients. Bibl. 16, Fig. 6.

Key words: thermoelectric composites, kinetic coefficients.

Introduction

The widely used mean-field approximation (Bruggeman-Landauer approximation, self-consistent approximation) [1 – 6] has a drawback. It does not allow describing media with different thresholds. In [7], a term (Sarychev-Vinogradov term, SV-term, SVt) was introduced in the Bruggeman-Landauer approximation, which allows obtaining concentration dependences of effective galvanomagnetic coefficients for media with a predetermined percolation threshold. In [8 – 10], this approach was used to describe magneto-elastomers, and the concept of moving percolation threshold was introduced. In [11], SVt was used to describe thermoelectric phenomena in randomly heterogeneous media, but the case of "normal" and "abnormal" local kinetic coefficients [12] had to be considered separately.

This paper proposes a generalization of the SVt term for the description of kinetic phenomena in randomly heterogeneous media with any percolation threshold and for any («normal» and abnormal») values of local kinetic coefficients.

The problem of percolation threshold in the mean-field approximation in the single-flow case (by the example of effective conductivity)

For a single-flow case, for example, the case of conductivity, when there is one thermodynamic flow – electric current density $\mathbf{j}$, one thermodynamic force – electric field intensity $\mathbf{E}$, which are related by the Ohm law

$$\mathbf{j} = \sigma \mathbf{E}\,. \tag{1}$$

Effective conductivity σ_e is determined as

$$\langle \mathbf{j} \rangle = \sigma_e \langle \mathbf{E} \rangle, \tag{2}$$

where $\langle ... \rangle = 1/V \int ...dV$ is volume average and in the case of a two-phase medium

$$\sigma(\mathbf{r}) = \begin{cases} \sigma_1, \mathbf{r} \in O_1 \\ \sigma_2, \mathbf{r} \in O_2 \end{cases}, \tag{3}$$

The Bruggeman-Landauer approximation has the form

$$\frac{\sigma_e - \sigma_1}{2\sigma_e + \sigma_1} p + \frac{\sigma_e - \sigma_2}{2\sigma_e + \sigma_2}(1-p) = 0\,, \tag{4}$$

The concentration dependence according to (4) is given in Fig.1

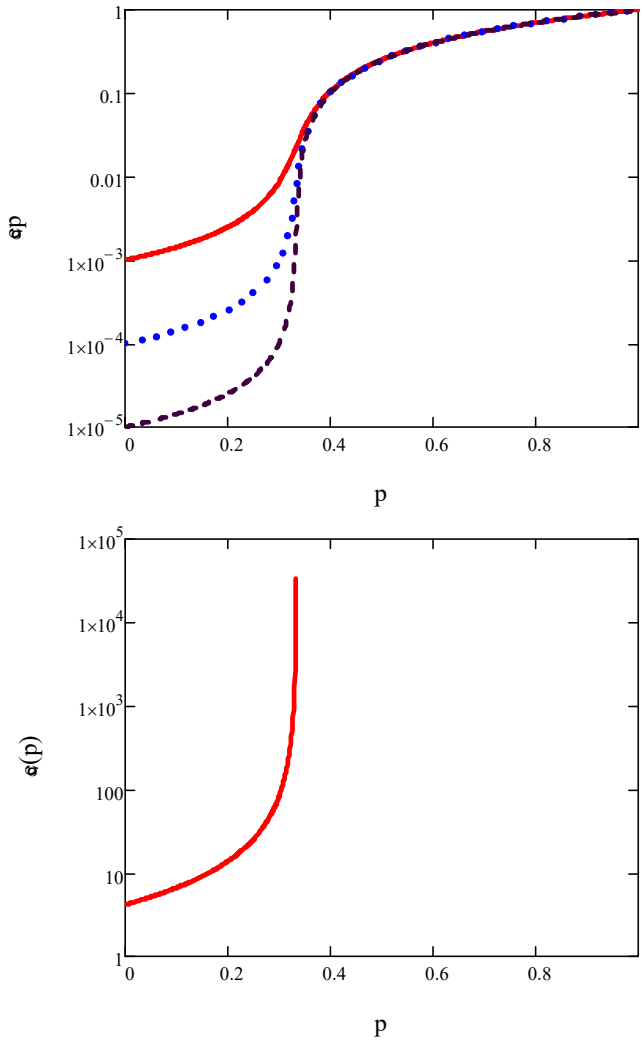

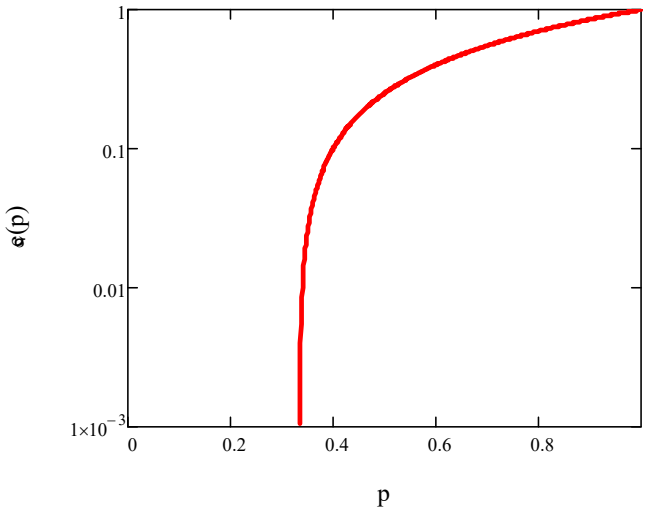

Fig. 1. Concentration behaviour of effective conductivity
a – final conductivity ratio,
b,c – percolation

Due to great heterogeneity $\sigma_1/\sigma_2 \to \infty$, the so-called percolation concentration range $|p-p_c| \ll 1$ stands out, for which the percolation dependences are valid [1,2,4], see Fig. 1

$$\sigma_e = \begin{cases} \sigma_1 (p_c - p)^{-t}, p < p_c \\ \left(\sigma_1^q \sigma_2^t\right)^{1/t+q}, |p-p_c| \ll \Delta, \\ \sigma_2 (p - p_c)^q, p > p_c \end{cases} \quad (5)$$

where $\Delta = (\sigma_2/\sigma_1)^{1/t+q}$.

It should be noted that percolation regularities are valid only for very large heterogeneity and in a very narrow concentration ($|p-p_c| \ll 1$) range. However, the numerical value of the percolation threshold is a characteristic of the entire concentration range and thus a characteristic of the behaviour of the effective kinetic coefficients in the entire concentration range and at any heterogeneity.

The Bruggeman-Landauer approximation is based on the calculation of fields in a solitary inclusion; it is surprising that this approximation describes the limiting behaviour of the effective kinetic coefficients quite well. In particular, at $p = p_c$ the concentration dependence of the effective conductivity $\sigma_e(p)$ has a kink. The sharper, the greater the heterogeneity. Thus, the Bruggeman-Landauer approximation describes well the concentration behaviour $\sigma_e(p)$ and can be used to describe experimental data.

There is a drawback of this approximation, the sharp transition of the effective conductivity $\sigma_e(p)$ (at $\sigma_1/\sigma_2 \to \infty$), at the same time, the percolation threshold is always equal to $p_c = 1/3$. However, in real media [7], the percolation threshold may take on different values depending on the

method of creating the composite. Despite the logic of the derivation and the simplicity of the resulting expression, the Bruggeman-Landauer approximation needs modification.

In [7], a modification was considered that allows one to set the value of percolation threshold for the case $\sigma_1 > \sigma_2$. This modification was used in the model of magnetoelastic composites with the introduction of the method of moving percolation threshold [8 – 10].

$$\frac{\frac{\sigma_e-\sigma_1}{2\sigma_e+\sigma_1}}{1+c(p,\tilde{p}_c)\frac{\sigma_e-\sigma_1}{2\sigma_e+\sigma_1}}p+\frac{\frac{\sigma_e-\sigma_2}{2\sigma_e+\sigma_2}}{1+c(p,\tilde{p}_c)\frac{\sigma_e-\sigma_2}{2\sigma_e+\sigma_2}}(1-p)=0, \tag{6}$$

where $c(p,\tilde{p}_c)$ is the Sarychev-Vinogradov term

$$c(p,\tilde{p}_c)=(1-3\tilde{p}_c)\left(\frac{p}{\tilde{p}_c}\right)^{\tilde{p}_c}\left(\frac{1-p}{1-\tilde{p}_c}\right)^{1-\tilde{p}_c} \tag{7}$$

A more complicated situation is observed in the mean-field approximation in the descriptions of the effective elastic properties of composites [10]. The mean-field approximation for elasticity is the Budiansky approximation [13, 14], with a large heterogeneity of elastic properties for the three-dimensional case, it gives the percolation threshold 1/2, and for the two-dimensional case – 2 /3, which contradicts the geometric considerations of the percolation structure.

Fig.2 shows the concentration dependence of the effective conductivity with regard to the Sarychev-Vinogradov term (6, 7). As can be seen from Fig.3, for a large heterogeneity ($\sigma_1 \gg \sigma_2$), the percolation threshold coincides, as it should be, with the one specified in the term $\tilde{p}_c$.

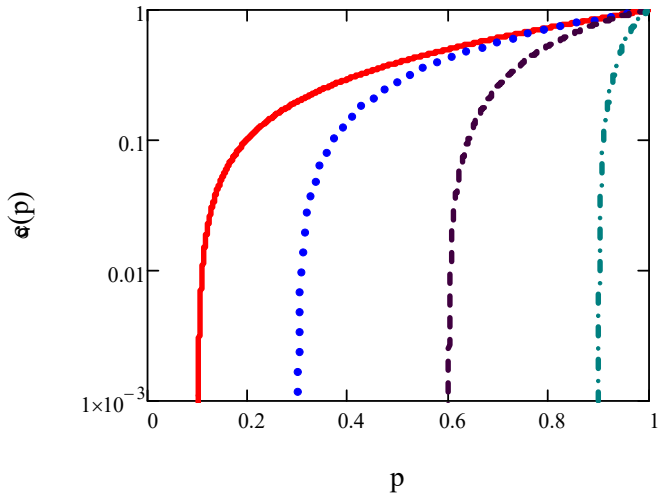

Fig. 2 Concentration behaviour of the effective conductivity according to (6, 7)

The situation is more complicated with a given value of the ratio σ_1/σ_2. The resulting threshold deviates from the one set in Svt $\tilde{p}_c$. To determine the type and magnitude of the deviation of p_c from $\tilde{p}_c$, we write down the solution of Eq.(6) in an explicit form.

$$\sigma_e(\sigma_1,\sigma_2,p,\tilde{p}_c)=\frac{1}{4}\left[2\frac{3p-1+c}{2+c}\sigma_1+2\frac{2-3p}{2+c}\sigma_2+\right.$$
$$\left.+\sqrt{4\left(\frac{3p-1+c}{2+c}\sigma_1+\frac{2-3p}{2+c}\sigma_2\right)^2+16\frac{1-c}{2+c}\sigma_1\sigma_2}\ \right] \tag{8}$$

(for ease of notation $c(p,\tilde{p}_c)$ is written as c), and from the equation that determines the inflection point,

$$\frac{d^3}{dp^3}\sigma_e(\sigma_1,\sigma_2,p,\tilde{p}_c)=0 \tag{9}$$

we find the "percolation" threshold (in which the value of p is fulfilled (9)) for a given ratio σ_1/σ_2 – Fig. 3. As can be seen, the deviation values are not very large.

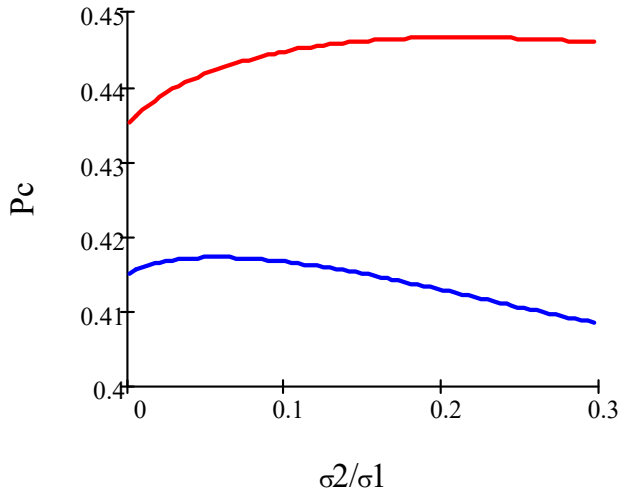

Fig.3 Percolation threshold at a given phase conductivity ratio

Term modification

A s is obvious from the direct solution of the self-consistency equation (the Bruggeman-Landauer approximation) the term works only at $\sigma_1>\sigma_2$. Thus, for instance, see Fig. 4, on setting $\tilde{p}_c=0.2$ at $\sigma_1>\sigma_2$ the obtained percolation threshold is really equal to 0.2, however, at $\sigma_1<\sigma_2$ (in both cases we have strongly inhomogeneous composite) the threshold is not 0.2, but 0.737.

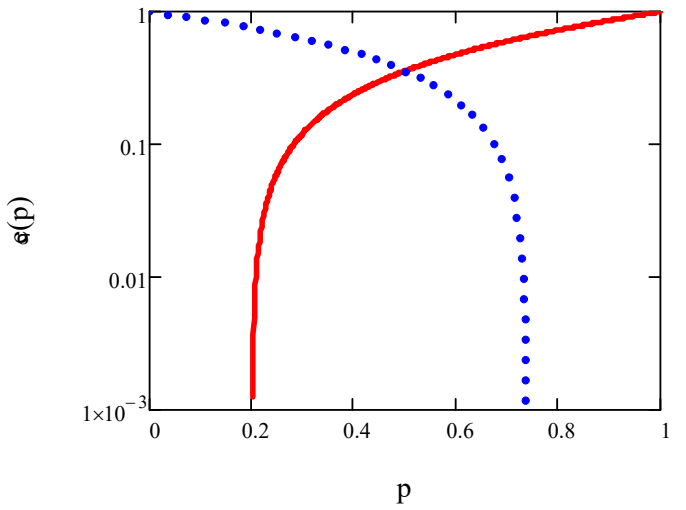

a)

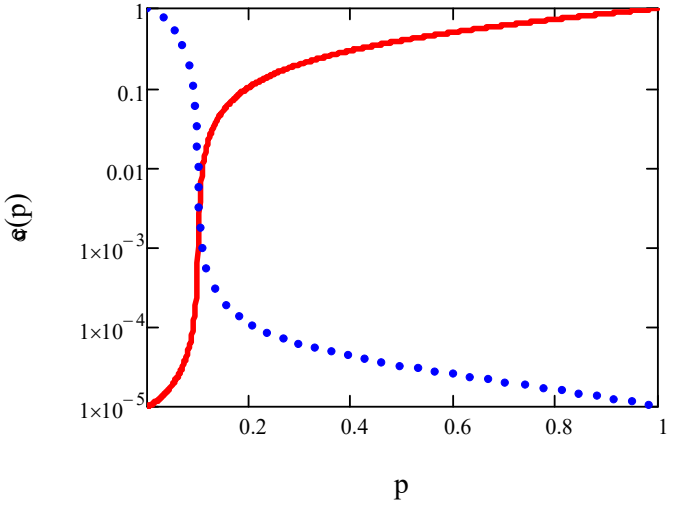

b)

Fig.4 Percolation thresholds
4a – incorrect case, 4б – correct case

It is necessary to modify the term so that it gives correct values of percolation threshold both at $\sigma_1 > \sigma_2$ and at $\sigma_1 < \sigma_2$.

Based on the symmetry of the behaviour of $\sigma_e(\sigma_1, \sigma_2, p)$ depending on the concentration and phase conductivity values

$$\sigma_e(\sigma_1, \sigma_2, p) = \sigma_e(\sigma_2, \sigma_1, 1-p), \tag{10}$$

and term (7), one can define the type of term for the case $\sigma_1 < \sigma_2$

$$c(p, \tilde{p}_c) = (3p-2)\left(\frac{p}{\tilde{p}_c}\right)^{\tilde{p}_c}\left(\frac{1-p}{1-\tilde{p}_c}\right)^{1-\tilde{p}_c}. \tag{11}$$

Combining these terms into one, so that at $\sigma_1 > \sigma_2$ term (7) would occur, and at $\sigma_1 < \sigma_2$ term (11) would have the form

$$c\left(p,\tilde{p}_c\right) = -\frac{1}{2} + \frac{3}{2}\left(1-2\tilde{p}_c\right)U\left(\sigma_1,\sigma_2\right), \tag{12}$$

where $U\left(\sigma_1,\sigma_2\right)$ function is related to sign function $\mathrm{sgn}\left(x\right)$ and has the form

$$U\left(\sigma_1,\sigma_2\right) = \begin{cases} 1, \sigma_1 > \sigma_2 \\ 0, \sigma_1 = \sigma_2 \\ -1, \sigma_1 < \sigma_2 \end{cases}. \tag{13}$$

The function $U\left(\sigma_1,\sigma_2\right)$ can be selected in the following way

$$U\left(\sigma_1,\sigma_2\right) = \frac{\sigma_1 - \sigma_2}{\left|\sigma_1 - \sigma_2\right|}. \tag{14}$$

If there is a need to differentiate the expression from з $U\left(\sigma_1,\sigma_2\right)$, it can be approximated by a smooth function $\bar{U}\left(\sigma_1,\sigma_2\right)$ that has derivatives at any point

$$\bar{U}\left(\sigma_1,\sigma_2\right) = \frac{e^{-\beta\left(\frac{\sigma_2}{\sigma_1}-1\right)}-1}{e^{-\beta\left(\frac{\sigma_2}{\sigma_1}-1\right)}+1}, \tag{15}$$

where the larger the parameter β, the closer the function $\bar{U}\left(\sigma_1,\sigma_2\right)$ to a step function.

Fig.4 b shows the dependence of the effective conductivity on the concentration at a given percolation threshold $\tilde{p}_c = 0.1$ at $\sigma_1 = 1, \sigma_2 = 10^{-5}$ (conditional units) and the opposite case, when $\sigma_1 = 10^{-5}, \sigma_2 = 1$

Now, having a term in the form (12,13) or (12,15), it is possible to find various dependences of the effective coefficients for any inequality σ_1, σ_2 in a uniform way.

Effective thermoelectric properties of randomly heterogeneous media

In [11], the thermoelectric properties of composites with different percolation thresholds were considered. A mean-field approximation with a term similar to Svt was used [7]. Here, we use a modified term (12-15), which allows us to consider any cases of inequalities in the local kinetic coefficients of phases in a uniform way.

We choose the following values of the kinetic coefficients of the first and second phases [15], at a temperature T = 300 K:

$$\sigma_1 = 5\cdot 10^6\,\text{Ом}^{-1}\text{м}^{-1},\ \kappa_1 = 36.1\ \text{Вт}/(\text{м}\cdot\text{К}),\ \alpha_1 = 0\ \text{В}/\text{К},$$

$$\sigma_2 = 10^5\,\text{Ом}^{-1}\text{м}^{-1},\ \kappa_2 = 0.963\ \text{Вт}/(\text{м}\cdot\text{К}),\ \alpha_2 = 173\cdot 10^{-6}\,\text{В}/\text{К}, \qquad (16)$$

where κ is thermal conductivity, α is thermoEMF. Thus, in the selected variant $\sigma_1 > \sigma_2$ and $\kappa_1 > \kappa_2$ the thermoelectric figure of merit of phases is equal to

$$Z_1 T = 0, \qquad Z_2 T = \frac{\sigma_2 \alpha_2^2}{\kappa_2} T = 1.2 \qquad (17)$$

We introduce parameter λ, which allows us to consider a set of values σ_2 and α_2. The figure of merit $Z_2 T$ remains unchanged, but inequality $\sigma_1 > \sigma_2$ is reversed

$$\sigma_2(\lambda) = \sigma_2(1+\lambda), \qquad \alpha_2(\lambda) = \alpha_2(1+\lambda)^{-1/2},\ \lambda \in [0, 9] \qquad (18)$$

At $\lambda = 0$ there is an initial set of values of local kinetic coefficients, and at $\lambda = 9$, $\sigma_2 = 10^6\ Ohm^{-1}m^{-1}$ and $\alpha_2 = 63\cdot 10^{-6}\ V/K$. Now the reverse inequality $\sigma_2 > \sigma_1$ holds for conductivity.

We write the expression for current densities and heat flux in the form

$$\langle \mathbf{j} \rangle = \sigma_e \langle \mathbf{E} \rangle + \sigma_e \alpha_e \langle -\nabla \mathrm{T} \rangle,$$

$$\frac{\langle \mathbf{q} \rangle}{T} = \sigma_e \alpha_e \langle \mathbf{E} \rangle + \kappa_e \frac{1 + Z_e T}{T} \langle -\nabla T \rangle, \qquad (19)$$

where ∇T is temperature gradient.

We introduce the matrix of local and effective kinetic coefficients $\mathbf{\Omega}$

$$\hat{\Omega}_i = \begin{pmatrix} \sigma_i & \sigma_i \alpha_i \\ \sigma_i \alpha_i & \kappa_i \dfrac{1 + Z_i T}{T} \end{pmatrix}, \qquad (20)$$

where i is phase number.

In such notation, the mean-field approximation for thermoelectric phenomena can be written as (details are given in [11])

$$\mathbf{\Lambda}_1 p + \mathbf{\Lambda}_2 (1 - p) = 0, \qquad (21)$$

where

$$\mathbf{\Lambda}_1 = \frac{\hat{\Omega}_e - \hat{\Omega}_1}{2\hat{\Omega}_e + \hat{\Omega}_1}, \qquad \mathbf{\Lambda}_2 = \frac{\hat{\Omega}_e - \hat{\Omega}_2}{2\hat{\Omega}_e + \hat{\Omega}_2}, \qquad (22)$$

where expressions of the type $\dfrac{\hat{\Omega}_e - \hat{\Omega}_1}{2\hat{\Omega}_e + \hat{\Omega}_1}$ are understood as $\left(\hat{\Omega}_e - \hat{\Omega}_1\right)\left(2\hat{\Omega}_e + \hat{\Omega}_1\right)^{-1}$.

The self-consistency equation with a modified term is given by

$$\frac{\Lambda_1}{1+\mathbf{C}\Lambda_1} p + \frac{\Lambda_2}{1+\mathbf{C}\Lambda_2}(1-p) = 0, \tag{23}$$

where now the term is written in the form of a matrix

$$\mathbf{C}(p, \tilde{p}_c) = \begin{pmatrix} c_\sigma(p, \tilde{p}_c) & 0 \\ 0 & c_\kappa(p, \tilde{p}_c) \end{pmatrix}$$

Here, $c_\sigma(p, \tilde{p}_c)$ is taken from (12-15), and $c_\kappa(p, \tilde{p}_c)$ is found therefrom with a corresponding replacement of σ_1 by κ_1 and σ_2 by κ_2.

Let us analyse the resulting solution (23) for the figure of merit. Fig.5 shows the dependence of Z_eT on parameter λ. With a change in parameter λ, the phase figures of merit remain unchanged. Surprisingly enough, the effective figure of merit in this case is a function of parameter λ. Note also the nonlinear dependence of the effective figure of merit on parameter λ.

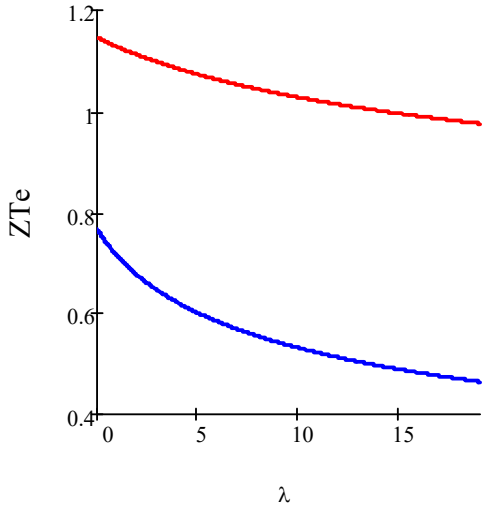

Fig.5 Dependence of Z_eT on parameter λ.
The upper curve at a concentration of 0.1, the other – at 0.3

Fig.6 shows the dependence of the effective figure of merit Z_eT on the concentration of the first phase p for different values of parameter λ. Note that these dependences change the ranking by the values of parameter λ (the larger the parameter, the larger the maximum) when passing through the percolation threshold.

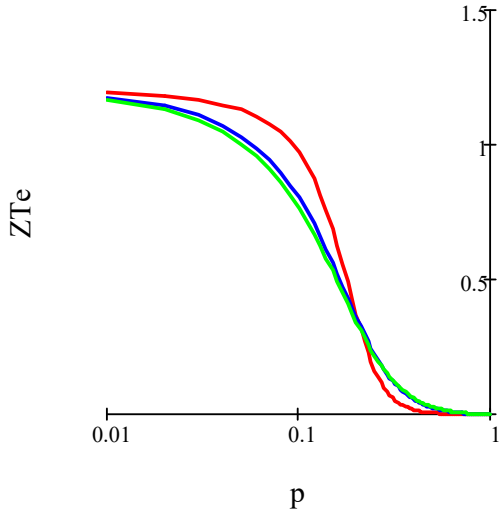

Fig.6 Dependence of the effective figure of merit Z_eT on the concentration of the first phase for different values of parameter λ (from top to bottom in the left part) the parameter is equal to 0, 9, 15

Conclusion

Using the modification of the term proposed in [11], the behaviour of the effective figure of merit Z_eT with a different set of local kinetic coefficients was considered. As it turned out, with constant values of local figures of merit $Z_1T = \text{const}$, $Z_2T = \text{const}$ the value Z_eT changes with a change in the set of kinetic coefficients. It is interesting to consider a similar modification of the term for the task of determining effective elastic moduli.

This approach makes it possible to describe composites with different percolation thresholds within the framework of the mean-field theory. Note that the values of the effective coefficients, even far from the percolation threshold, depend on the value of the percolation threshold. Composites with nanoparticles exhibit [16] unusual percolation threshold values from the point of view of standard mean-field theory and percolation theory (there is, among other things, a difference between the experimentally obtained percolation threshold values for, for example, electrical conductivity and elasticity). The approach proposed in this paper makes it possible (formally, without elucidating the physical reason for such a phenomenon) to describe the effective properties of such composites.

References

1. Torquato S. (2002). *Random heterogeneous materials. Microstructure and macroscopic properties.* Springer Verlag: New York, USA, doi: 10.1115/1.1483342
2. Balagurov B. Ya. (2015). Electrophysical properties of composites. Moscow: Lenand.
3. Choy T. C. (2016). *Effective medium theory: principles and applications*, Oxford University Press: Oxford, UK, doi: 10.1093/acprof:oso/9780198705093.001.0001

4. Snarskii A., Bezsudnov IV, Sevryukov VA, Morozovskiy A., Malinsky J. (2016). *Transport processes in macroscopically disordered media. From mean field theory to percolation.* Springer Verlag: New York, USA, doi: 10.1007/978-1-4419-8291-9.
5. Bruggeman V. D. (1935). Berechnung verschiedener physikalischer Konstanten von heterogenen Substanzen. I. Dielektrizitätskonstanten und Leitfähigkeiten der Mischkörper aus isotropen Substanzen. *Ann. Phys . (Leipzig)*, *16*, 664. doi: 10.1002/andp.19354160705
6. Landauer R. (1952). The electrical resistance of binary metallic mixtures. *J. Appl. Phys. 23*, 784. doi:10.1063/1.1702301.
7. Sarychev A. K., Vinogradov A. P. (1863). Effective medium theory for the magnetoconductivity tensor of disordered material. *phys. stat. sol. (b)*, *117* , K113-K118. doi: 10.1002/pssb.2221170252
8. Snarskii A., Zorinets D., Shamonin M., Kalita V. (2019). Theoretical method for calculation of effective properties of composite materials with reconfigurable microstructure: electric and magnetic phenomena. *Phys. A: Stat. Mech. Appl. 535* , 122467. doi: 10.1016/j.physa.2019.122467
9. Snarskii A., Shamonin M., Yuskevich P. (2020). Colossal magnetoelastic effects in magnetoactive elastomers. arxiv: 2002.11762, 2020.
10. Snarskii A., Shamonin M., Yuskevich P. (2020). Effective medium theory for elastic properties of composite materials with various percolation thresholds. *Materials*, 13, 1243.
11. Snarskii A., Yuskevich P. (2019). Effective medium theory for the thermoelectric properties of composite materials with various percolation thresholds. *J.Thermoelectricity*, 3, 40.
12. Lee S., Hippalgaonkar K., Yang F., Hong J., Ko C., Suh J., Liu K., Wang K., Urban JJ, Zhang X., Dames C., Hartnoll SA, Delaire O., Wu J. (2017). *Science*, 355, 371.
13. Budiansky, B. (1965). On the elastic moduli of some heterogeneous materials. *J. Mech. Phys. Solids*, 13, 223-227. doi: 10.1016/0022-5096(65)90011-6
14. Shermergor T. D. (1977). *Theory of elasticity of microinhomogeneous media.* Moscow: Nauka.
15. Rowe D. M (2006). Thermoelectrics Handbook (macro to nano), Taylor Francis, 1000.
16. M.-L. Huang, Y.-D. Shi, M. Wang. (2022). A comparative study on nanoparticle network-dependent electrical conductivity, electromagnetic wave shielding effectiveness and rheological properties in multiwall carbon nanotubes filled polymer nanocomposites, *Polym. Compos.* 1. https://doi.org/10.1002/pc.2716

Submitted 16.03.2022

Снарський А., *док. фіз.- мат. наук, професор*
Федотов В., *ст.викладач*

Національний технічний університет України
"Київський політехнічний інститут
імені Ігоря Сікорського", проспект Перемоги, 37,
Київ, 03056, Україна, *e - mail:asnarskii@gmail.com*

ТЕРМОЕЛЕКТРИЧНІ КОМПОЗИТИ З РІЗНИМИ ПОРОГАМИ ПРОТІКАННЯ

Розглядається модифікація наближення середнього поля для опису поведінки ефективних кінетичних коефіцієнтів, у тому числі для термоелектричних композитів. Запропонована модифікація дозволяє описувати випадково-неоднорідні середовища з різними порогами протікання при довільних значеннях локальних кінетичних коефіцієнтів. Бібл. 16. рис. 6.
Ключові слова: термоелектричні композити, кінетичні коефіцієнти.

References

1. Torquato S. (2002). *Random heterogeneous materials. Microstructure and macroscopic properties.* Springer Verlag: New York, USA, doi: 10.1115/1.1483342
2. Balagurov B. Ya. (2015). Electrophysical properties of composites. Moscow: Lenand.
3. Choy T. C. (2016). *Effective medium theory: principles and applications*, Oxford University Press: Oxford, UK, doi: 10.1093/acprof:oso/9780198705093.001.0001
4. Snarskii A., Bezsudnov IV, Sevryukov VA, Morozovskiy A., Malinsky J. (2016). *Transport processes in macroscopically disordered media. From mean field theory to percolation.* Springer Verlag: New York, USA, doi: 10.1007/978-1-4419-8291-9.
5. Bruggeman V. D. (1935). Berechnung verschiedener physikalischer Konstanten von heterogenen Substanzen. I. Dielektrizitätskonstanten und Leitfähigkeiten der Mischkörper aus isotropen Substanzen. *Ann. Phys . (Leipzig)*, *16*, 664. doi: 10.1002/andp.19354160705
6. Landauer R. (1952). The electrical resistance of binary metallic mixtures. *J. Appl. Phys. 23*, 784. doi:10.1063/1.1702301.
7. Sarychev A. K., Vinogradov A. P. (1863). Effective medium theory for the magnetoconductivity tensor of disordered material. *phys. stat. sol. (b)*, *117* , K113-K118. doi: 10.1002/pssb.2221170252
8. Snarskii A., Zorinets D., Shamonin M., Kalita V. (2019). Theoretical method for calculation of effective properties of composite materials with reconfigurable microstructure: electric and magnetic phenomena. *Phys. A: Stat. Mech. Appl. 535* , 122467. doi: 10.1016/j.physa.2019.122467
9. Snarskii A., Shamonin M., Yuskevich P. (2020). Colossal magnetoelastic effects in magnetoactive elastomers. arxiv: 2002.11762, 2020.
10. Snarskii A., Shamonin M., Yuskevich P. (2020). Effective medium theory for elastic properties of composite materials with various percolation thresholds. *Materials*, 13, 1243.
11. Snarskii A., Yuskevich P. (2019). Effective medium theory for the thermoelectric properties of composite materials with various percolation thresholds. *J.Thermoelectricity*, 3, 40.
12. Lee S., Hippalgaonkar K., Yang F., Hong J., Ko C., Suh J., Liu K., Wang K., Urban JJ, Zhang X., Dames C., Hartnoll SA, Delaire O., Wu J. (2017). *Science*, 355, 371.
13. Budiansky, B. (1965). On the elastic moduli of some heterogeneous materials. *J. Mech. Phys. Solids*, 13, 223-227. doi: 10.1016/0022-5096(65)90011-6
14. Shermergor T. D. (1977). *Theory of elasticity of microinhomogeneous media.* Moscow: Nauka.

15. Rowe D. M (2006). Thermoelectrics Handbook (macro to nano), Taylor Francis, 1000.
16. M.-L. Huang, Y.-D. Shi, M. Wang. (2022). A comparative study on nanoparticle network-dependent electrical conductivity, electromagnetic wave shielding effectiveness and rheological properties in multiwall carbon nanotubes filled polymer nanocomposites, *Polym. Compos.* 1. https://doi.org/10.1002/pc.2716

Submitted 16.03.2022

DOI: 10.63527/1607-8829-2022-1-18-27

P. V. Gorskiy

P. V. Gorskyi, *dok. phys.– mat. sciences*[1,2]
R. V. Kuz , *cand. phys.– mat. sciences*[1,2]

Institute of Thermoelectricity of the NAS
and MES of Ukraine,
1, Nauky str., Chernivtsi, 58029, Ukraine,
[2]Yuriy Fedkovych Chernivtsi National University
2 Kotsiubynskyi str., Chernivtsi, 58012, Ukraine

R. V. Kuz

ANALYTICAL CALCULATION OF THE EFFECT OF METAL COATING OF THERMOELECTRIC LEGS ON THE EFFICIENCY OF GENERATOR THERMOELEMENT

The effect of the protective metal coating of the lateral surface of thermoelectric legs on the efficiency of a generator thermoelement has been determined. At the same time, it is taken into account that the metal coating shunts the thermoelectric leg both in terms of electric current and heat flux. Theoretical calculations were made without taking into account eddy thermoelectric currents in the "thermoelectric material - protective coating" system and the temperature dependences of the characteristics of the metal and thermoelectric material for the "bismuth telluride - nickel" couple. The effects of the metal coating on the effective thermoEMF of the leg are taken into account. It is shown that when the influence of the metal coating on the thermoEMF of the leg is taken into account, the efficiency is a sharply monotonically decreasing function of the thickness of the metal coating, so that in order to achieve the efficiency of a thermoelement at a level of about 5%, the coating thickness should be no more than 0.5 μm at a leg height of 1 mm, about 0.9 μm for the leg height of 2 mm and about 1 μm with a leg height of 3 mm. In so doing, it is assumed that the electrical contact resistance is about 10^{-5} Ohm•cm^2, and the thermal contact resistance is absent. However, in the presence of thermal contact resistance at a level of 0.8 K•cm^2 /W, the efficiency of the thermoelement remains at a level of about 5.3% even with a coating thickness of 5 μm. Bibl. 11, Fig. 5.

Key words: thermoelement reliability, thermoelectric leg, metal coating, shunt, thermoelectric figure of merit, effective thermoEMF, coating thickness, maximum thermoelement efficiency.

Introduction

Reliability, in particular the resource stability of thermoelectric generator modules, is their even more important parameter than consumer characteristics. This is due to the fact that they are used, in particular, in systems where their replacement in the event of a failure is impossible or difficult, for example, in the space industry and medicine. And the resource is essentially determined by the stability of thermoelements that make up these modules, and, consequently, by the stability of

thermoelectric materials of which their thermoelectric legs are made. Among the typical failure mechanisms of thermoelements and thermoelectric generator modules, sublimation of volatile components and alloying impurities from thermoelectric materials and mechanical destruction of thermoelectric legs both in the process of manufacturing thermoelectric generator modules and during their operation are singled out. To prevent or reduce the negative impact of these factors on the consumer characteristics of thermoelectric generator modules, the lateral surface of thermoelectric legs is partially or completely covered with various coatings, in so doing, completely - as a rule, polymer [1], glass-enamel [2] or ceramic [3], and partially - metal [4]. To increase the mechanical stability of thermoelectric generator modules, the mechanical stability, coefficient of linear thermal expansion, Young's modulus, Poisson's ratio, and thermal conductivity of the thermoelectric material are specially coordinated with each other during their design [5 – 7], and special frames are used between the thermoelectric legs to limit their displacement and deformations during the operation of generator modules [8]. In all these cases, reduction of heat flux shunting of thermoelectric legs is achieved [9]. However, for the simultaneous solution of these problems, it seems promising to cover the lateral surface of thermoelectric legs with metal. Since such a coating significantly shunts the thermoelectric leg in terms of electric current and heat flux, the purpose of this article is an approximate assessment of the influence of the geometric characteristics of such a coating on the efficiency of a thermocouple thermoelement in the electric power generation mode.

Physical model of a thermoelement with fully protected legs

A physical model of thermocouple thermoelement with fully protected legs is schematically shown in Fig.1.

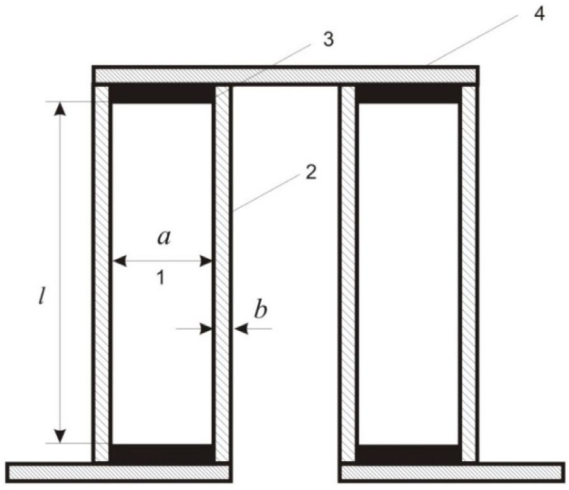

Fig. 1. Physical model of a thermoelement with protected legs:
1 – thermoelectric material;
2 – protective coating; 3 – anti-diffusion layer;
4 – soldered copper interconnect

In the model, it is assumed that the leg has the shape of a rectangular parallelepiped with a square cross-section. The metal coating is continuous. In addition, the following assumptions are made in the model at the initial stage of the study: 1) temperature dependences of the thermoelectric parameters of the semiconductor and metal are neglected, i.e. they are considered approximately constant in the temperature range in which the thermoelement operates; 2) there are no eddy currents at the interface between the thermoelectric material and the metal; 3) the end faces of the covering layer are in contact with the metal interconnect electrodes. In this case, the thermoelectric leg is equivalent to two electrical and thermal resistances connected in parallel, if the protective coating completely covers its side surface. In a thermocouple thermoelement, such legs should be considered electrically connected in series and thermally connected in parallel. We also take into account the electrical and thermal contact resistances, which we consider independent of temperature. The intrinsic resistance of metal connections, solder and anti-diffusion coating are neglected.

Calculation of thermoelement efficiency and discussion of its results

To calculate the efficiency of such a thermoelement, first determine the electrical and thermal resistance of each leg. They are equal, respectively:

$$R_E = \frac{\rho_s \rho_m l + 2\rho_{ce}\left[4\rho_s\left(\delta+\delta^2\right)+\rho_m\right]}{a^2\left[4\rho_s\left(\delta+\delta^2\right)+\rho_m\right]}, \tag{1}$$

$$R_T = \frac{\kappa_s^{-1}\kappa_m^{-1} l + 2\rho_{ct}\left[4\kappa_s^{-1}\left(\delta+\delta^2\right)+\kappa_m^{-1}\right]}{a^2\left[4\kappa_s^{-1}\left(\delta+\delta^2\right)+\kappa_m^{-1}\right]}. \tag{2}$$

In these formulae, a is the cross-sectional side of the leg, l is its length, $\delta = b/a$ is the relative thickness of the coating, i.e. the ratio of coating thickness to the side of the square cross-section of the leg, ρ_s, ρ_m are electric resistivities, respectively, κ_s, κ_m are thermal conductivities of semiconductor and metal, respectively, ρ_{ce}, ρ_{ct} are electrical and thermal contact resistivities, respectively.

We move on to determining the efficiency of a thermoelement with partially or fully protected legs. Let the materials of the legs have the same electrical resistivity and thermal conductivity and the Seebeck coefficients α_s of the same magnitude, but opposite in sign. Then the figure of merit of the thermoelectric leg will be equal to:

$$Z = \frac{\alpha_s^2 R_T}{R_E}. \tag{3}$$

With regard to relations (1) and (2), we will find the following expression for it:

$$Z = \alpha_s^2 \frac{\left\{\kappa_s^{-1}\kappa_m^{-1} l + 2\rho_{ct}\left[4\kappa_s^{-1}\left(\delta+\delta^2\right)+\kappa_m^{-1}\right]\right\}\left[4\rho_s\left(\delta+\delta^2\right)+\rho_m\right]}{\left[4\kappa_s^{-1}\left(\delta+\delta^2\right)+\kappa_m^{-1}\right]\left\{\rho_s\rho_m l + 2\rho_{ce}\left[4\rho_s\left(\delta+\delta^2\right)+\rho_m\right]\right\}}. \quad (4)$$

Assuming in this formula $\delta = 0$, $\rho_{ct} = 0$, $\rho_{ce} = 0$, we will come to the well-known expression for the figure of merit of thermoelectric material:

$$Z_{TEM} = \alpha_s^2 / \rho_s \kappa_s . \quad (5)$$

Note that formula (4) is also valid for a leg with a circular cross-section, if we understand δ as the ratio of the coating thickness to the diameter of the circular cross-section of the leg.

But, as a matter of fact, one should additionally take into account the effect of the coating on the thermoEMF of the leg, given that a leg with a metal coating, strictly speaking, should be considered not as one with a resistance connected in parallel, but as two sources of electrical energy connected in parallel. The equivalent electrical circuit of the coated leg is shown in Fig. 2.

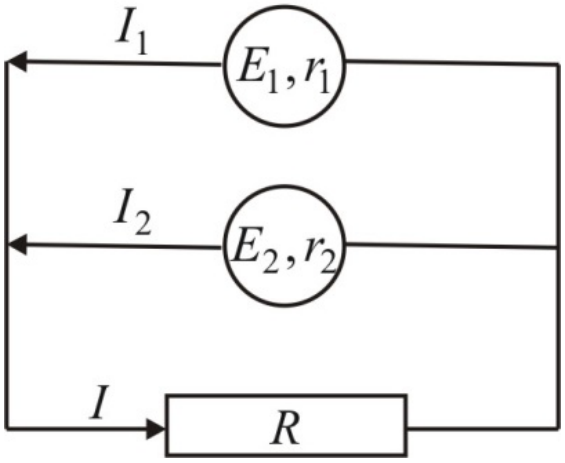

Fig. 2. Equivalent electrical circuit of coated thermoelectric leg

According to Kirchhoff's rules, we compose an equation for currents:

$$\begin{aligned} I_1 + I_2 - I &= 0 \\ I_1 r_1 + IR &= E_1 \\ I_2 r_2 + IR &= E_2 \end{aligned} \quad (6)$$

From this system we find current I:

$$I = \frac{E_1/r_1 + E_2/r_2}{\left(1/r_1 + 1/r_2\right)\left(R + \dfrac{r_1 r_2}{r_1 + r_2}\right)}. \quad (7)$$

From expression (10) it follows that two sources of electrical energy connected in parallel are equivalent to one source with an equivalent EMF equal to:

$$E = \frac{E_1/r_1 + E_2/r_2}{1/r_1 + 1/r_2}, \tag{8}$$

and equivalent internal resistance equal to:

$$r = \frac{r_1 r_2}{r_1 + r_2}. \tag{9}$$

It follows from formula (11) that for a *p*-type leg, the following should be substituted into it:

$$E_1 = \alpha_s \Delta T, \tag{10}$$

$$E_2 = \alpha_m \Delta T, \tag{11}$$

and for an *n*- type leg one should substitute:

$$E_1 = \alpha_s \Delta T, \tag{12}$$

$$E_2 = -\alpha_m \Delta T, \tag{13}$$

where α_m is thermoEMF of metal.

and, moreover, for legs of both types one should substitute:

$$r_1 = \rho_s \frac{l}{a^2}, \tag{14}$$

$$r_2 = \frac{\rho_m l}{4a^2\left(\delta + \delta^2\right)}. \tag{15}$$

Therefore, the expression for the effective figure of merit of the thermoelectric leg will take the following final form:

$$Z_e = \left[\frac{\alpha_s \rho_s^{-1}}{\rho_s^{-1} + \rho_m^{-1}\left(\delta + \delta^2\right)}\right]^2 \times \\ \times \frac{\left\{\kappa_s^{-1}\kappa_m^{-1} l + 2\rho_{ct}\left[4\kappa_s^{-1}\left(\delta + \delta^2\right) + \kappa_m^{-1}\right]\right\}\left[4\rho_s\left(\delta + \delta^2\right) + \rho_m\right]}{\left[4\kappa_s^{-1}\left(\delta + \delta^2\right) + \kappa_m^{-1}\right]\left\{\rho_s \rho_m l + 2\rho_{ce}\left[4\rho_s\left(\delta + \delta^2\right) + \rho_m\right]\right\}}. \tag{16}$$

Now we proceed to the calculation of maximum efficiency of thermoelement in the mode of electric energy generation. The geometrical dimensions of leg without coating will be assumed to be equal to a=1.4 mm, l=1, 2 or 3 mm, the coating thickness b, and, therefore, parameter $\delta = b/a$ will be considered to be variable, and material parameters will be considered to be temperature independent and equal to the following values: $\alpha_s = 160$ μV/K, $\rho_s = 7.143 \cdot 10^{-6}$ Ohm·m, $\rho_m = 7.5 \cdot 10^{-8}$ Ohm·m, $\kappa_s = 1.7$ W/(m·K), $\kappa_m = 90$ W/(m·K), electrical contact resistivity $\rho_{ce} = 10^{-9}$ Ohm·m^2, and thermal contact resistance will be neglected. To calculate maximum efficiency η_{max}, the following formula will be used [10]:

$$\eta_{\max} = \frac{T_h - T_c}{T_h} \cdot \frac{\sqrt{1 + 0.5 Z_e (T_h + T_c)} - 1}{\sqrt{1 + 0.5 Z_e (T_h + T_c)} + T_c / T_h}, \quad (17)$$

where T_h and T_c are the temperatures of the hot and cold thermoelement sides, respectively, Z_e – the effective thermoelectric figure of merit of a coated leg. The results of calculating the efficiency between the extreme temperatures 300 and 500 K are given in Figs. 3, 4.

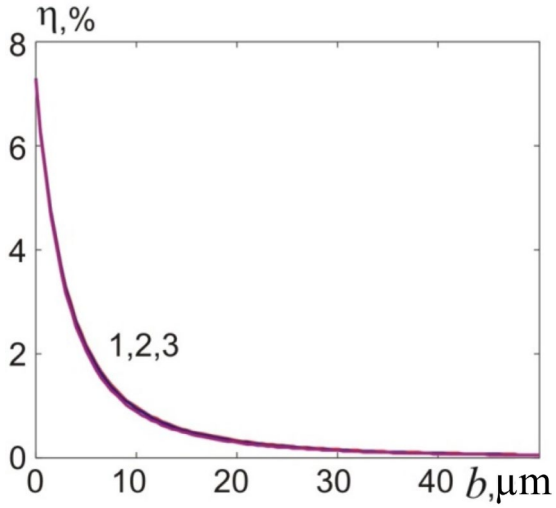

Fig. 3. Dependence of the efficiency on the thickness of the nickel coating of the leg based on Bi-Te in a wide range of thicknesses, with regard to the effect of the coating on the thermal EMF of the leg 1 - for a leg height of 3 mm; 2 – for a leg height of 2 mm; 3 – for a leg height of 1 mm

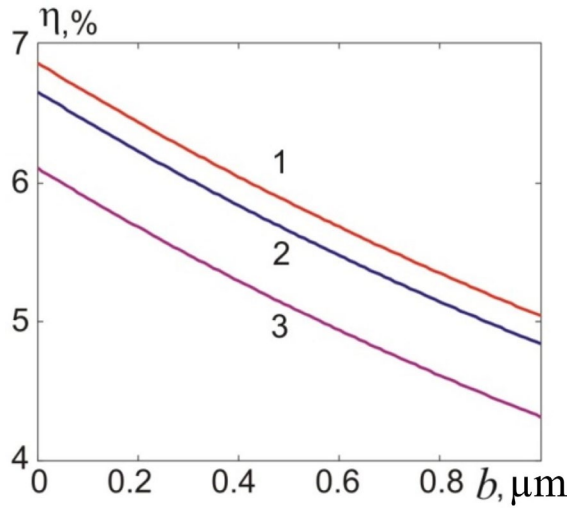

Fig. 4. Dependence of the efficiency on the thickness of the nickel coating of the leg based on Bi-Te in the range of thicknesses at which it is possible to maintain the efficiency of the thermoelement at a level of at least 4%: 1 – for a leg height of 3 mm; 2 – for a leg height of 2 mm; 3 – for a leg height of 1 mm

It can be seen from the figures that, taking into account the effect of the metal coating on the thermal EMF of the leg, the efficiency of the thermoelement is a sharply monotonically decreasing function of the coating thickness. If we disregard the effect of thermal contact resistance, then it turns out that in order to maintain the efficiency of a thermoelement at a level of at least 5 %, a coating with a thickness of no more than 0.9 μm should be produced at a leg height of 2 - 3 mm.

However, the presence of thermal contact resistance to a certain extent neutralizes the negative effect of heat flux shunting the legs. This is illustrated in Fig. 3. At the same time, based on the results of our thermal contact resistance calculations, we believe that the maximum value of the contact resistance can be about ρ_{ct}=0.8 K·cm^2/W.

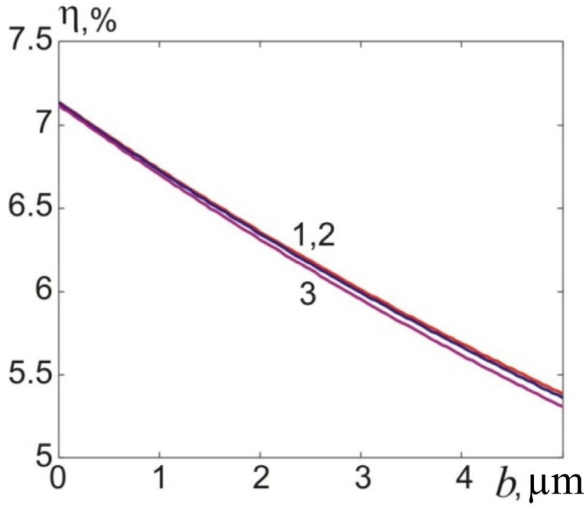

Fig. 5. Dependence of the efficiency on the thickness of nickel coating of the leg, with regard to thermal contact resistances in a wide range of thicknesses. The numbering of the curves is the same as in Fig. 4

We can see that the effect of thermal contact resistances slows down the drop in the efficiency of the thermocouple with the increase in the thickness of the nickel coating of the legs. Thus, if the assessment of thermal contact resistances is done correctly, it can be assumed that the efficiency of the thermocouple in the case of covering the lateral surface of the leg based on *Bi-Te* with a nickel and anti-sublimation layer 5 μm thick will remain at a level of 5.3-5.4 %.

Let us compare these results with those of [11] where, among other things, the influence of the presence of electrically conductive nickel layers on the isothermal faces of a zone-inhomogeneous thermoelement based on *Bi-Te* on its efficiency was studied. It is shown that the efficiency of such a thermoelement is a monotonically increasing function of the coating thickness, which quickly reaches saturation when the ratio of coating thickness to the linear size of the thermoelement coil is about 0.06. The efficiency value in this case reaches about 5.1 %, which, as follows from Fig. 3, is close to our results for a nickel anti-sublimation layer thickness of about 5 μm. However, a strict comparison of these results is not correct, because the equivalent electrical circuits of a thermocouple thermoelement with a protective conductive layer on each leg and a zone-inhomogeneous thermoelement, in which the conductive layer electrically connects the *n*-and *p*-regions, are fundamentally different from each other.

Conclusions

1. Without taking into account eddy currents in the "thermoelectric leg – anti-sublimation protective metal coating" system and the temperature dependences of thermoelectric parameters of thermoelectric material and metal, the thermoelectric figure of merit of a leg with a completely protected lateral surface is calculated.
2. It is shown that in the absence of thermal contact resistances, the maximum efficiency of a thermoelement with fully protected legs will remain at a level of about 5 % if, at a leg height of 2 - 3 mm, the coating thickness does not exceed 0.9 - 1 μm.
3. In the presence of thermal contact resistances of about 0.8 Kcm^2/W, the maximum efficiency of a thermoelement with fully protected legs will remain at a level of about 5.3 % if, at a leg height of 1 - 3 mm, the coating thickness does not exceed 5 μm.

References

1. WO/2015/126272. V. I. Grishin, D. V. Kotlov. Method of manufacturing semiconductor legs for thermoelectric module and thermoelectric module.
2. Sabo E. P. (2006). Mechanisms that determine the resource possibilities of thermoelectric converters. *J. Thermoelectricity*, 2, 59 - 70.
3. Salvo M., Smeacetto F., D'Isanto F. et al. (2018) Glass-ceramic oxidation protection of higher manganese silicide thermoelectrics Journal of European Ceramic Society. https://doi.org/10.1016/j.jeurceramsoc.2018.01.007
4. *US patent No US 7480984 B1* (2009). J. S. Sakamoto, T. Caillat, J.-P. Fleurial, G. J. Snyder. Method of suppressing sublimation in advanced thermoelectric devices.
5. Wereszczak A. A., McCarty R., Thompson, Sharp J. (2012). Thermoelectric mechanical reliability. *Vehicle technologies annual merit review and peer evaluation meeting*. Arlington VA. 15 May 2012.
6. Liu W., Jie Q., Kim H.S., Ren Z. *Current progress and future challenges in thermoelectric power generation: from materials to devices*. – Preprint of department of physics and Texas center for superconductivity (TcSUH) – University of Houston, Texas 77204, USA. – 60 p.
7. Karri N.K., Mo C. (2017). Reliable thermoelectric module design under opposing requirements from structural and thermoelectric considerations. *Journal of Electronic Materials*. November, 2017, 1-10. – https://doi:10.1007/s11664-017-5934-6 .
8. Yi Yan. (2019). Vertical self-defined thermoelectric legs for use in thin-film micro thermo electric generators (μ-TEG)/ Yi Yan . *A dissertation submitted in partial fulfillment of the requirements for the degree of Doctor of Philosophy (Electrical Engineering) in the University of Michigan*.
9. Song Lv., Liu M., Xe W. et al. (2020). Study of thermal insulation material influence on the performance of thermoelectric generators by creating a significant effective temperature difference. *Energy Conversion and Management*, Vol.207, 112516-1 – 112516-9.

10. Anatychuk L. I. (1979). *Termoelementy i termoelectricheskiie ustroistva. Spravochnik. [Thermoelements and thermoelectric devices. Guidebook]*. Kyiv: Naukova Dumka.
11. Anatychuk L. I., Kuz R. V., Luste O. J. (2005). Optimization of zone-inhomogeneous thermoelement with electrically conductive layers on isothermal faces. *J.Thermoelectricity*, 3, 68 - 73.

Submitted 13.03.2022

Горський П. В., *док. фіз.-мат. наук*[1,2]
Кузь Р. В., *канд.фіз.-мат. наук*[1,2]

[1]Інститут термоелектрики НАН та МОН України,
вул. Науки 1, Чернівці, 58029, Україна
[2]Чернівецький національний університет імені Юрія Федьковича,
ул. Коцюбинського 2, Чернівці, 58012, Україна;
Petro Gorskyi: *gena.grim@gmail.com*

АНАЛІТИЧНИЙ РОЗРАХУНОК ВПЛИВУ МЕТАЛЕВОГО ПОКРИТТЯ ТЕРМОЕЛЕКТРИЧНИХ ГІЛОК НА ККД ГЕНЕРАТОРНОГО ТЕРМОЕЛЕМЕНТА

Визначено вплив захисного металевого покриття бічної поверхні термоелектричних гілок на ККД генераторного термоелемента. При цьому враховано, що металеве покриття шунтує термоелектричну гілку як за електричним струмом, так і за тепловим потоком. Теоретичні розрахунки зроблено без врахування вихрових термоелектричних струмів у системі «термоелектричний матеріал – захисне покриття» і температурних залежностей характеристик металу і термоелектричного матеріалу для пари «телурид вісмуту – нікель». Враховано впливу металевого покриття на ефективну термоЕРС гілки. Показано, що при врахуванні впливу металевого покриття на термоЕРС гілки ККД є різко монотонно спадною функцією товщини металевого покриття, так що для досягнення ККД термоелемента на рівні близько 5% товщина покриття повинна складати не більше 0.5 мкм за висоти гілки 1 мм, близько 0.9 мкм за висоти гілки 2 мм і близько 1 мкм за висоти гілки 3 мм. При цьому вважається, що електричний контактний опір складає близько 10^{-5} Ом·см^2, а тепловий контактний опір відсутній. Однак за наявності теплового контактного опору на рівні 0.8 К·см^2/Вт ККД термоелемента зберігається на рівні близько 5.3% навіть за товщини покриття 5 мкм. Бібл. 11, рис. 5.

Ключові слова: *надійність термоелемента, термоелектрична гілка, металеве покриття, шунт, термоелектрична добротність, ефективна термоЕРС, товщина покриття, максимальний ККД термоелемента.*
елементи, телурид вісмуту.

References

1. WO/2015/126272. V. I. Grishin, D. V. Kotlov. Method of manufacturing semiconductor legs for thermoelectric module and thermoelectric module.
2. Sabo E. P. (2006). Mechanisms that determine the resource possibilities of thermoelectric converters. *J. Thermoelectricity*, 2, 59 - 70.
3. Salvo M., Smeacetto F., D'Isanto F. et al. (2018) Glass-ceramic oxidation protection of higher manganese silicide thermoelectrics Journal of European Ceramic Society. https://doi.org/10.1016/j.jeurceramsoc.2018.01.007
4. *US patent No US 7480984 B1* (2009). J. S. Sakamoto, T. Caillat, J.-P. Fleurial, G. J. Snyder. Method of suppressing sublimation in advanced thermoelectric devices.
5. Wereszczak A. A., McCarty R., Thompson, Sharp J. (2012). Thermoelectric mechanical reliability. *Vehicle technologies annual merit review and peer evaluation meeting*. Arlington VA. 15 May 2012.
6. Liu W., Jie Q., Kim H.S., Ren Z. *Current progress and future challenges in thermoelectric power generation: from materials to devices*. – Preprint of department of physics and Texas center for superconductivity (TcSUH) – University of Houston, Texas 77204, USA. – 60 p.
7. Karri N.K., Mo C. (2017). Reliable thermoelectric module design under opposing requirements from structural and thermoelectric considerations. *Journal of Electronic Materials*. November, 2017, 1-10. – https://doi:10.1007/s11664-017-5934-6 .
8. Yi Yan. (2019). Vertical self-defined thermoelectric legs for use in thin-film micro thermo electric generators (μ-TEG)/ Yi Yan . *A dissertation submitted in partial fulfillment of the requirements for the degree of Doctor of Philosophy (Electrical Engineering) in the University of Michigan*.
9. Song Lv., Liu M., Xe W. et al. (2020). Study of thermal insulation material influence on the performance of thermoelectric generators by creating a significant effective temperature difference. *Energy Conversion and Management*, Vol.207, 112516-1 – 112516-9.
10. Anatychuk L. I. (1979). *Termoelementy i termoelectricheskiie ustroistva. Spravochnik. [Thermoelements and thermoelectric devices. Guidebook]*. Kyiv: Naukova Dumka.
11. Anatychuk L. I., Kuz R. V., Luste O. J. (2005). Optimization of zone-inhomogeneous thermoelement with electrically conductive layers on isothermal faces. *J.Thermoelectricity*, 3, 68 - 73.

Submitted 13.03.2022

DOI: 10.63527/1607-8829-2022-1-28-43

V. A. Romaka, *doc. techn sciences, professor*[1]
Yu. V. Stadnyk, *cand. chem. of science*[2]
L. P. Romaka, *cand. chem. of science*[2]
Yu. O. Plevachuk *doc. phys. and math sciences* [2]
V. V. Romaka, *doc. techn sciences,*
cand. chem. of science, professor [3]
A. M. Horyn, *cand. chem. of science*[2]
V. Z. Pashkevych, *cand. tehn. of science*[1]
A. V. Zelinskiy *cand. tehn. of science*[2]

[1]National University "Lvivska Politechnika", 12, S. Bandera Str., Lviv, 79013, Ukraine,
e-mail: vromaka@polynet.lviv.ua;
[2]Ivan Franko National University of Lviv, 6, Kyryla and Mefodiya Str., Lviv, 79005, Ukraine,
e-mail: lyubov.romaka@lnu.edu.ua
[3]Leibniz Institute for Solid State and Materials Research, IFW-Dresden, Helmholtzstr. 20, 01069 Dresden, Germany

RESEARCH OF THE THERMOELECTRIC MATERIAL $Lu_{1-x}V_xNiSb$: MODELING OF PROPERTIES

The result of modeling the crystal and electronic structures, thermodynamic and kinetic properties of $Lu_{1-x}V_xNiSb$ is establishing the nature of the generated energy states. It is shown that the semiconductor solid solution $Lu_{1-x}V_xNiSb$ is a promising thermoelectric material, and at a temperature of T≈620 K and a concentration of $Lu_{0.99}V_{0.01}NiSb$, the thermoelectric factor Z values reach the maximum values of ZT = 0.62. It was established that the impurity atoms of V ($3d^34s^2$), introduced into the structure of the LuNiSb compound, simultaneously occupy the crystallographic positions 4a of Lu atoms ($5d^16s^2$) and 4c of Ni atoms ($3d^84s^2$) in different ratios, generating in the band gap ε_g impurity donor ε_D^V and acceptor ε_A^{Ni} energy states. The ratio of concentrations of donors and acceptors determines the location of the Fermi level ε_F and the mechanisms of electrical conductivity. Bibl. 28, Fig. 6.

Key words: electronic structure, figure of merit of thermoelectric material, resistivity, thermopower coefficient

Introduction

One of the most studied thermoelectric materials, which have a high efficiency of converting thermal energy into electrical energy, are semiconductor solid substitution solutions based on half-

Heusler phases, in particular, *MNiSn* (*M – Ti, Zr, Hf*) and *RNiSb* (*R – Y, Gd– Lu*) [1, 2], which crystallize in the *MgAgAs* structural type (space group $F\bar{4}3m$) [3]. Therefore, one of the subjects of the research presented below is the modeling of the thermodynamic, structural, energy and kinetic properties of the semiconductor thermoelectric material $Lu_{1-x}V_xNiSb$, obtained by doping the base semiconductor *p-LuNiSb* with *V* atoms ($3d^3 4s^2$), introduced into the structure by replacing *Lu* atoms in the 4*a* position ($5d^1 6s^2$). Modeling of the dynamics of the crystal and electronic structures, thermodynamic and kinetic properties of the $Lu_{1-x}V_xNiSb$ semiconductor will allow us to understand the mechanism of generation in the band gap ε_g of energy states that determine its properties. In practice, this is realized by choosing alloying conditions: the type and concentration of the impurity, the method of introduction, and modes of homogenizing annealing. This is the essence of optimizing the values of the specific electrical conductivity $\sigma(T)$, thermopower coefficient $\alpha(T)$ and thermal conductivity $\kappa(T)$ to the values that will meet the conditions for obtaining the maximum values of the thermoelectric factor Z ($Z = \alpha^2 \cdot \sigma/\kappa$) [2 , 4].

Semiconductor materials, unlike metals or metal alloys, are convenient for optimizing their characteristics and obtaining maximum values of thermoelectric factor. The fact is that in metals and metal alloys, the values of thermopower coefficient $\alpha(T)$ are small, and changes in the values of the coefficient of thermal conductivity $\kappa(T)$ and specific electrical conductivity $\sigma(T)$ due to the constancy of the Lorentz number cannot significantly change the value of the thermoelectric factor *Z*. That is why the optimization of the characteristics by the appropriate doping of semiconductors allows to achieve the conditions under which the values of the thermoelectric factor *Z* will be maximum [4].

In this context, it is extremely important to understand the structural features of the *p-LuNiSb* base semiconductor. Since the optimization of characteristics is carried out by doping *p-LuNiSb*, in order to achieve the maximum efficiency of the conversion of thermal energy into electrical energy, it is necessary to choose the type and concentration of the impurity when the Fermi level ε_F approaches the zone of continuous energies [2, 4]. And this cannot be done without comprehensive knowledge of the crystal and electronic structures of a semiconductor and their transformation during doping.

The study of the structural, kinetic, and magnetic properties of compounds of half-Heusler phases *RNiSb* (*R – Y, Gd–Lu*) [5, 6] established that their crystal structure is unordered. In addition, it was shown that *RNiSb* compounds are semiconductors and holes are the main current carriers at all investigated temperatures. A detailed analysis of the crystal and electronic structures of half-Heusler *RNiSb* phases allowed the authors of [7] to establish the nature of disorder in their structure. It was shown that there are vacancies (Vac) in crystallographic positions 4*a* of rare earth metal atoms and 4*c* of *Ni* atoms (Fig. 1). In turn, the vacancies in the *RNiSb* crystal structure are point defects of an acceptor nature, which generate the corresponding acceptor states ε_A^{Vac} in the band gap ε_g [7]. Therefore, the nature of the hole-type conductivity of half-Heusler *RNiSb* phases is understandable, as indicated by the results of kinetic and galvanomagnetic studies [5 – 7].

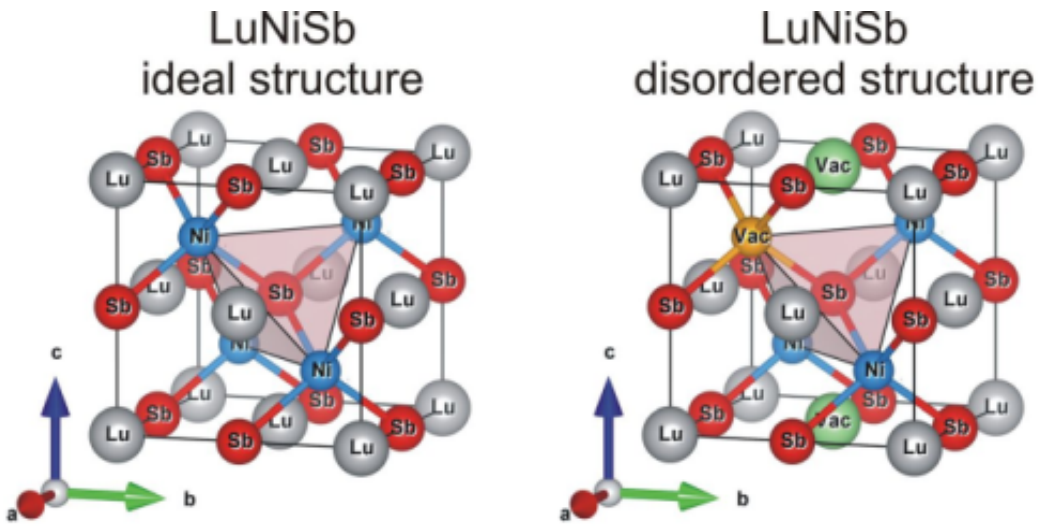

Fig. 1. Models of the crystal structure of the half-Heusler phase of LuNiSb

Previous studies of semiconductor thermoelectric materials obtained by doping *p-RNiSb* (*R – Er, Tm, Lu*) with *Zr* or *Sc* atoms by substituting rare earth metal atoms in the crystallographic position 4*a* [8 – 14] made it possible to understand the mechanisms of energy state generation. Thus, replacing *Er* ($5d^06s^2$) or *Lu* atoms with *Zr* ($4d^25s^2$) atoms or occupying the last vacancies in position 4*a* generates structural defects of the donor nature (*Zr* has more *d*-electrons than *Er* or *Lu*) [8 – 10]. At the same time, corresponding donor states appear in the ε_g band gap of $Er_{1-x}Zr_xNiSb$ or $Lu_{1-x}Zr_xNiSb$ semiconductors. In the case of substitution of *R* atoms for *Sc* atoms in position 4*a* in semiconductors $Er_{1-x}Sc_xNiSb$, $Tm_{1-x}Sc_xNiSb$ and $Lu_{1-x}Sc_xNiSb$, defects of a neutral nature are generated (*Er*, *Tm*, *Lu* and Sc atoms are located in the same group of the Periodic System of Chemical Elements) [11 – 14]. However, when *Sc* atoms occupy vacancies in position 4*a* [7], defects of the acceptor nature and the corresponding acceptor states ε_A^{Vac} disappear, and defects of the donor nature and donor states are generated. At the same time, at all concentrations of $Er_{1-x}Sc_xNiSb$, $Tm_{1-x}Sc_xNiSb$ and $Lu_{1-x}Sc_xNiSb$, holes remain current carriers, and the Fermi level ε_F lies near the valence band ε_V.

The first step in the study of the new semiconductor thermoelectric material $Lu_{1-x}V_xNiSb$ is the modeling of its properties, which is the subject of this work. The difficulty of such modeling lies in the unpredictability of the behavior of *V* atoms. First, *V* atoms can be in different valence states (from +1 to +5). Secondly, when *V* atoms are introduced into the structure of the *LuNiSb* compound by substituting *Lu* atoms in the 4*a* position, they can occupy other crystallographic positions. After all, the atomic radius of *V* ($r_V = 0.134$ nm) is much smaller than that of *Lu* ($r_{Lu} = 0.173$ nm) and *Sb* ($r_{Sb} = 0.159$ nm) and is close to the atomic radius of *Ni* (($r_{Ni} = 0.125$ nm). Therefore, changes are possible in the structure of the semiconductor $Lu_{1-x}V_xNiSb$ associated with the occupation of different positions by *V* atoms. In particular, *V* atoms are able to occupy the 4*c* position by

occupying vacancies and/or replacing *Ni* atoms. The latter will lead to the generation of structural defects of an acceptor nature. The following results of modeling the properties of the semiconductor solid solution $Lu_{1-x}V_xNiSb$ will show the prospects of its use as an effective thermoelectric material.

Research methods

Thermodynamic, structural, energy, and kinetic properties of the new semiconductor solid solution $Lu_{1-x}V_xNiSb$, obtained by doping the *p-LuNiSb* semiconductor by replacing *Lu* atoms with *V* atoms in the crystallographic position 4*a*, were simulated. DFT calculations were performed using the Vienna Ab initio Simulation Package VASP v. 5.4.4 [15] with potentials of the PAW type [16]. The exchange-correlation functional Perdew-Burke-Enzerhoff in the generalized gradient approximation (GGA) Monkhorst-Pack [17] for the *k*-grid 11 × 11 × 11 [18] was used. In all calculations, the plane wave cutoff was set to 400 eV. A supercell approach was used for mixed-arrangement crystal structures. In this case, lattice symmetry was reduced and all unique distributions of atoms were generated using a combinatorial approach [19]. The lattice parameters for such structures were optimized by a variable lattice volume, which was then selected by the universal equation of state [20]. The electronic kinetic coefficients were calculated using the Exciting code [21] (FLAPW - Full Potential Linearized Augmented Plane Waves method) by solving the linearized Boltzmann equation in the approximation of a constant relaxation time [22 – 25]. The modeling of the distribution of the density of electronic states (DOS) was carried out using the Korringa-Kohn-Rostoker (KKR) method (AkaiKKR software package [26]) in the Coherent Potential Approximation (CPA) and Local Density Approximation (LDA) for exchange correlation potential with the Moruzzi-Janak-Williams (MJW) parameterization [27]. The accuracy of calculating the position of the Fermi level ε_F is ± 6 meV.

Modeling of structural and thermodynamic properties of $Lu_{1-x}V_xNiSb$

Based on the assumption that there is a continuous solid solution of the substitution $Lu_{1-x}V_xNiSb$, x = 0–1.0, the change in values of the unit cell period a(x) for the ordered variant of the crystal structure was calculated (Fig. 2, curve 1). In this case, all crystallographic positions are occupied by atoms corresponding to the *MgAgAs* structural type [1], and *V* atoms replace *Lu* atoms in position 4*a*. Modeling the change in the period of the $Lu_{1-x}V_xNiSb$, x = 0–1.0, shows a monotonous decrease in the values of a(x) (Fig. 2, curve 1). The obtained result is logical, since the substitution of large *Lu* atoms (r_{Lu} = 0.173 nm) with much smaller *V* atoms (r_V = 0.134 nm) in position 4*a* should lead to a decrease in the period of the unit cell a(x) $Lu_{1-x}V_xNiSb$. Such structural changes will lead to the formation of defects of a donor nature in the crystal structure of the semiconductor, and impurity donor states ε_D^V will be generated in the band gap ε_g $Lu_{1-x}V_xNiSb$ [28] (*V* has more *d*-electrons than *Lu*).

Modeling of thermodynamic characteristics in the approximation of harmonic oscillations of atoms for a hypothetical solid solution of $Lu_{1-x}V_xNiSb$, x = 0–1.0, allows us to establish the energetic feasibility of the existence of such a substitution solid solution. For this purpose, a simulation of the

change in the values of the mixing enthalpy $\Delta H_{mix}(x)$ $Lu_{1-x}V_xNiSb$, x = 0–1.0, was carried out (Fig., curve 2). The calculation shows the energetic expediency of the existence of a solid solution of substitution $Lu_{1-x}V_xNiSb$ only at concentrations x = 0–0.10. This is evidenced by the low values of the mixing enthalpy $\Delta H_{mix}(x)$. At higher concentrations of V, x > 0.10, delamination occurs (spinoid phase decay).

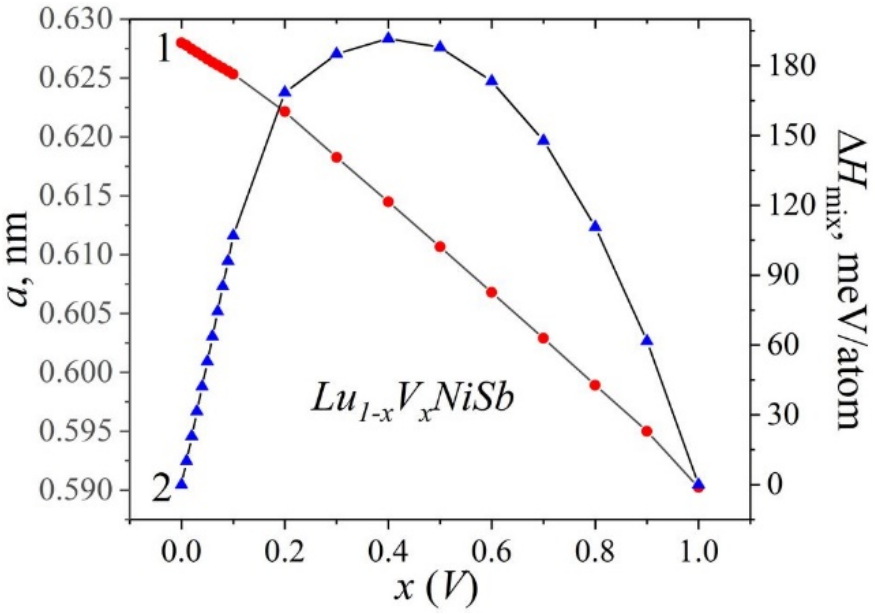

Fig. 2. Modeling of changes in the values of the period of the elementary cell a(x) (1) and enthalpy of mixing $\Delta H_{mix}(x)$ (2) $Lu_{1-x}V_xNiSb$

Modeling of the electronic structure of $Lu_{1-x}V_xNiSb$

To predict the behavior of the Fermi level ε_F, the band gap ε_g, and the kinetic characteristics of $Lu_{1-x}V_xNiSb$, the distribution of the density of electronic states (DOS) was first calculated for two variants of the structure of the *LuNiSb* compound (Fig. 3). As can be seen from fig. 3, the simulation results are diametrically opposed. Thus, for the first, ordered version of the structure, when *V* atoms replace *Lu* atoms in position 4*a* (Fig. 3a), DOS simulation places the Fermi level ε_F near the conduction band ε_C. This is typical for semiconductors of the electronic conductivity type [28]. In the case of a disordered version of the *LuNiSb* structure (Fig. 3b), when there are vacancies (Vac) in positions 4*a* of Lu atoms and 4*c* of *Ni* atoms (Fig. 1), the Fermi level ε_F lies near the valence band ε_V. In this case, the DOS simulation corresponds to hole-type semiconductors [28].

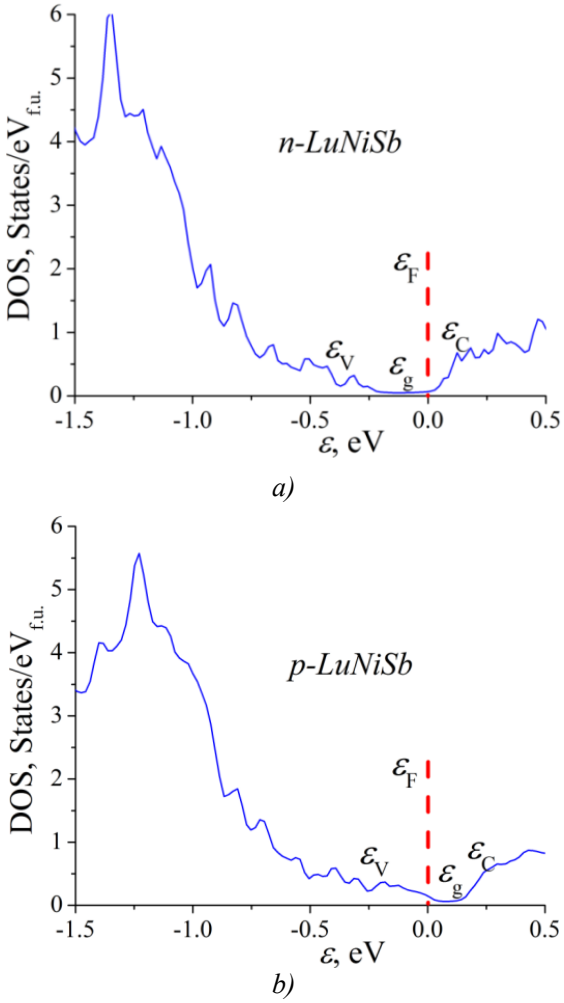

Fig. 3. Calculation of the distribution of the DOS density of electronic states for the ordered (a) and disordered (b) versions of the structure of the LuNiSb compound

Since the replacement of *Lu* atoms by *V* atoms generates structural defects of the donor nature, and in the band gap ε_g of the semiconductor $Lu_{1-x}V_xNiSb$ near the conduction band ε_C, donor states ε_D^V appear that form the donor band, then already at a $Lu_{0.99}V_{0.01}NiSb$ concentration, the Fermi level ε_F will approach the edge of the conduction zone ε_C (Fig. 4). At higher concentrations of *V* atoms, the concentration of donor states ε_D^V and the strength of the donor zone will increase, and the Fermi level ε_F will approach, and later cross the conduction band ε_C: a dielectric-metal conduction transition will occur, which is the Anderson transition [28]. The approach of the Fermi level ε_F to the conduction band ε_C will also lead to a change in the sign of the thermopower coefficient $\alpha(T, x)$ from positive (for *p-LuNiSb*) to negative, and electrons will become the main current carriers of $Lu_{1-x}V_xNiSb$. In addition, the intersection of the Fermi level ε_F and the edge of the conduction band ε_C will change the type of conductivity of the semiconductor from activation (for *p-LuNiSb*) to metallic [28]: in the experiment on the temperature dependences of the resistivity $\ln(\rho(1/T))$ $Lu_{1-x}V_xNiSb$ will disappear activation areas, and the resistance values ρ will increase with temperature.

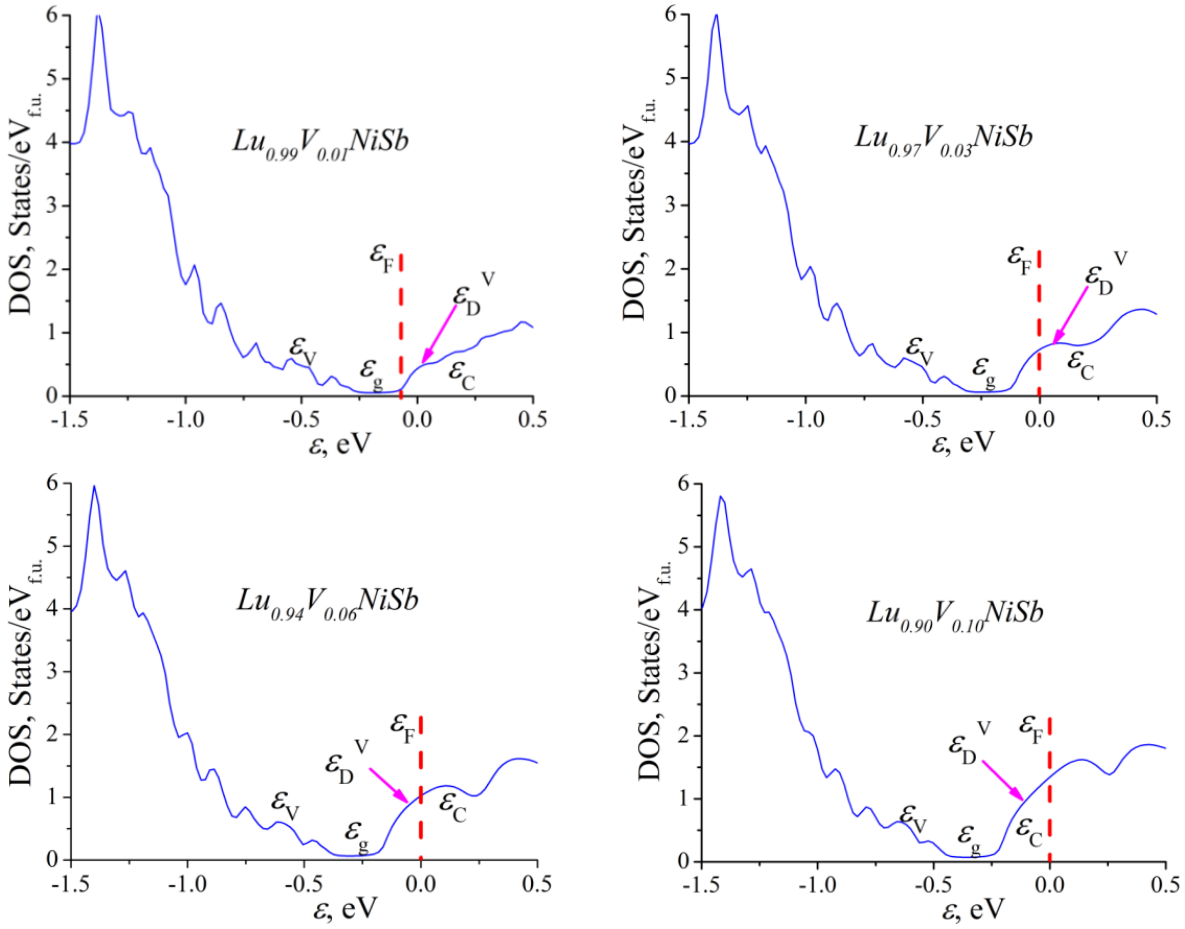

Fig. 4. Calculation of the distribution of the density of electronic states of DOS $Lu_{1-x}V_xNiSb$

Modeling of the electrokinetic properties of $Lu_{1-x}V_xNiSb$

In fig. 5 shows the results of modeling the temperature dependences of the specific resistance $\rho(T, x)$ and the thermopower coefficient $\alpha(T,x)$ $Lu_{1-x}V_xNiSb$, $x \leq 0.10$. The result of calculating the temperature dependences of $\rho(T)$ and $\alpha(T)$ for *p-LuNiSb* coincides with that obtained earlier [2, 8, 9] and shows a decrease in the resistance values when holes are activated from the acceptor states ε_A^{Vac} into the valence band ε_V. At the same time, the holes are the main carriers of the current, which is indicated by the positive values of the thermopower coefficient $\alpha(T)$. This behavior of electrical resistance $\rho(T)$ is characteristic of semiconductors, when the number of free current carriers increases due to their thermal activation from the Fermi level ε_F to the continuous energy zone [28].

Doping *p-LuNiSb* with *V* atoms by substituting *Lu* atoms in the 4*a* position generates structural defects of a donor nature in the semiconductor $Lu_{1-x}V_xNiSb$, and corresponding donor states ε_D^V appear in the ε_g band gap. As can be seen from fig. 5, at the lowest impurity concentration ($x = 0.01$) in the temperature range $T = 10$–170 K, the values of specific electrical resistance $\rho(T)$ in the semiconductor $Lu_{0.99}V_{0.01}NiSb$ increase. At the same time, the main current carriers, as in the case of *p-LuNiSb*, are holes, as indicated by the positive values of the thermopower coefficient $\alpha(T)$.

Such an increase in the values of electrical resistance ρ(*T*) is not a manifestation of metallic conductivity, when the increase in resistance is associated with the action of current carrier scattering mechanisms. In the case of the semiconductor $Lu_{0.99}V_{0.01}NiSb$, the increase in the values of specific electrical resistance ρ(*T*) at temperatures *T* = 10–170 K is of a concentration nature. After all, the basic semiconductor *p-LuNiSb* contains acceptor states ε_A^{Vac}, which in $Lu_{0.99}V_{0.01}NiSb$ with increasing temperature capture electrons from the generated donor states ε_D^V, which reduces the concentration of free holes and increases the degree of compensation and the value of electrical resistance ρ(*T*). At the same time, the Fermi level ε_F drifts from the edge of the valence band ε_V to the middle of the band gap ε_g, which it will cross at a temperature of $T \approx 65$ K. At higher temperatures, $T > 65$ K, the sign of the thermopower coefficient α(*T*) $Lu_{0.99}V_{0.01}NiSb$ becomes negative, the Fermi level ε_F now drifts to the conduction band ε_C. The extremum on the dependence of the specific resistance ρ(*T*) of $Lu_{0.99}V_{0.01}NiSb$ at a temperature of $T \approx 170$ K and the subsequent decrease in the electrical resistance values (Fig. 5, inset) is also of a concentration nature. All acceptor states are compensated, but the Fermi level ε_F lies in the band gap ε_g near the edge of the conduction band ε_C and the concentration of free electrons increases during the ionization of donor states ε_D^V.

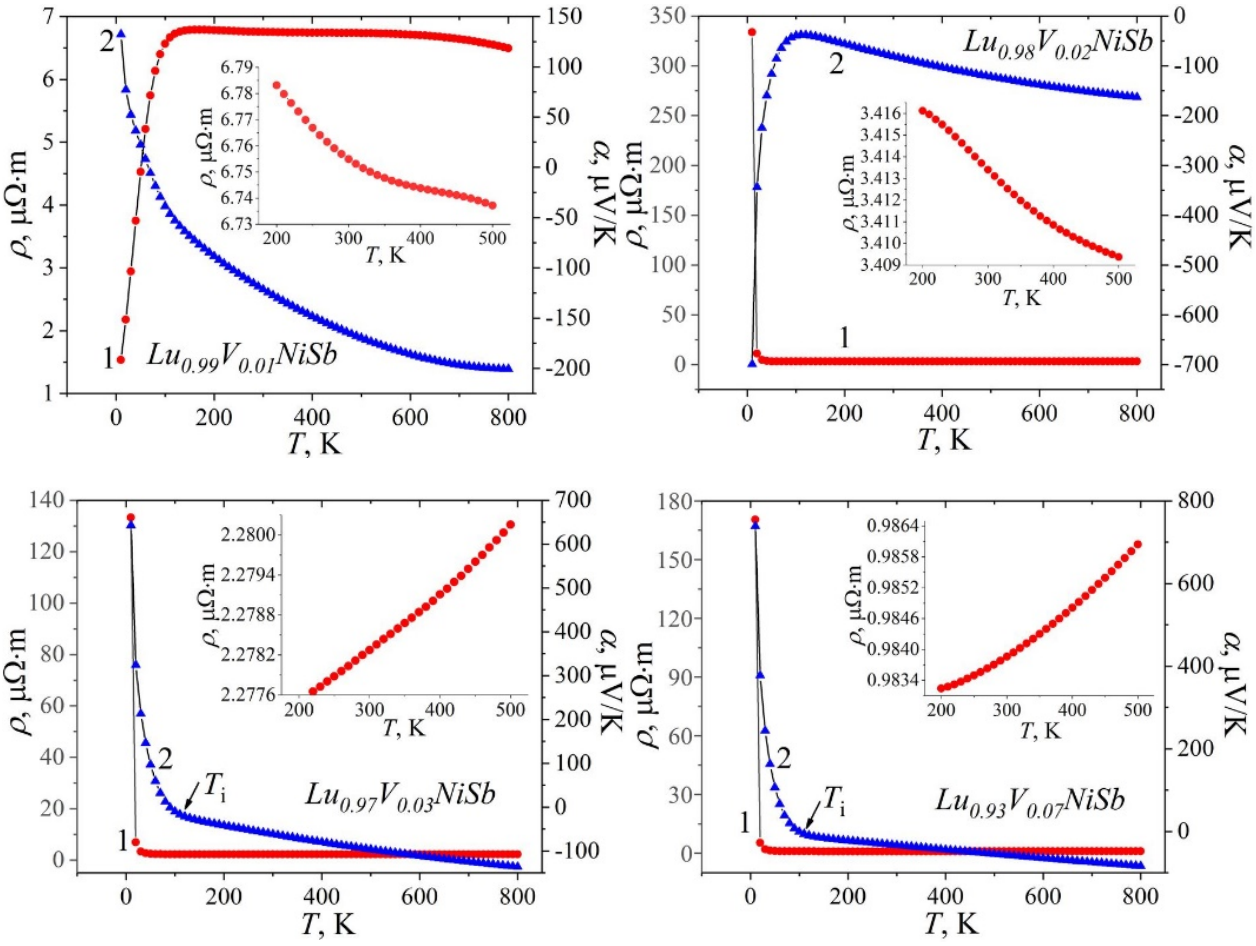

Fig. 5. Modeling of the change in the values of specific electrical resistance ρ(T,x) (1) and thermopower coefficient α(T,x) (2) $Lu_{1-x}V_xNiSb$

In the $Lu_{0.98}V_{0.02}NiSb$ semiconductor, the temperature dependence of the specific resistance $\rho(T, x)$ at low temperatures does not include the region of increase in resistance values, which was in $Lu_{0.99}V_{0.01}NiSb$ and is associated with a decrease in the concentration of holes during the compensation of the acceptor states ε_A^{Vac} by electrons of ionized donor states ε_D^V. The simulation shows only a rapid decrease in the values of the specific resistance $\rho(T, x)$ from $\rho_{10\ K} = 333.7$ μΩ·m to the values $\rho_{20\ K} = 11.2$ μΩ·m and $\rho_{30\ K} = 4.9$ μΩ·m. At the same time, the sign of the thermopower coefficient $\alpha(T, x)$ $Lu_{0.98}V_{0.02}NiSb$ remains negative at all the investigated temperatures. This behavior of the temperature dependences $\rho(T, x)$ and $\alpha(T, x)$ of $Lu_{0.98}V_{0.02}NiSb$ indicates that all acceptor states ε_A^{Vac} are compensated, the Fermi level ε_F is fixed at the donor states ε_D^V and is in the band gap ε_g near the edge conduction zones ε_C.

The results of modeling the kinetic characteristics of $Lu_{1-x}V_xNiSb$ at higher concentrations of the impurity V, $x \geq 0.03$, indicate the appearance of a significant number of structural defects of an acceptor nature in the semiconductor. This is evidenced by the positive values of the thermopower coefficient $\alpha(T, x)$ at temperatures $T \leq 90$ K in the semiconductor $Lu_{0.97}V_{0.03}NiSb$ and $T \leq 100$ K in the semiconductor $Lu_{0.93}V_{0.07}NiSb$ (Fig. 5). We noted above that V atoms ($3d^34s^2$) can occupy different crystallographic positions in $Lu_{1-x}V_xNiSb$, in particular, the 4*c* position of *Ni* atoms ($3d^84s^2$). The latter will lead to the generation of structural defects of an acceptor nature (V has fewer 3*d*-electrons than *Ni*) and the appearance of impurity acceptor states ε_A^{Ni} in the band gap. At these temperatures, holes are the main current carriers.

At higher temperatures $T > T_i$, the sign of the thermopower coefficient $\alpha(T, x)$ is inverted from positive to negative (Fig. 5), and electrons become the main current carriers. The fact that the inversion of the sign of the thermopower coefficient $\alpha(T, x)$ occurs at temperatures $T_i > 90$–100 K indicates that in the band gap ε_g of a semiconductor, the depth of donor states ε_D^V relative to the edge of the conduction band ε_C is greater than that of acceptor states of ε_A^{Ni} states relative to the valence band edge ε_V. Therefore, at low temperatures, acceptors are first ionized, and at higher temperatures, $T > T_i$, donors are ionized. Such a change in the sign of the thermopower coefficient $\alpha(T, x)$ $Lu_{1-x}V_xNiSb$ (of the type of main current carriers) shows that at concentrations of V atoms, $x \geq 0.03$, the number of structural defects of the donor nature outweighs the number of defects of the acceptor nature.

Modeling the temperature dependences of the specific electrical resistance $\rho(T, x)$ $Lu_{1-x}V_xNiSb$, $x \geq 0.03$, shows that in the semiconductor $Lu_{0.97}V_{0.03}NiSb$, the resistance values decrease in the temperature range $T = 10$–160 K, and only increase at higher temperatures (Fig. 5, inset). In the case of the semiconductor $Lu_{0.93}V_{0.07}NiSb$, a decrease in the values of the specific resistance $\rho(T, x)$ occurs at temperatures $T = 10$–110 K, after which the resistance increases. This behavior $\rho(T, x)$ $Lu_{1-x}V_xNiSb$, $x \geq 0.03$, shows that at low temperatures the Fermi level ε_F is in the band gap ε_g of the semiconductor, and at higher temperatures it crosses the edge of the conduction band ε_C and moves along the band of continuous energies. A dielectric-metal conduction transition will occur, which is an Anderson transition [28]. In the case of experimental measurements on the temperature dependence of the

specific electrical resistance ln(ρ(1/*T*)) $Lu_{1-x}V_xNiSb$, there will be no high-temperature activation areas, and the resistance values ρ will increase with temperature.

Modeling of thermoelectric characteristics of $Lu_{1-x}V_xNiSb$

An exhaustive characteristic of a thermoelectric material in terms of its efficiency in converting thermal energy into electrical energy is the value of the thermoelectric factor at different temperatures. In fig. 6 shows the results of *ZT* modeling in the temperature range $T = 10–800$ K for the semiconductor solid solution $Lu_{1-x}V_xNiSb$, $x \leq 0.10$. Note that the electronic component of thermal conductivity κ_e was taken into account when modeling the values of the thermoelectric factor *Z*.

From fig. 6, we can see that in the semiconductor solid solution $Lu_{0.99}V_{0.01}NiSb$ at a temperature of $T \approx 620$ K, the thermoelectric factor *Z* are maximal and reach the values of $ZT = 0.62$. The values of the thermoelectric factor obtained by mathematical modeling for $Lu_{1-x}V_xNiSb$, $x \leq 0.10$, testify to the prospects of the obtained semiconductor solid solution as a thermoelectric material.

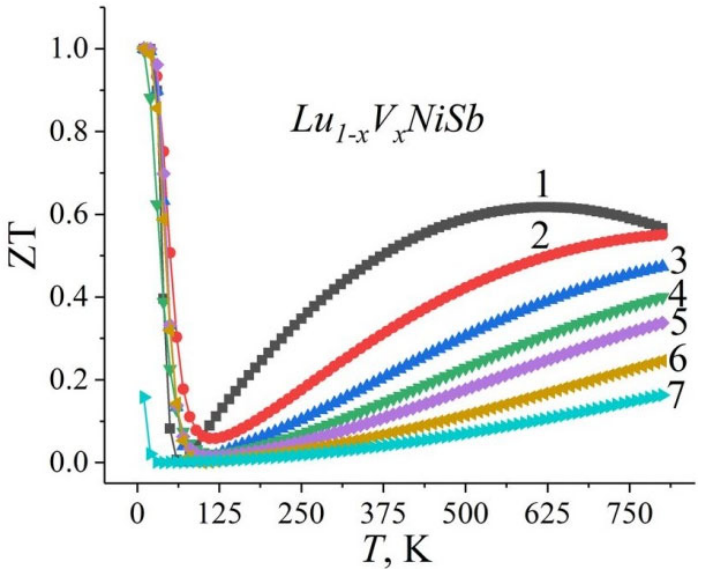

Fig. 6. Modeling the change in ZT values of $Lu_{1-x}V_xNiSb$ with increasing temperature:
1 – x = 0.01; 2 – x = 0.02; 3 – x = 0.03; 4 – x = 0.04;
5 – x = 0.05; 6 – x = 0.07; 7 – x = 0.10

Conclusion

The result of modeling the crystal and electronic structures, thermodynamic and kinetic properties of $Lu_{1-x}V_xNiSb$ is establishing the nature of the generated energy states. It is shown that the semiconductor solid solution $Lu_{1-x}V_xNiSb$ is a promising thermoelectric material, and at a temperature of $T \approx 620$ K and a concentration of $Lu_{0.99}V_{0.01}NiSb$, the thermoelectric factor *Z* values reach the maximum values of $ZT = 0.62$. It was established that the impurity atoms of *V* ($3d^3 4s^2$), introduced

into the structure of the *LuNiSb* compound, simultaneously occupy the crystallographic positions 4*a* of *Lu* atoms ($5d^16s^2$) and 4*c* of *Ni* atoms ($3d^84s^2$) in different ratios, generating in the band gap ε_g impurity donor ε_D^V and acceptor ε_A^{Ni} energy states. The ratio of concentrations of donors and acceptors determines the location of the Fermi level ε_F and the mechanisms of electrical conductivity.

References

1. Romaka V. V., Rogl P. F., Carlini R., Fanciulli C. (2017). Prediction of the Thermoelectric Properties of Half-Heusler Phases from the Density Functional Theory. – P. 286 - 323. In "*Alloys and Intermetallic Compounds. From Modeling to Engineering*". Genova, Italy: CRC Press Taylor & Francis Group. International Standard Book Number–13: 978–1–4987–4143–9.
2. Romaka V. A., Stadnyk Yu. V., Krayovskyy V. Ya., Romaka L. P., Guk O. P., Romaka V. V., Mykyuchuk M. M., Horyn A. M. (2020). *Novitni termochutlyvi materialy ta peretvoriuvachi temperatury* [*New thermosensitive materials and temperature converters*]. Lviv: Lvivska Polytechnika [in Ukrainian]. DOI: https://opac.lpnu.ua/bib/1131184.
3. Hartjes K., Jeitschko W. (1995). Crystal structure and magnetic properties of the lanthanoid nickel antimonides *LnNiSb* (*Ln = La–Nd, Sm, Gd–Tm, Lu*). *J. Alloys Compd*., 226, 81-86. DOI: https://doi.org/10.1016/0925-8388(95)01573-6.
4. Anatychuk L. I. (1979). *Termoelementy i termoelectricheskiie ustroistva. Spravochnik.* [*Thermoelements and thermoelectric devices. Reference book*]. Kyiv: Naukova dumka [in Russian].
5. Karla I., Pierre J., Skolozdra R. V. (1998). Physical properties and giant magnetoresistance in R*NiSb* compounds. *J. Alloys Compd*., 265, 42 - 48. DOI: https://doi.org/10.1016/S0925-8388(97)00419-2.
6. Romaka V. V., Romaka L., Horyn A., Rogl P., Stadnyk Yu., Melnychenko N., Orlovskyy M., Krayovskyy V. (2016). Peculiarities of thermoelectric half-Heusler phase formation in *Gd-Ni-Sb* and *Lu-Ni-Sb* ternary systems. *J. Solid State Chem*., 239, 145 - 152. https://doi.org/10.1016/j.jssc.2016.04.029).
7. Romaka V.V., Romaka L., Horyn A., Stadnyk Yu. (2021). Experimental and theoretical investigation of the *Y–Ni–Sb* and *Tm–Ni–Sb* systems. *J. Alloys Compd*., 855, 157334–12. DOI: https://doi.org/10.1016/j.jallcom.2020.157334.
8. Romaka V. A., Stadnyk Yu. V., Romaka L. P., Pashkevych V. Z., Romaka V. V., Horyn A. M., Demchenko P. Yu. (2021). Study of structural, thermodynamic, energy, kinetic and magnetic properties of thermoelectric material $Lu_{1-x}Zr_xNiSb$. *J. Thermoelectricity*, 1, 32 - 48. DOI: http://jt.inst.cv.ua/jt/jt_2021_01_en.pdf.
9. Romaka V. A., Stadnyk Yu., Romaka L., Horyn A., Pashkevych V., Nychyporuk H., Garanyuk P. (2022). Investigation of Thermoelectric Material Based on $Lu_{1-x}Zr_xNiSb$ Solid Solution. I. Experimental Results. *J. Phys. Chem. Sol. State*, 23, 235-241. DOI: 10.15330/pcss.23.2.235-241.
10. Romaka V. A., Stadnyk Yu., Romaka L., Krayovskyy V., Horyn A., Klyzub P., Pashkevych V. (2020). Study of structural, electrokinetic and magnetic characteristics of the $Er_{1-x}Zr_xNiSb$ Semiconductor. *J. Phys. Chem. Sol. State*, 21, 689-694. DOI: 10.15330/pcss.21.4.689-694.

11. Wolańska I., Synoradzki K., Ciesielski K., Załęski K., Skokowski P., Kaczorowski D. (2019). Enhanced thermoelectric power factor of half-Heusler solid solution $Sc_{1-x}Tm_xNiSb$ prepared by high-pressure hightemperature sintering method. *Materials Chemistry and Physics*, 227, 29 - 35. DOI: https://doi.org/10.1016/j.matchemphys.2019.01.056.
12. Romaka V. V., Romaka V. A., Stadnyk Yu. V., Romaka L. P., Demchenko P. Y., Pashkevych V. Z., Horyn A. M. (2022). Features of mechanisms of electrical conductivity in semiconductive solid solution $Lu_{1-x}Sc_xNiSb$. *Ukr. J. Phys*., 67, 370-379. DOI: https://doi.org/10.15407/ujpe67.5.370.
13. Romaka V. A., Stadnyk Yu. V., Romaka V. V., Demchenko P. Yu., Romaka L. P., Pashkevych V. Z., Horyn A. M., Horpeniuk A. Ya. (2021). Investigation of properties of new thermoelectric material $Lu_{1-x}Sc_xNiSb$. *J. Thermoelectricity*, 2, 18 - 30. DOI: http://jt.inst.cv.ua/jt/jt_2021_02_en.pdf.
14. Romaka V. A., Stadnyk Yu., Romaka L., Krayovskyy V., Klyzub P., Pashkevych V., Horyn A., Garanyuk P. (2021). Synthesis and Electrical Transport Properties of $Er_{1-x}Sc_xNiSb$ Semiconducting Solid Solution. *J. Phys. Chem. Sol. State*, 22, 146–152. DOI:10.15330/pcss.22.1.146-152.
15. Kresse G., Hafner J. (1993). Ab initio molecular dynamics for liquid metals. *Phys. Rev*., B 47, 558 - 561.
16. Kresse G., Joubert D. (1999). From ultrasoft pseudopotentials to the projector augmented-wave method. *Phys. Rev*., B 59, 1758 - 1775.
17. Perdew J. P., Burke K., Ernzerhof M. (1976). Generalized gradient approximation made simple. *Phys. Rev. Lett*., 77(18), 3865–8. https://doi.org/10.1103/PhysRevLett.77.3865.
18. Monkhorst H. J., Pack J. K. (1976). Special points for Brillouin-zone integrations. *Phys. Rev*., B 13, 5188 - 5192.
19. Okhotnikov K., Charpentier T., Cadars S. (2016). Supercell program: a combinatorial structure-generation approach for the local-level modeling of atomic substitutions and partial occupancies in crystals. J. Cheminform, 8(17), 1 - 15.
20. Vinet P., Rose J. H., Jr Ferrante J. S. (1989). Universal features of the equation of state of solids. *J. Phys.: Condens. Matter*., 1, 1941 - 1964.
21. Gulans A., Kontur S., Meisenbichler C., Nabok D., Pavone P., Rigamonti S., Sagmeister S., Werner U., Draxl C. (2014). Exciting – a full-potential all-electron package implementing density-functional theory and many-body perturbation theory. *J. Phys.: Condens Matter*., 26, 363202, 1 - 24.
22. Nag B. R. (1996). *Electron Transport in Compound Semiconductors*. Berlin: Springer Verlag.
23. Mahan G. D. and Sofo J. O. (1996). The best thermoelectric. *Proc. Natl. Acad. Sci. USA*, 93 7436.
24. Scheidemantel T. J., Ambrosch-Draxl C., Thonhauser T., Badding H. V., and Sofo J. O. (2003). Transport coefficients from first-principles calculations. *Phys. Rev*., B 68, 125210.
25. Babak V. P., Babak S. V., Myslovych M. V., Zaporozhets A. O., Zvaritch V. M. (2020). Technical provision of diagnostic systems. *Studies in Systems, Decision and Control*, 281, 91 - 133. https://doi.org/10.1007/978-3-030-44443-3_4
26. Schruter M., Ebert H., Akai H., Entel P., Hoffmann E., Reddy G. G. (1995). First-principles

investigations of atomic disorder effects on magnetic and structural instabilities in transition-metal alloys. *Phys. Rev*. B 52, 188 - 209

27. Moruzzi V. L., Janak J. F., Williams A. R. (1978). *Calculated Electronic Properties of Metals*. NY: Pergamon Press.
28. Shklovskii B. I. and Efros A. L. (1984). *Electronic properties of doped semiconductors*. Berlin, Heidelberg, Springer-Verlag. DOI: 10.1007/978-3-662-02403-4.

Submitted 15.02.2022

Ромака В. А., *док. техн. наук*, *канд. фіз.-мат., професор* [1]
Стадник Ю. В, *канд. хім. наук*[2]
Ромака Л. П., *канд. хім. наук*[2]
Плевачук Ю. О., *док. фіз.-мат.*[2]
Ромака В. В., *док. техн. наук*, *канд. хім. наук*[3]
Горинь А. М., *канд. хім. наук*[2]
Пашкевич В. З., *канд. тех. наук*[1]
Зелінський А. В., *канд. хім. наук*[2]

[1]Національний університет "Львівська політехніка",
вул. С. Бандери, 12, Львів, 79013, Україна;
[2]Львівський національний університет ім. І. Франка,
вул. Кирила і Мефодія, 6, Львів, 79005, Україна;
[3]Інститут дослідження твердого тіла ім. Лейбніца, Гельмгольц штрасе,
20, 01069 Дрезден, Німеччина

ДОСЛІДЖЕННЯ ТЕРМОЕЛЕКТРИЧНОГО МАТЕРІАЛУ $Lu_{1-x}V_xNiSb$: МОДЕЛЮВАННЯ ВЛАСТИВОСТЕЙ

Результатом моделювання кристалічної та електронної структур, термодинамічних та кінетичних властивостей $Lu_{1-x}V_xNiSb$ є встановлення природи генерованих енергетичних станів. Показано, що напівпровідниковий твердий розчин $Lu_{1-x}V_xNiSb$ є перспективним термоелектричним матеріалом, а за температури T≈620 K та концентрації $Lu_{0.99}V_{0.01}NiSb$ значення добротності досягають максимальних значень ZT = 0.62. Встановлено, що домішкові атоми V ($3d^34s^2$), уведені до структури сполуки LuNiSb, одночасно у різних

співвідношеннях займають кристалографічні позиції 4a атомів Lu ($5d^16s^2$) та 4c атомів Ni ($3d^84s^2$), генеруючи в забороненій зоні ε_g домішкові донорні ε_D^V та акцепторні ε_A^{Ni} енергетичні стани. Співвідношення концентрацій донорів та акцепторів визначає розташування рівня Фермі ε_F та механізми електропровідності. Бібл. 28, рис.6.

Ключові слова: електронна структура, термоелектрична добротність, електроопір, коефіцієнт термоЕРС.

References

1. Romaka V. V., Rogl P. F., Carlini R., Fanciulli C. (2017). Prediction of the Thermoelectric Properties of Half-Heusler Phases from the Density Functional Theory. – P. 286 - 323. In "*Alloys and Intermetallic Compounds. From Modeling to Engineering*". Genova, Italy: CRC Press Taylor & Francis Group. International Standard Book Number–13: 978–1–4987–4143–9.
2. Romaka V. A., Stadnyk Yu. V., Krayovskyy V. Ya., Romaka L. P., Guk O. P., Romaka V. V., Mykyuchuk M. M., Horyn A. M. (2020). *Novitni termochutlyvi materialy ta peretvoriuvachi temperatury* [*New thermosensitive materials and temperature converters*]. Lviv: Lvivska Polytechnika [in Ukrainian]. DOI: https://opac.lpnu.ua/bib/1131184.
3. Hartjes K., Jeitschko W. (1995). Crystal structure and magnetic properties of the lanthanoid nickel antimonides *LnNiSb* (*Ln = La–Nd, Sm, Gd–Tm, Lu*). *J. Alloys Compd*., 226, 81-86. DOI: https://doi.org/10.1016/0925-8388(95)01573-6.
4. Anatychuk L. I. (1979). *Termoelementy i termoelectricheskiie ustroistva. Spravochnik.* [*Thermoelements and thermoelectric devices. Reference book*]. Kyiv: Naukova dumka [in Russian].
5. Karla I., Pierre J., Skolozdra R. V. (1998). Physical properties and giant magnetoresistance in R*NiSb* compounds. *J. Alloys Compd*., 265, 42 - 48. DOI: https://doi.org/10.1016/S0925-8388(97)00419-2.
6. Romaka V. V., Romaka L., Horyn A., Rogl P., Stadnyk Yu., Melnychenko N., Orlovskyy M., Krayovskyy V. (2016). Peculiarities of thermoelectric half-Heusler phase formation in *Gd-Ni-Sb* and *Lu-Ni-Sb* ternary systems. *J. Solid State Chem*., 239, 145 - 152. https://doi.org/10.1016/j.jssc.2016.04.029).
7. Romaka V.V., Romaka L., Horyn A., Stadnyk Yu. (2021). Experimental and theoretical investigation of the *Y–Ni–Sb* and *Tm–Ni–Sb* systems. *J. Alloys Compd*., 855, 157334–12. DOI: https://doi.org/10.1016/j.jallcom.2020.157334.
8. Romaka V. A., Stadnyk Yu. V., Romaka L. P., Pashkevych V. Z., Romaka V. V., Horyn A. M., Demchenko P. Yu. (2021). Study of structural, thermodynamic, energy, kinetic and magnetic properties of thermoelectric material $Lu_{1-x}Zr_xNiSb$. *J. Thermoelectricity*, 1, 32 - 48. DOI: http://jt.inst.cv.ua/jt/jt_2021_01_en.pdf.
9. Romaka V. A., Stadnyk Yu., Romaka L., Horyn A., Pashkevych V., Nychyporuk H., Garanyuk P. (2022). Investigation of Thermoelectric Material Based on $Lu_{1-x}Zr_xNiSb$ Solid Solution. I. Experimental Results. *J. Phys. Chem. Sol. State*, 23, 235-241. DOI: 10.15330/pcss.23.2.235-241.
10. Romaka V. A., Stadnyk Yu., Romaka L., Krayovskyy V., Horyn A., Klyzub P., Pashkevych V. (2020). Study of structural, electrokinetic and magnetic characteristics of the $Er_{1-x}Zr_xNiSb$

Semiconductor. *J. Phys. Chem. Sol. State*, 21, 689-694. DOI: 10.15330/pcss.21.4.689-694.

11. Wolańska I., Synoradzki K., Ciesielski K., Załęski K., Skokowski P., Kaczorowski D. (2019). Enhanced thermoelectric power factor of half-Heusler solid solution $Sc_{1-x}Tm_xNiSb$ prepared by high-pressure hightemperature sintering method. *Materials Chemistry and Physics*, 227, 29 - 35. DOI: https://doi.org/10.1016/j.matchemphys.2019.01.056.
12. Romaka V. V., Romaka V. A., Stadnyk Yu. V., Romaka L. P., Demchenko P. Y., Pashkevych V. Z., Horyn A. M. (2022). Features of mechanisms of electrical conductivity in semiconductive solid solution $Lu_{1-x}Sc_xNiSb$. *Ukr. J. Phys*., 67, 370-379. DOI: https://doi.org/10.15407/ujpe67.5.370.
13. Romaka V. A., Stadnyk Yu. V., Romaka V. V., Demchenko P. Yu., Romaka L. P., Pashkevych V. Z., Horyn A. M., Horpeniuk A. Ya. (2021). Investigation of properties of new thermoelectric material $Lu_{1-x}Sc_xNiSb$. *J. Thermoelectricity*, 2, 18 - 30. DOI: http://jt.inst.cv.ua/jt/jt_2021_02_en.pdf.
14. Romaka V. A., Stadnyk Yu., Romaka L., Krayovskyy V., Klyzub P., Pashkevych V., Horyn A., Garanyuk P. (2021). Synthesis and Electrical Transport Properties of $Er_{1-x}Sc_xNiSb$ Semiconducting Solid Solution. *J. Phys. Chem. Sol. State*, 22, 146–152. DOI:10.15330/pcss.22.1.146-152.
15. Kresse G., Hafner J. (1993). Ab initio molecular dynamics for liquid metals. *Phys. Rev*., B 47, 558 - 561.
16. Kresse G., Joubert D. (1999). From ultrasoft pseudopotentials to the projector augmented-wave method. *Phys. Rev*., B 59, 1758 - 1775.
17. Perdew J. P., Burke K., Ernzerhof M. (1976). Generalized gradient approximation made simple. *Phys. Rev. Lett*., 77(18), 3865–8. https://doi.org/10.1103/PhysRevLett.77.3865.
18. Monkhorst H. J., Pack J. K. (1976). Special points for Brillouin-zone integrations. *Phys. Rev*., B 13, 5188 - 5192.
19. Okhotnikov K., Charpentier T., Cadars S. (2016). Supercell program: a combinatorial structure-generation approach for the local-level modeling of atomic substitutions and partial occupancies in crystals. J. Cheminform, 8(17), 1 - 15.
20. Vinet P., Rose J. H., Jr Ferrante J. S. (1989). Universal features of the equation of state of solids. *J. Phys.: Condens. Matter*., 1, 1941 - 1964.
21. Gulans A., Kontur S., Meisenbichler C., Nabok D., Pavone P., Rigamonti S., Sagmeister S., Werner U., Draxl C. (2014). Exciting – a full-potential all-electron package implementing density-functional theory and many-body perturbation theory. *J. Phys.: Condens Matter*., 26, 363202, 1 - 24.
22. Nag B. R. (1996). *Electron Transport in Compound Semiconductors*. Berlin: Springer Verlag.
23. Mahan G. D. and Sofo J. O. (1996). The best thermoelectric. *Proc. Natl. Acad. Sci. USA*, 93 7436.
24. Scheidemantel T. J., Ambrosch-Draxl C., Thonhauser T., Badding H. V., and Sofo J. O. (2003). Transport coefficients from first-principles calculations. *Phys. Rev*., B 68, 125210.
25. Babak V. P., Babak S. V., Myslovych M. V., Zaporozhets A. O., Zvaritch V. M. (2020). Technical provision of diagnostic systems. *Studies in Systems, Decision and Control*, 281, 91 - 133. https://doi.org/10.1007/978-3-030-44443-3_4

26. Schruter M., Ebert H., Akai H., Entel P., Hoffmann E., Reddy G. G. (1995). First-principles investigations of atomic disorder effects on magnetic and structural instabilities in transition-metal alloys. *Phys. Rev*. B 52, 188 - 209
27. Moruzzi V. L., Janak J. F., Williams A. R. (1978). *Calculated Electronic Properties of Metals*. NY: Pergamon Press.
28. Shklovskii B. I. and Efros A. L. (1984). *Electronic properties of doped semiconductors*. Berlin, Heidelberg, Springer-Verlag. DOI: 10.1007/978-3-662-02403-4.

Submitted 15.02.2022

DOI: 10.63527/1607-8829-2022-1-44-54

L. I. Anatychuk, *Academician of NAS of Ukraine*[1,2]
R. G. Cherkez, *dok. phys.– mat. sciences, acting professor*[1,2]
O. M. Porubanyi [2]
A. S. Zhukova [2]

[1]Institute of Thermoelectricity of the NAS and MES of Ukraine,
1 Nauky str., Chernivtsi, 58029, Ukraine,
[2]Yu.Fedkovych Chernivtsi National University, Chernivtsi, Ukraine

EFFECT OF LEG THICKNESS AND HEAT CARRIER VELOCITY ON THE EFFICIENCY OF A PERMEABLE GENERATOR THERMOELEMENT

The paper presents the results of computer research on the influence of leg thickness and gas pumping velocity for a 3D model of a permeable generator thermoelement on the EMF and efficiency. The dependences of the energy characteristics of a thermoelement made of materials based on Bi-Te-Se-Sb are calculated. Bibl. 11, Fig. 3, Table 1.

Key words: permeable thermoelement, computer simulation, electric energy generation, energy characteristics.

Introduction

The most widespread application of thermoelectric energy converters is based on the use of a thermocouple element [1, 2]. Its energy conversion efficiency is determined by the figure of merit parameters Z of the materials used. Therefore, the search for materials with the maximum value of the figure of merit becomes the main task of thermoelectric materials science. However, despite intensive research in this direction, no significant increase in the figure of merit has been observed over the past 20-30 years [3, 4]. The maximum values of the dimensionless figure of merit of thermoelectric materials for industrial use remain at the level of $1 \div 1.2$. Therefore, to improve efficiency, it is necessary to use new, non-traditional approaches, which consist in the use of other nonconventional variants of physical models of thermoelements which are the main component of a thermoelectric power converter.

One of them is the use of thermoelements with a developed internal heat exchange surface, namely permeable thermoelements. In such thermoelements, heat exchange with the heat source and heat sink occurs not only at the junctions, but also in the legs. Already the first theoretical [5] and experimental [6] studies for cooling gas flows have shown their promise. They indicate the possibility of improving the efficiency of energy conversion by a factor of $1.3 \div 1.4$.

However, such studies were conducted for a model that is difficult for practical implementation. Therefore, it is necessary to create and study a more realistic 3D model of a permeable thermoelement, which is the purpose of this paper.

Physical model and its mathematical description

The physical model of a permeable thermoelement, in which heat exchange with the heat carrier occurs not only through the connecting plates, but also with the lateral surfaces of the leg, is shown in Fig. 1. It includes *n* – and *p* – type legs (2, 10) covered by adiabatic insulation 1 and 8, which together form channels 5, 6, 9. Heat carrier 7 flowing through channels 3, 5 and 5, 9, is supplied through channel 6 with temperature T_h. The legs are made of a homogeneous material based on *Bi-Te* with a maximum value of figure of merit *Z* in the temperature range $20 \div 320\ ^{\circ}C$. The temperature dependence of material parameters should be taken into consideration. Connecting plates *c* are made of copper, connecting resistance is 10^{-6} Ohm cm^2. The temperature T_0 of lower connecting plates is thermostated. The *n* – and *p* – type legs are interconnected by a thin layer 14, the thermal conductivity, electrical conductivity and thickness of which are neglected. The material of the legs is homogeneous and isotropic with known temperature dependences: electrical conductivity $\sigma(T)$, the Seebeck coefficient $\alpha(T)$, thermal conductivity $\kappa(T)$. In the thermoelectric medium, the volume effects of Thomson, Joule-Lenz and the Peltier contact effect are taken into consideration. The temperature of heat carrier at the inlet to the thermoelement was assumed to be equal to the temperature of hot junctions. The size of the thermoelement in the direction perpendicular to the plane of the figure is *d*, the value of $d = a$. The planes $d = 0$ and $d = a$ are adiabatic insulations which form channels 5, 6, 9, Friction between the heat carrier and the adiabatic insulations 1, 8 is absent.

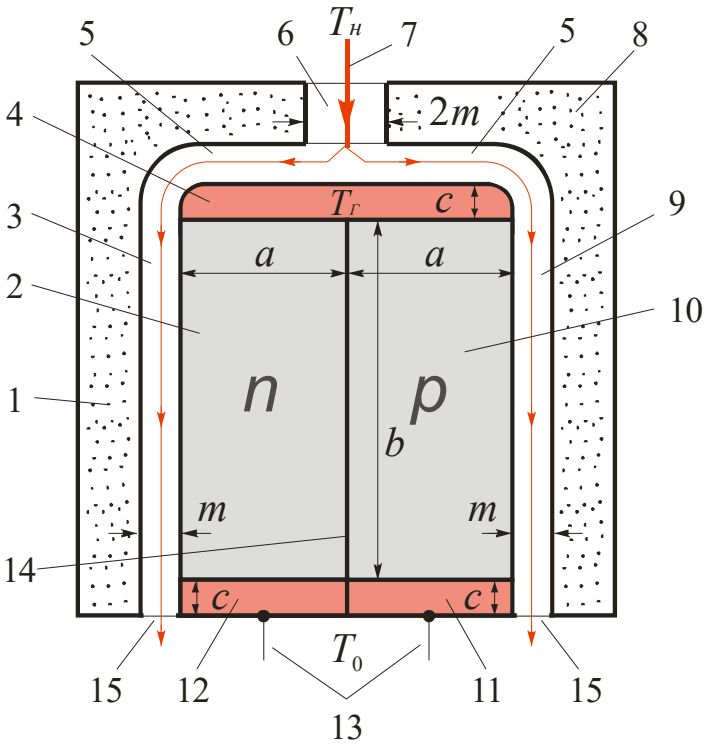

Fig. 1. Physical model of a permeable thermoelement:
1 – adiabatic insulation, 2 – n-type legs, 3 - channels, 4 – connecting plate, 5 - channel, 6 - channel, 7 – heat carrier, 8 – adiabatic insulation, 9 – channel, 10 – p-type leg, 11, 12 – connecting plates, 13 – electric contacts, 14 – layer between n- and p-type legs, 15 – channel outputs

On the lateral surface of legs 2 of connecting plates 4 which are in thermal contact with heat carrier 4, heat exchange is described by the Newton-Richmann law:

$$q_0 = \alpha_T (t - T), \tag{1}$$

where α_T is heat exchange coefficient, T is temperature of thermoelement leg, t is temperature of heat carrier.

The system of equations describing the distribution of temperature and potential in the thermoelectric medium is described by the fundamental laws of conservation of energy and current carriers [7]:

$$\vec{\nabla}\vec{W} = 0 \tag{2}$$

$$\vec{\nabla}\vec{i} = 0 \tag{3}$$

where $\vec{W} = \vec{q} + U\vec{i}$ is energy flux density.

Using the generalized Fourier and Ohm's laws for thermoelectric medium:

$$\vec{q} = -\kappa\vec{\nabla}T + \alpha\vec{i}\,T \tag{4}$$

$$\vec{i} = -\sigma(\vec{\nabla}U + \alpha\vec{\nabla}T) \tag{5}$$

where U is potential, κ is thermal conductivity, α is the Seebeck coefficient, σ is electric conductivity, one can obtain a system of differential equations to find the distribution of temperatures and potentials:

$$\left.\begin{aligned} &\vec{\nabla}\kappa\vec{\nabla}T + \frac{i^2}{\sigma} - T\vec{i}\vec{\nabla}\alpha = 0; \\ &\vec{\nabla}(-\sigma(\vec{\nabla}U + \alpha\vec{\nabla}T)) = 0. \end{aligned}\right\} \tag{6}$$

To describe the motion of the heat carrier in the channel, the system of the Navier-Stokes equations and the continuity equation are used, and for the distribution of heat carrier temperature the thermal conductivity equation is used.

The Navier-Stokes equations and the continuity equation can be written as [8]:

$$\left.\begin{aligned} &\rho\frac{d\vec{\vartheta}}{dt} = \rho\vec{F} - \vec{\nabla}P + \mu\vec{\nabla}^2\vec{\vartheta} + \frac{1}{3}\mu\vec{\nabla}(div\vec{\vartheta}), \\ &div\rho\vec{\vartheta} = 0. \end{aligned}\right\} \tag{7}$$

The left side (7) represents the fluid inertia force. The first term on the right side of (7) is the mass force, the second is the action of surface pressure forces (normal stresses), and the last two terms are the action of the contiguous components of surface forces (internal friction forces).

Heat exchange in the fluid is described by the thermal conductivity equation [9]:

$$\rho C_p\left(\frac{\partial T}{\partial t} + (\vec{\vartheta}\vec{\nabla})T\right) = -(\vec{\nabla}\vec{q}) + \sum_{i,j}\tau_{ij}S_{ij} - \frac{T}{\rho}\frac{\partial\rho}{\partial T}\bigg|_P\left(\frac{\partial\rho}{\partial t} + (\vec{\vartheta}\vec{\nabla})P\right) + Q \tag{8}$$

where ρ is the density, C_p is the heat capacity, T is the temperature, $\vec{\vartheta}$ – is the fluid velocity vector, q is the heat flux density, P is the pressure, τ_{ij} is the viscous stress tensor, where η is the viscosity, I is the unit tensor, $\vec{S}_{ij}$ is the strain rate tensor.

Since this problem is considered for the steady-state case, the left side of the first equation in system (7) is equal to zero. We also neglect the influence of mass forces, then the first term on the left side of the same equation is also equal to zero. Eq.(8) must also be written for the steady-state case, and heating of fluid due to internal friction, fluid compression, as well as heating of fluid due to internal heat sources are neglected. Then the system of Navier-Stokes, continuity and thermal conductivity equations for this problem will be written in the form:

$$\left.\begin{aligned} &-\vec{\nabla}P+\mu\vec{\nabla}^2\vec{\vartheta}+\frac{1}{3}\mu\vec{\nabla}(div\vec{\vartheta})=0,\\ &div\rho\,\vec{\vartheta}=0,\\ &\rho C_p(\vec{\vartheta}\vec{\nabla})T+\vec{\nabla}\vec{q}=0. \end{aligned}\right\} \tag{9}$$

Boundary conditions describing the conjugate problem used in this task have the following form:

– for thermoelectric medium:

$$\text{temperature - } \begin{matrix} T|_0=300K \\ T|_{z_h}=\alpha_T(T_h-T) \end{matrix}, \tag{10}$$

$$\text{potential - } \begin{matrix} U|_0=0 \\ U|_{x_3}=U_0 \end{matrix}, \tag{11}$$

– for heat carrier:

$$\text{velocity - } \begin{matrix} \vartheta|_0=\vartheta_0 \\ \vartheta|_{z_h}=P_0=0 \\ \vartheta|_{S_б}=0 \end{matrix}, \tag{12}$$

$$\text{inlet temperature - } t|_{z_h}=T_h \tag{13}$$

where ϑ_0 is the initial velocity of the heat carrier, U_0 is a fixed value of the potential, S_0 is the lateral surface of the thermoelement.

Implementation of the stated problem in the Comsol Multiphysics software package

To calculate the problem, the Comsol Multiphysics software package was chosen, namely, the equation in partial derivatives (*PDE modes)*. Where one of the ways to represent the equation is the coefficient form:

$$e_a \frac{\partial^2 \vec{u}}{\partial t^2} + d_a \frac{\partial \vec{u}}{\partial t} + \vec{\nabla}(-c\vec{\nabla}\vec{u} - \alpha\vec{u} + \gamma) + \beta\vec{\nabla}u + a\vec{u} = f \tag{14}$$

This equation is used for a thermoelectric medium and reduced to the form $\vec{\nabla}(-c\vec{\nabla}\vec{u}) = 0$. For this, e_a, d_a, α, γ, β, a are set to zero, and the value c is written in the form of a matrix:

$$c = \begin{pmatrix} \kappa + \alpha^2\sigma T + \sigma U\alpha & \alpha T\sigma + \sigma U \\ \alpha\sigma & \sigma \end{pmatrix}. \tag{15}$$

Moreover, vector $\vec{u}$ has also the form of a matrix:

$$\vec{u} = \begin{pmatrix} T \\ U \end{pmatrix}. \tag{16}$$

The Comsol Multiphysics – Non-Isothermal Flow module [11] is used to describe the motion and heat transfer of a fluid. The module includes the system of Navier-Stokes equations, the continuity equation and the heat transfer equation for a fluid that changes in time or in a steady-state mode. The calculation of the given model in the steady-state mode was carried out according to the relations:

$$\left.\begin{aligned} &\rho(\vec{\vartheta}\vec{\nabla})\vec{u}_2 = \vec{\nabla}\left[-PI + \mu(\vec{\nabla}\vec{\vartheta} + (\vec{\nabla}\vec{\vartheta})^T) - \frac{2}{3}\mu(\vec{\nabla}\vec{\vartheta})I\right], \\ &\vec{\nabla}(\rho\vec{\vartheta}) = 0, \\ &\rho C_p\vec{\vartheta}\vec{\nabla}T + \vec{\nabla}(\kappa\vec{\nabla}T) = 0. \end{aligned}\right\} \tag{17}$$

The value of the electric current was calculated through the integral over the cross-sectional area S_V:

$$I = \iint_{S_V} I_n dS_V, \tag{19}$$

where $I_n = n_x I_x + n_y I_y + n_z I_z$ is electric current density vector. The values I_x I_y I_z were determined by the relations:

$$I_x = -\sigma\frac{\partial U}{\partial x} - \sigma\alpha\frac{\partial T}{\partial x}, \tag{20}$$

$$I_y = -\sigma\frac{\partial U}{\partial y} - \sigma\alpha\frac{\partial T}{\partial y}, \tag{21}$$

$$I_z = -\sigma\frac{\partial U}{\partial z} - \sigma\alpha\frac{\partial T}{\partial z}. \tag{22}$$

The heat carrier flow rate was determined by integrating the velocity υ over the cross-sectional area of the channel S_{V1}:

$$G = \iint_{S_{V1}} \vartheta dS_{V1} \tag{23}$$

The electrical power of the thermoelement $W = I \cdot U$, heat flux coming to thermoelement $Q_h = GC_p \Delta t$.

The main parameter characterizing the efficiency of thermoelement work in the mode of electric energy generation is the efficiency which is determined by the relation:

$$\eta = \frac{W}{Q_h}. \tag{24}$$

Results of computer research on the characteristics of air permeable thermoelement made of materials based on *Bi-Te-Se -Sb*

The calculation was carried out for materials based on *Bi-Te-Se-Sb*. Functional dependences of the material parameters – the Seebeck coefficient α, thermal conductivity κ and electric conductivity σ on temperature were determined [3].

The simulation of a permeable thermoelement was made in the Comsol Multiphysics program for the following basic design (Fig. 1): height $b = 2$ *mm*, length 2 *mm*, width $a = 0.5$ *mm*. The dimensions of the lower interconnect – height $c = 0.1$ *mm*, length 2 *mm*, width $a = 0.5$ *mm*; upper – height $d = 0.1$ *mm*, length $c = 2$ *mm*, width 2 *mm*. The interconnect material is copper. These slots in the interconnect, together with the legs, form a system of channels for pumping the heat carrier. The contact resistance was $2 \cdot 10^{-6}$ Ohm·cm^2. Fig. 2 shows the partition of such a construction into finite elements.

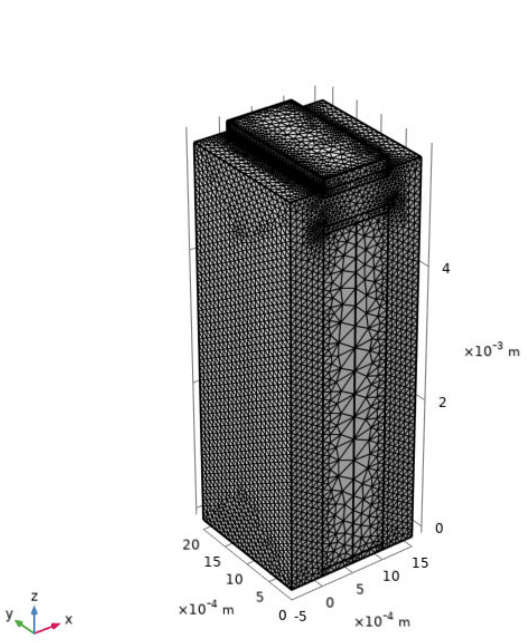

Fig. 2. Geometric grid.

An example of temperature distribution in heat carrier and thermoelement material at inlet gas temperature 600K is shown in Fig. 3.

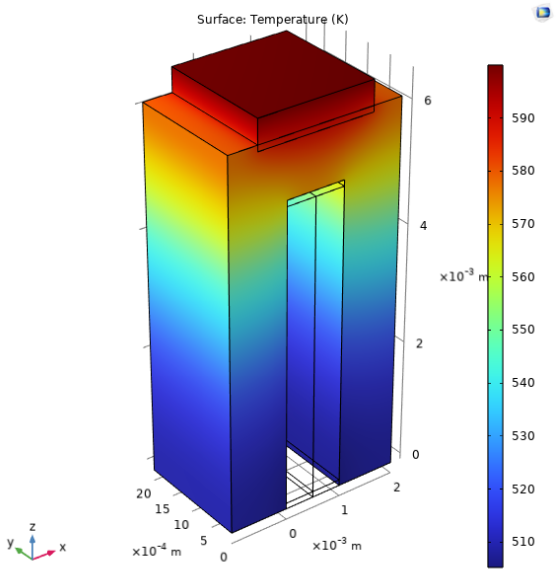

a) temperature distribution in heat carrier;

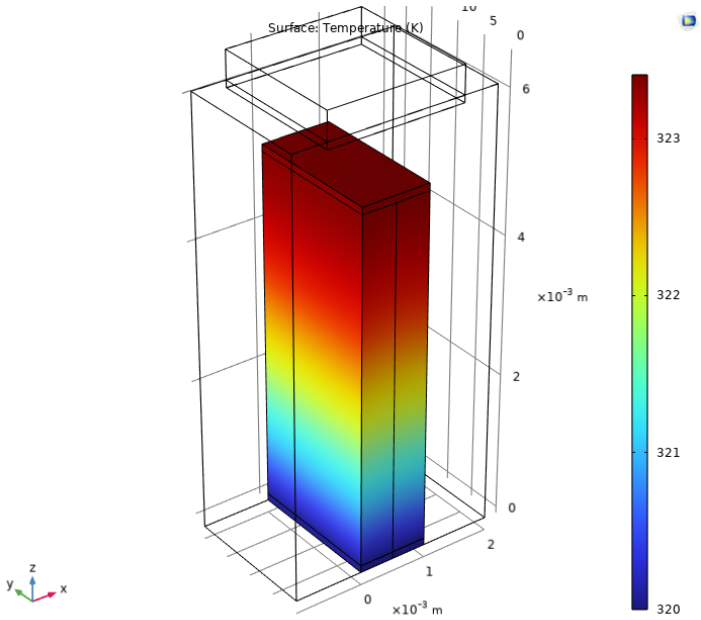

b) temperature distribution in thermoelement material.

Fig. 3. Temperature distributions.

The width of thermoelement legs varied from 0.05 mm to 0.2 mm, and heat carrier velocity at the inlet to thermoelement varied from 0.001m/s to 0.05 m/s.The heat exchange coefficient - α_T, according to Newton-Richmann law, was 1000 $W/(m^2 \cdot K)$.

For the above parameters, the average integral characteristics of thermoelement were determined: air temperature at the thermoelement outlet - t_{out}; thermoelement electromotive force - EMF; the value of the electric current I, A; air consumption - G; electric power W; efficiency η. The dependences of these

parameters on leg width a and height 0.002m for different heat carrier velocities V at the thermoelement inlet are presented in Table. The heat carrier temperature at the thermoelement inlet was 600K.

Table

Dependences of energy parameters on the width of leg and the velocity of heat carrier

a, m	V, m/s	$t_{вих}$, K	EPC, V	I, A	G, m^3/s	W, 10^{-8} W	η (%)
0.002	0.001	506.80	4.09E-04	1.25E-05	0.000855	0.50929	1.52
0.002	0.01	518.18	4.18E-04	1.32E-05	0.008724	0.551344	2.19
0.002	0.03	543.75	4.47E-04	1.49E-05	0.027447	0.665821	2.18
0.002	0.05	558.25	4.62E-04	1.59E-05	0.046937	0.732695	2.18
0.001	0.001	506.75	6.81E-04	6.71E-06	8.55E-04	4.57042	2.05
0.001	0.01	523.25	7.17E-04	7.31E-06	0.008823	5.24203	1.64
0.001	0.03	471.62	5.71E-04	4.14E-06	0.022122	2.3663	0.54
0.0005	0.001	474.75	0.001043	2.11E-06	7.75E-04	2.19625	0.11
0.0001	0.001	511.87	0.005279	9.16E-08	8.67E-04	4.83785	0.177

As can be seen from the table, for a leg width of 0.002 m, the value of efficiency from the rate of heat carrier supply to the thermoelement reaches saturation with a small maximum at a rate of 0.01 m/s. With a decrease in the thickness of legs (0.001 m), we obtain lower efficiency values at the same heat carrier velocities. Therefore, to identify maximum efficiency, it is necessary to carry out multi-parameter optimization of a permeable thermoelement. It is difficult to solve such a problem using the Comsol Multiphysics software package by parameter selection, since for modern computers with a clock frequency of 4.7 GHz, the program searches for a solution to a program with one set of

parameters for 8 hours. Therefore, to solve a multi-parameter optimization problem, it is more expedient to use the mathematical theory of optimal control developed for a 1D model of a permeable thermoelement.

Conclusions

1. A 3D model of a permeable generator thermoelement was developed in the Comsol Multiphysics software package.
2. The temperature distributions in the material of thermoelement legs and heat carrier, potentials in the thermoelement, air velocities and energy characteristics of a permeable generator thermoelement made of materials based on *Bi-Te-Se-Sb* were determined.
3. For multi-parameter optimization of structural and thermophysical parameters of a permeable thermoelement, it is advisable to use the mathematical theory of optimal control developed for a 1D model of a permeable thermoelement.

References

1. Anatychuk L. I. (1979). *Termoelementy i termoelektricheskiie ustroistva. Spravochnik. [Thermoelements and thermoelectric devices. Reference book]*. Kyiv [in Russian].
2. Anatychuk L. I. (2008). Termoelektrichestvo. T.1. Fizika termoelektrichestva [Thermoelectricity. Vol.1. Physics of Thermoelectricity]. Chernivtsi [in Russian].
3. Snyder G. J., Toberer E. S. (2008). Complex thermoelectric materials. *Nature Materials*, 7, 105 - 114.
4. Anatychuk L. I. (2007). Current status and some prospects of thermoelectricity. *J.Thermoelectricity*, 2, 7 - 20.
5. Anatychuk L. I., Vikhor L. N., Cherkez R. G. (2000). Optimal control of semiconductor material inhomogeneity for permeable cooling thermocouples. *J.Thermoelectricity*, 3, 45 - 55.
6. Anatychuk L. I., Cherkez R. G., Demyanyuk D.D., Bukharayeva N. R. (2012). Research on the energy characteristics of a permeable planar thermoelement. *J.Thermoelectricity*, 2, 88 - 92.
7. Anatychuk L. I., Semeniuk V. A. (1992). *Optimalnoiie upravleniie svoistvami termoelektricheskikh materialov i priborov [Optimal control over the properties of thermoelectric materials and devices]*. Chernivtsi: Prut [in Russian].
8. Kadenko I. M., Kharitonov O. M., Yermolenko R. V. [2010]. Osnovy teplohidravliky yadernykh energetychnykh ustanovok [Fundamentals of thermal hydraulics of nuclear power plants]. Kyiv: VPC “Kyiv University” [in Ukrainian].
9. Okhrimenko D. I. (2009). The use of COMSOL Multiphysics 3.4 package for solving hydrodynamics and heat exchange problems in chemical technology: Course paper. D.
10. Biriulin G. V. (2006). Thermophysical calculations in the COMSOL/FEMLAB finite element package: A Guidebook. St-Petersburg: ITMO University [in Russian].
11. http://www.comsol.com.

Submitted 09.03.2022

Анатичук Л. І., *акад. НАН України*[1,2]
Черкез Р. Г., *док. фіз.-мат. наук, в.о. професора*[1,2]
Порубаний О. М.[2]
Жукова А. С.[2]

[1]Чернівецький національний університет
імені Юрія Федьковича, вул. Коцюбинського 2,
Чернівці, 58012, Україна
[2]Чернівецький національний університет імені Ю. Федьковича,
Чернівці, Україна

ВПЛИВ ТОВЩИНИ ВІТКИ ТА ШВИДКОСТІ ТЕПЛОНОСІЯ НА ЕФЕКТИВНІСТЬ ПРОНИКНОГО ГЕНЕРАТОРНОГО ТЕРМОЕЛЕМЕНТА

В роботі представлені результати комп'ютерних досліджень по впливу товщини вітки та швидкості прокачки газу для 3D моделі проникного генераторного термоелемента на ЕРС та ККД. Розраховано залежності енергетичних характеристик термоелемента з матеріалів на основі Bi-Te-Se-Sb. Бібл. 11, рис.3, табл. 1.

Ключові слова: проникний термоелемент, комп'ютерне моделювання, генерація електричної енергії, енергетичні характеристики.

References

1. Anatychuk L. I. (1979). *Termoelementy i termoelektricheskiie ustroistva. Spravochnik. [Thermoelements and thermoelectric devices. Reference book]*. Kyiv [in Russian].
2. Anatychuk L. I. (2008). Termoelektrichestvo. T.1. Fizika termoelektrichestva [Thermoelectricity. Vol.1. Physics of Thermoelectricity]. Chernivtsi [in Russian].
3. Snyder G. J., Toberer E. S. (2008). Complex thermoelectric materials. *Nature Materials*, 7, 105 - 114.
4. Anatychuk L. I. (2007). Current status and some prospects of thermoelectricity. *J.Thermoelectricity*, 2, 7 - 20.
5. Anatychuk L. I., Vikhor L. N., Cherkez R. G. (2000). Optimal control of semiconductor material inhomogeneity for permeable cooling thermocouples. *J.Thermoelectricity*, 3, 45 - 55.
6. Anatychuk L. I., Cherkez R. G., Demyanyuk D.D., Bukharayeva N. R. (2012). Research on the energy characteristics of a permeable planar thermoelement. *J.Thermoelectricity*, 2, 88 - 92.
7. Anatychuk L. I., Semeniuk V. A. (1992). *Optimalnoiie upravleniie svoistvami termoelektricheskikh materialov i priborov [Optimal control over the properties of thermoelectric materials and devices]*. Chernivtsi: Prut [in Russian].
8. Kadenko I. M., Kharitonov O. M., Yermolenko R. V. [2010]. Osnovy teplohidravliky yadernykh energetychnykh ustanovok [Fundamentals of thermal hydraulics of nuclear power plants]. Kyiv:

VPC “Kyiv University” [in Ukrainian].

9. Okhrimenko D. I. (2009). The use of COMSOL Multiphysics 3.4 package for solving hydrodynamics and heat exchange problems in chemical technology: Course paper. D.
10. Biriulin G. V. (2006). Thermophysical calculations in the COMSOL/FEMLAB finite element package: A Guidebook. St-Petersburg: ITMO University [in Russian].
11. http://www.comsol.com.

Submitted 09.03.2022

DOI: 10.63527/1607-8829-2022-1-55-63

M. F. Dmytrychenko, *doc. techn sciences*
Yu. F. Gutarevych, *doc. techn sciences*
D. M. Trifonov, *cand. tehn. of science*
O. V. Syrota, *cand. tehn. of science*
E. V. Shuba, *cand. tehn. of science*
N. O. Kukhtyk, *doc. philosophy*

National Transport University 1, M.Omelianovycha-Pavlenka Str.,
Kyiv, 01010, Ukraine, *e-mail*: d.trifonov@ntu.edu.ua

USE OF A THERMOELECTRIC DEVICE TO MAINTAIN OPTIMAL AIR TEMPERATURE AT THE INTAKE OF A SPARK-IGNITION ENGINE WHEN OPERATING ON ALCOHOL-CONTAINING GASOLINE

The article deals with the problem associated with increasing the efficiency of operation of a spark ignition engine. Among the alternative fuels for spark ignition engines, ethanol is regarded worldwide as an important renewable energy source Adding ethanol to commercial gasoline reduces harmful air pollutants, greenhouse gases, and production costs. On the other hand, the use of benzoethanol mixtures as a fuel is associated with a lower saturated vapor pressure, which makes starting a cold engine quite difficult, and also leads to deterioration in the fuel-economic and environmental performance of the engine in the warm-up mode. A device with the use of thermoelectric modules is proposed for maintaining the optimal air temperature at the intake of a spark-ignition engine when operating on benzoethanol mixtures in the start-up and warm-up modes of a cold engine. The description of the proposed thermoelectric device, the principle of its functioning and the results of functional tests are presented. Bibl. 9, Fig 4.

Key words: spark ignition engine, benzoethanol mixture, thermoelectric modules, cold engine start and warm-up, intake air heating.

Introduction

Transport has become an integral part of modern life and one of the key sectors in terms of energy consumption. The internal combustion engine (ICE) running on fossil fuel is one of the most efficient and universal sources of mechanical energy used in cars, construction and agricultural machinery, stationary power plants, etc. The instability of world prices for fossil fuels, the reduction of its reserves, problems with transportation force us to look for alternative fuels. The use of alternative fuels should reduce the environmental damage associated with the use of fossil fuels. The development of the alternative fuel market should reduce Ukraine's dependence on oil and contribute to economic growth and reduction of greenhouse gas emissions in transport. Reducing the impact of road transport on atmospheric air pollution is one of the most important priorities of state policy in the field of road transport [1].

Therefore, research on the impact of alternative fuels on the environmental and energy performance of a vehicle engine, as well as determining recommendations for their use, taking into account the operating conditions of the vehicle, is an important scientific task that makes it possible to widely use alternative fuels in the future.

Analysis of previous research

Modern trends in the fuel industry, such as increased environmental requirements for fuel, an increase in the consumption of high-octane gasoline, an increase in the cost of oil production, a deterioration in the quality of produced oil and, as a result, an increase in the cost of its processing, lead to the need to revise traditional approaches to the production of motor fuels. First of all, this concerns the production of high-octane gasolines and the use of fuels and their components alternative to petroleum ones.

One of the ways to solve these problems can be the use of alcohol as an additive to traditional commercial gasoline, and first of all, dehydrated ethyl alcohol (fuel bioethanol) made of biologically renewable raw materials. The use of alcohol-containing gasoline mixtures has become a global trend that allows improving the energy efficiency of internal combustion engines, increasing its operational life, reducing maintenance costs, and most importantly, reducing dependence on fossil fuels [2 – 5].

Along with this, a number of significant drawbacks of the use of alcohol as a motor fuel have been identified, limiting its maximum concentration in benzoethanol mixtures. Thus, the high latent heat of evaporation makes it difficult to start a cold engine (at temperatures below 10°C it becomes practically impossible), the lower heat of combustion compared to the heat of combustion of petroleum fuels requires an increase in consumption by 25...30 %, the lower temperature of the exhaust gases leads to an increase in the time for the catalytic converter to reach an effective mode of conversion of harmful substances in the engine warm-up mode, as a result of which the emission of harmful substances increases, relatively high electrical conductivity in combination with a high oxygen content requires protection of parts of the fuel supply system from corrosion, phase instability of alcohol-containing fuel, unsatisfactory tribological characteristics [6, 7].

To overcome some of the disadvantages of using a benzoethanol mixture as a motor fuel, which will improve the performance of internal combustion engines, there are basically two possible approaches. The first is the introduction of a minimum amount of alcohol into commercial gasoline (up to 20 % in order to avoid problems with the normal operation of the internal combustion engine). The second is to ensure the heating of the intake air to the optimum temperature and stabilization when using a benzoethanol mixture (depending on the concentration of alcohol in the mixture) at low ambient temperatures, in particular, in cold engine start and warm-up modes.

Modern designs of vehicle engine intake systems, through the use of various design solutions, primarily provide a low concentration of harmful substances in the exhaust gas and high economic performance under normal operating conditions, in which there are no factors that impede the implementation of functional or technological processes. As is known, the operational characteristics of a vehicle engine in different modes of its operation depend not only on the improvement of the

design of engine systems, but also on operating conditions. Natural and climatic conditions have the greatest influence on the performance of the vehicle engine. The main characteristic of natural and climatic conditions, which significantly affects the operational properties of the vehicle, is the ambient temperature. The ambient air temperature is a determining factor in the formation of the air-fuel mixture due to the effect on the temperature in the intake manifold of the vehicle engine [8, 9].

The formation of the optimal composition of the air-fuel mixture, the speed and completeness of its combustion during engine operation in various modes, including at low ambient temperatures, to a large extent depends on the physicochemical properties of the fuel used, determined by a number of indicators, including saturated vapor pressure (SVP) characterizing the volatility of the fuel. The value of SVP can be used to judge the starting properties of the fuel (Fig. 1).

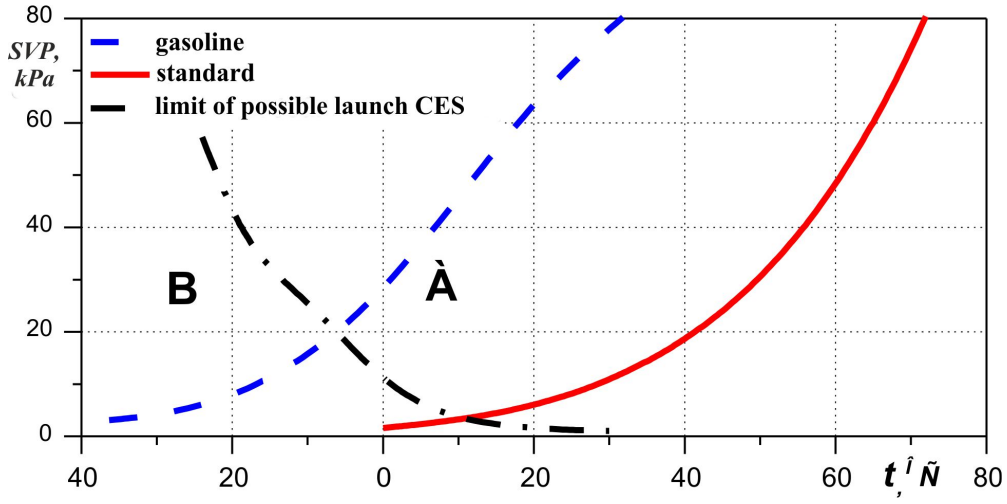

Fig. 1. Dependence of the SVP of gasoline and alcohol on the ambient air temperature and the dependence of possible engine start on their SVP: A – the area where it is possible to start an internal combustion engine; B – area where start-up is impossible

Presented in Fig. 1, graphical dependences obtained from a fairly large number of sources show that with an increase in the ethanol content in the benzoethanol blend, the SVP decreases and reaches a value that makes it impossible to start the engine, especially at low temperatures.

Various methods are used to intensify fuel evaporation at low temperatures, including fuel preheating, intake manifold heating, intake air heating, increased airflow turbulence, and others.

In this regard, the use of a benzoethanol blend, especially with fairly high ethanol content, requires the development of various methods and devices in order to ensure the preparation of an air-fuel mixture of optimal composition and quantity, regardless of climatic conditions and vehicle engine operating modes.

The results of the conducted analysis indicate the relevance and expediency of research aimed at creation and use of devices that ensure the improvement of the operating characteristics of a spark-ignition engine when working on benzoethanol mixtures in the start-up and warm-up modes of a cold engine.

Research results

Taking into account the requirements for minimizing interference in the engine design, systems that ensure its operation and modern technological solutions, the authors proposed a system that ensures automatic maintenance of the optimal air temperature in the intake manifold of the vehicle engine, which consists of an internal combustion engine, an air cleaner, an intake manifold, a thermoelectric device (TED), electronic control unit, air temperature sensor in the intake manifold, load sensor. The thermoelectric device consists of thermoelectric modules, an internal and external heat sink with fans, and an external heat sink temperature sensor (Fig. 2).

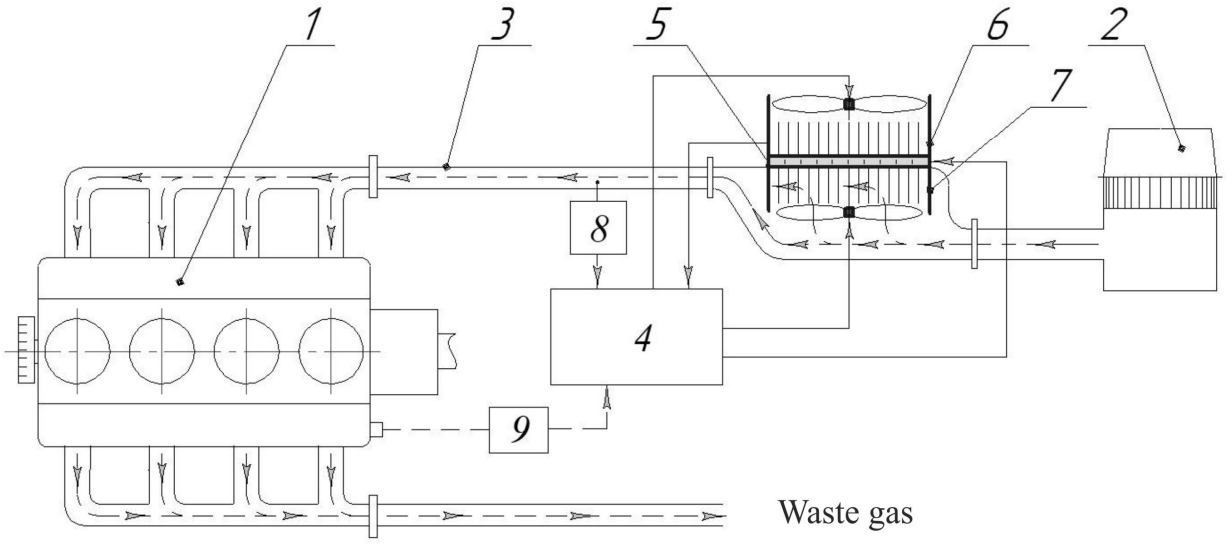

Fig. 2. Structural schematic of the proposed system, which ensures automatic maintenance of the optimal air temperature in the intake manifold of the internal combustion engine: 1 – iternal combustion engine, 2 – air cleaner, 3 – intake manifold, 4 – electronic control unit, 5 – thermoelectric module, 6 – external heat sink with a fan and temperature sensor, 7 – internal heat sink with a fan, 8 – air temperature sensor in the intake manifold, 9 – load sensor

The main element of the proposed system is a thermoelectric device consisting of thermoelectric modules, the principle of operation of which is based on the Peltier effect (TEC1-12706). The most significant features of thermoelectric modules are: small weight and dimensions, lack of moving parts, fairly high heating speed with low energy consumption, practically no need in maintenance. The use of thermoelectric modules often allows obtaining a simple solution to complex technical problems of thermal energy management and provides significant advantages over alternative technologies.

Functions of the electronic control unit: forms a continuous current and voltage on the thermoelectric modules, measures and stabilizes the intake air temperature, limits the power consumed according to the set value, controls the temperature of the external heat sink of the thermoelectric device and controls its fan, smoothes out pulsations and performs diagnostics of the parts of the proposed system.

A fan is used to intensify the heat exchange (enhance turbulence) of the air flow in the intake manifold with the internal heat sink of the thermoelectric modules. In order to prevent a decrease in the efficiency of the proposed system, the electronic control unit ensures that the fan of the external heat sink is turned on according to the signal level of the external heat sink temperature sensor.

The principle of operation of the proposed thermoelectric system is as follows: during engine operation, the electronic control unit receives signals from air temperature sensors in the intake manifold, the external heat sink, and the load. Depending on the level of these signals, the electronic control unit, by changing the power of the electric current supplied to the thermoelectric modules, ensures the required (optimal) temperature of the internal heat sink (the degree of its heating).

The proposed system provides the following modes of operation:

- under conditions of optimal air temperature in the intake manifold (according to the signal level of the air temperature sensor in the intake manifold), air from the air cleaner through the intake manifold enters the engine cylinders (the thermoelectric device is turned off);
- under conditions when the air temperature in the intake manifold is less than optimal, the electronic control unit connects the thermoelectric modules to the on-board network, which ensures an increase in the temperature of the internal heat sink and, by changing the power of the electric current, ensures the heating of the air in the intake manifold to optimal values.

At the Department of Engines and Thermal Engineering of the National Transport University, a working sample of the proposed thermoelectric device was made (Fig. 3) and its functional tests were carried out in order to assess the possible effectiveness of the proposed device for maintaining the optimum air temperature at the intake of a spark ignition engine when operating on benzoethanol mixtures under conditions of low ambient temperatures.

Functional tests of the working sample were carried out at an ambient air temperature of minus 5°C. At the same time, the temperature change at the outlet of the thermoelectric device, the voltage and the current strength at the thermoelectric module were monitored. Based on the analysis of the literature, which is devoted to the features of starting a cold engine, the optimal intake temperature in the start-up and warm-up modes is about +40...60 °C. Taking into account the higher heat capacity of benzoethanol mixtures compared to commercial gasoline, the final intake temperature was chosen to be about + 60 °C.

According to the results of the research, the following was established. The average value of the voltage on the thermoelectric module was 12.7 V, the current strength was 4.1 A. Air temperature after 3 min reached 56.8 °C, while there was a decrease in the rate of increase in air temperature (Fig. 4). This phenomenon is due to a decrease in current power, which is explained by the absence during the research of TED electronic control unit, in particular, managing controller of thermoelectric module. This phenomenon is due to a decrease in the current power, which is explained by the absence of an electronic control unit during the TEC study, in particular, the managing controller of the thermoelectric module. The absence of a thermoelectric module controller led to a decrease in current power by almost 12 % compared to the initial value.

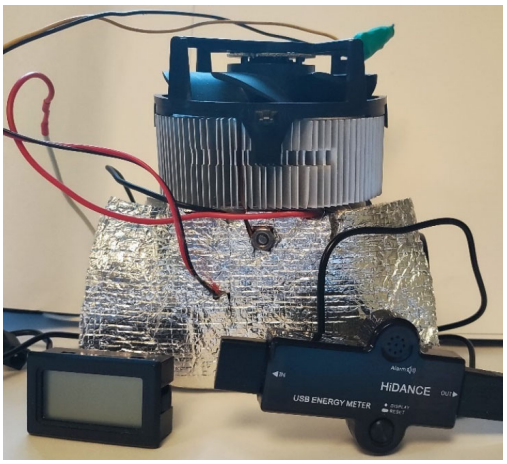

a)

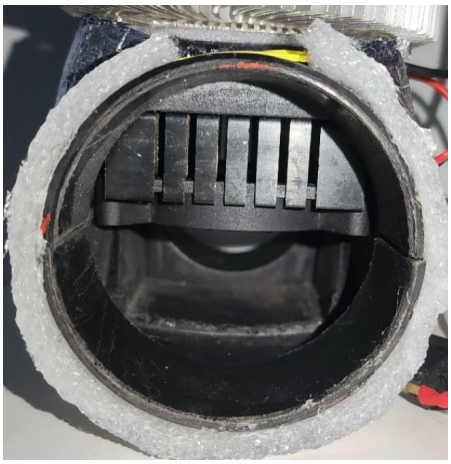

b)

Fig 3. Experimental sample of the proposed thermoelectric device: a) General view of a TED with a remote temperature sensor and a voltage, currentand power consumption tester, b) Internal heat sink with a fan

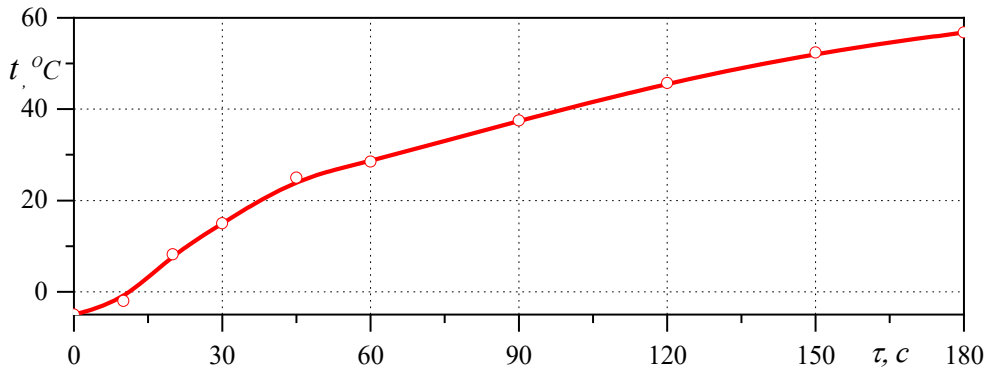

Fig.4. Change in intake air temperature when using TED

Based on the results of functional tests, the possibility and expediency of using devices that ensure the maintenance of the optimum air intake temperature of spark ignition engine in the modes of starting and warming up a cold engine when operating on benzoethanol mixtures, in particular, thermoelectric modules, the principle of operation of which is based on the Peltier effect, have been confirmed. Based on the results of the study, it was established that it is necessary to use a managing controller for a thermoelectric module, the absence of which leads to a sharp decrease in the efficiency of the module (according to some data, up to 30 ... 40 %).

Conclusions

1. Alternative fuels, in particular benzoethanol mixtures, have great potential in solving fuel-energy and environmental problems associated with fossil fuels.
2. The possibility of using thermoelectric devices to maintain the optimal air temperature at the intake of the vehicle engine during operation on benzoethanol mixtures, in particular in the start-up and warm-up modes of a cold engine, was studied.
3. The advantages and prospective directions of the use of thermoelectric devices during the operation of vehicle engines under conditions of low ambient air temperatures are determined. It has been established that such devices can realize the heating of the intake air to optimal values.
4. Functional tests of TED indicate the possibility and expediency of using thermoelectric modules, the principle of operation of which is based on the Peltier effect with a managing controller to maintain the optimal air temperature at the intake of a spark-ignition engine in the start-up and warm-up modes during its operation on benzoethanol mixtures.

References

1. The Law of Ukraine on the basic principles (strategy) of the state environmental policy of Ukraine for the period up to 2030. Verkhovna Rada Vidomosti, 2019, 16, p.70.
2. Erdiwansyah Mamat, R., Sani M. S. M., Sudhakar K., Kadarohman A., and Sardjono R. E. (2019). An overview of higher alcohol and biodiesel as alternative fuels in engines. *Energy Reports*, 5, 467-479, ISSN 2352-4847, https://doi.org/10.1016/j.egyr.2019.04.009
3. Awad O. I., Mamat R., Ali O. M., Sidik N. A. C., Yusaf T., Kadirgama K., Kettner M. Alcohol and ether as alternative fuels in spark ignition engine: A review. (2018). *Renewable and Sustainable Energy Reviews,* 82, Part 3, 2586-2605, ISSN 1364-0321, https://doi.org/10.1016/j.rser.2017.09.074.
4. Tibaquirá J. E., Huertas J. I., Ospina S., Quirama L. F., Niño J. E. (2018). The effect of using ethanol-gasoline blends on the mechanical, energy and environmental performance of in-use vehicles. *Energies* 11, 221. https://doi.org/10.3390/en11010221.
5. Sivakumar Kasibhatta (2019). *Alcohol fuels as an alternative fuel - bringing new heights in sustainability, alcohol fuels - current technologies and future prospect*, Yongseung Yun, IntechOpen, (November 5th 2019). DOI: 10.5772/intechopen.86626.

6. Matějovský L., Macák J., Pospíšil M., Staš M., Baroš P., & Krausová A. (2018). Study of corrosion effects of oxidized ethanol–gasoline blends on metallic materials. *Energy & Fuels*, 32 Part 4, 5145 - 5156, https://doi.org/10.1021/acs.energyfuels.7b04034.
7. Raja A., Arasu A. (2015). Exhaust gas treatment for reducing cold start emissions of a motorcycle engine fuelled with gasoline-ethanol blends. *Journal of Energy in Southern Africa*. 26, Part 2, 84 - 93. ISSN 2413-3051, http://doi.org/10.17159/2413-3051/2015/v26i2a2199.
8. Monteiro Sales Luis Carlos, Sodré José Ricardo (2012). Cold start characteristics of an ethanol-fuelled engine with heated intake air and fuel. *Applied Thermal Engineering*, 40, 198-201, ISSN 1359-4311, https://doi.org/10.1016/j.applthermaleng.2012.01.057.
9. Dmytrychenko M. F., Gutarevych Y. F., Trifonov D. M., Syrota O. V. (2020). The use of thermoelectric energy converters to reduce the influence of natural and climatic factors on the technical readiness of a vehicle. *J.Thermoelectricity*, 3, 56 - 68.

Submitted 23.02.2022

Дмитриченко М. Ф. *доктор техн. наук*
Гутаревич Ю. Ф. *доктор техн. наук*
Тріфонов Д. М. *канд. техн. наук*
Сирота О. В. *канд. техн. наук*
Шуба Е. В. *канд. техн. наук*
Кухтик Н. О. *доктор філософії*

Національний транспортний університет
вул. М. Омеляновича-Павленка, 1, м. Київ,
01010, Україна, *e-mail: d.trifonov@ntu.edu.ua*

ВИКОРИСТАННЯ ТЕРМОЕЛЕКТРИЧНОГО ПРИСТРОЮ ДЛЯ ПІДТРИМАННЯ ОПТИМАЛЬНОЇ ТЕМПЕРАТУРИ ПОВІТРЯ НА ВПУСКУ ДВИГУНА З ІСКРОВИМ ЗАПАЛЮВАННЯМ ЗА РОБОТИ НА СПИРТОВМІСНОМУ БЕНЗИНІ

У статті розглядається проблема, що пов'язана з підвищенням ефективності експлуатації двигуна з іскровим запалюванням. Серед альтернативних палив, для двигунів з іскровим запалюванням у всьому світі розглядається етанол як важливе відновлюване джерело енергії. Додавання етанолу до товарного бензину забезпечує зниження шкідливих забруднювачів повітря, парникових газів, а також цін на виробництво. З іншого боку, використання бензоетанольних сумішей як палива пов'язано з більш низьким тиском

насичених парів, що робить пуск холодного двигуна досить складним, а також призводить до погіршення паливно-економічних і екологічних показників двигуна в режимі прогріву. Запропоновано пристрій що використовує термоелектричні модулі для підтримання оптимальної температури повітря на впуску двигуна з іскровим запалюванням при роботі на бензоетанольних сумішах в режимах пуску і прогріву холодного двигуна. Наведено опис запропонованого термоелектричного пристрою, принцип його функціонування та результати функціональних випробувань. Бібл. 9, рис. 4.

Ключові слова: двигун з іскровим запалюванням, бензоетанольна суміш, термоелектричні модулі, пуск і прогрів холодного двигуна, підігрів повітря на впуску.

References

1. The Law of Ukraine on the basic principles (strategy) of the state environmental policy of Ukraine for the period up to 2030. Verkhovna Rada Vidomosti, 2019, 16, p.70.
2. Erdiwansyah Mamat, R., Sani M. S. M., Sudhakar K., Kadarohman A., and Sardjono R. E. (2019). An overview of higher alcohol and biodiesel as alternative fuels in engines. *Energy Reports*, 5, 467-479, ISSN 2352-4847, https://doi.org/10.1016/j.egyr.2019.04.009
3. Awad O. I., Mamat R., Ali O. M., Sidik N. A. C., Yusaf T., Kadirgama K., Kettner M. Alcohol and ether as alternative fuels in spark ignition engine: A review. (2018). *Renewable and Sustainable Energy Reviews,* 82, Part 3, 2586-2605, ISSN 1364-0321, https://doi.org/10.1016/j.rser.2017.09.074.
4. Tibaquirá J. E., Huertas J. I., Ospina S., Quirama L. F., Niño J. E. (2018). The effect of using ethanol-gasoline blends on the mechanical, energy and environmental performance of in-use vehicles. *Energies* 11, 221. https://doi.org/10.3390/en11010221.
5. Sivakumar Kasibhatta (2019). *Alcohol fuels as an alternative fuel - bringing new heights in sustainability, alcohol fuels - current technologies and future prospect*, Yongseung Yun, IntechOpen, (November 5th 2019). DOI: 10.5772/intechopen.86626.
6. Matějovský L., Macák J., Pospíšil M., Staš M., Baroš P., & Krausová A. (2018). Study of corrosion effects of oxidized ethanol–gasoline blends on metallic materials. *Energy & Fuels*, 32 Part 4, 5145 - 5156, https://doi.org/10.1021/acs.energyfuels.7b04034.
7. Raja A., Arasu A. (2015). Exhaust gas treatment for reducing cold start emissions of a motorcycle engine fuelled with gasoline-ethanol blends. *Journal of Energy in Southern Africa*. 26, Part 2, 84 - 93. ISSN 2413-3051, http://doi.org/10.17159/2413-3051/2015/v26i2a2199.
8. Monteiro Sales Luis Carlos, Sodré José Ricardo (2012). Cold start characteristics of an ethanol-fuelled engine with heated intake air and fuel. *Applied Thermal Engineering*, 40, 198-201, ISSN 1359-4311, https://doi.org/10.1016/j.applthermaleng.2012.01.057.
9. Dmytrychenko M. F., Gutarevych Y. F., Trifonov D. M., Syrota O. V. (2020). The use of thermoelectric energy converters to reduce the influence of natural and climatic factors on the technical readiness of a vehicle. *J.Thermoelectricity*, 3, 56 - 68.

Submitted 23.02.2022

DOI: 10.63527/1607-8829-2022-1-64-81

V. G. Kolobrodov, *doc. techn. sciences, professor*
V. I. Mykytenko, *doc. techn. sciences, assist professor*
G. S. Tymchyk, *doc. techn. sciences, professor*
M. S. Kolobrodov

National Technical University of Ukraine
"Igor Sikorsky Kyiv Polytechnic Institute"
37 Peremohy Ave., Kyiv, 03056, Ukraine
e-mail: deanpb@kpi.ua

INCREASING THE SENSITIVITY OF COMPUTER-INTEGRATED THERMAL IMAGERS IN THE STUDY OF THERMOELECTRIC PHENOMENA AND REMOTE OBSERVATIONS

The work is devoted to the substantiation of the choice of optical polarizing elements for thermal imaging remote observations and measurements. A comparative analysis of the main methods of obtaining polarization images was performed, namely using polarizer rotation, phase plate rotation, and using combined infrared matrix receivers with micro polarizers. Simplified mathematical models of signal transformation in the main optical elements of polarimetric thermal imagers – linear polarizers and phase (quarter-wave) plates - were used for the analysis. The advantage of wire polarizers compared to polarizers based on reflection is shown. It is also substantiated that among the various physical effects causing phase delays – birefringence, total internal reflection and reflection of radiation at the air-metal interface, diffraction on a wire diffraction grating – the use of the latter effect is most acceptable. Bibl. 21, Figs. 7.

Key words: polarimetric thermal imagers, Stokes vectors, polarizer, quarter-wave plate.

Introduction

Thermoelectric phenomena are widely used in various spheres of human activity. One of the relevant scientific and applied problems, for instance, is the utilization of waste heat using thermoelectricity [1]. A complete set of means for technical implementation of energy conversion processes requires many components, including measurement technologies. To control the quality of thermoelectric energy converters, computerized methods of absolute measurements using thermocouples are being developed [2]. More generalized monitoring of physical phenomena related to thermal contrasts is possible using thermal imagers. Classical thermal imagers allow observing the thermal radiation contrast of energy brightness (intensity) between the object and the background [3]. With a low radiation contrast of the observation object, the efficiency of using classical thermal imagers may not be high. In order to increase the radiation contrast of images of objects on a uniform background, some countries have begun research on the creation of thermal imagers, in which the

carrier of information is the polarization properties of infrared (IR) radiation of the target and the background (obstacles) [4, 5, 6]. Such polarimetric thermal imagers (PT) measure the polarization characteristics of radiation from the object and background, namely: intensity, degree of polarization, and azimuth and ellipticity of polarization [7, 8]. These characteristics make it possible to measure the complex refractive index, which combines the optical and electrical parameters of the medium under study.

The PT optical system consists of an IR polarizer, a quarter-wave retarder, and an IR lens located in series on the optical axis [9, 10]. A number of monographs and articles [11, 12] are devoted to the study of such an optical system, where the polarization elements (IR polarizer and quarter-wave plate) are considered, which perform the appropriate transformations of the optical signal to obtain the polarization parameters of radiation from the observation object and the background. Also, great attention is paid to PT calibration [13]. At the same time, there is no information on the study of PT optical system in order to substantiate the choice of infrared polarizer and phase plate for improving the operational characteristics of the thermal imager.

The purpose of this work is to research and substantiate the choice of infrared polarizer and phase plate to match their parameters, which will improve the operational characteristics of polarimetric thermal imagers.

Physical and mathematical model of the optical-electronic system of the polarimetric thermal imager

The polarization characteristics of radiation, which change during propagation and reflection, can be expressed by the Stokes vector, the Jones vector, or the Mueller matrix [14, 15]. The Stokes vector was proposed to study partially polarized, as well as unpolarized and fully polarized light. The four parameters of the Stokes vector $\vec{S} = \{S_0, S_1, S_2, S_3\}$ describe information about the polarization state of the observation object. The four-segmentation method of the modulation of the matrix radiation receiver (MRR) by the polarization state of the radiation for the measurement of the Stokes vector has become the most widespread [4, 5, 9].

Fig. 1 shows a diagram that explains the operating principle of such a PT based on modulation [10]. To simplify the study, we will assume that monochromatic radiation is considered. The investigated partially polarized radiation with amplitude $\vec{E}_{pp}$ passes through a polarizer, a quarter-wave plate, which can change the polarization angle θ and the phase difference ε between the components E_x and E_y of the vector $\vec{E}_{pp}$ using mechanical rotation, or continuous periodic modulation. The infrared MRR forms a group of output radiation values, which are used to obtain four parameters of the Stokes vector of the polarization image by changing the angles θ and ε.

The Stokes vectors make it possible to obtain the main parameters of radiation polarization: intensity, degree of polarization, polarization angle, and polarization ellipticity.

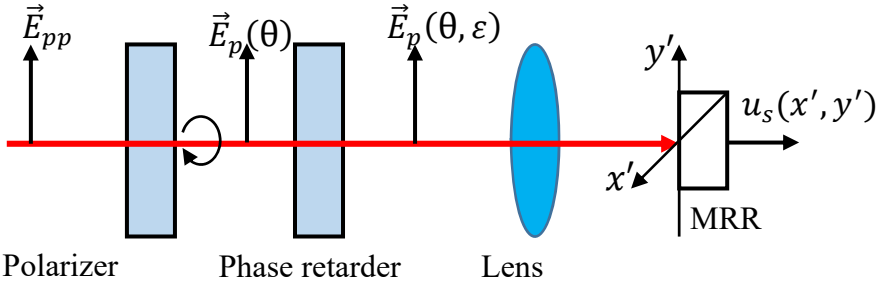

Fig. 1. Operating principle of polarimetric thermal imager

We will consider the PT optical system, which consists of an IR polarizer, a quarter-wave plate and an IR lens of a thermal imager located in series on the optical axis (Fig. 2). Let a parallel beam of natural or partially polarized radiation with amplitudes $\vec{E}_n$ or $\vec{E}_{pp}$, respectively, enter the input of the optical system. At the output of the polarizer, linearly polarized radiation with the vector $\vec{E}_{lp}$ is formed, which is oriented at an angle θ relative to the x axis. After passing through a quarter-wave plate, the optical axis of which is parallel to the surface of the plate and forms the angle α with the vector $\vec{E}_{lp}$ (polarization plane), as a result of birefringence in the plate, ordinary and extraordinary beams with amplitudes E_0 and E_e are formed. These beams spread in one direction and have a phase difference at the exit from the plate

$$\Delta\varphi = \varepsilon = k \cdot \Delta d = \frac{2\pi}{\lambda}(n_o - n_e)d, \qquad (1)$$

where d is the thickness of the plate, n_o and n_e are the refractive indices for the ordinary and extraordinary beams, respectively.

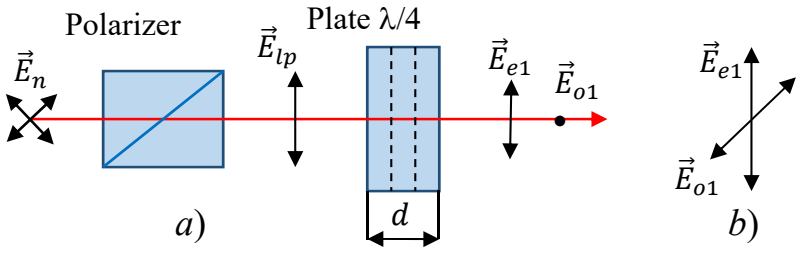

Fig. 2. Diagram for radiation polarization study (a) and its vector model (b)

In modern PTs, three methods of obtaining a polarized image are used: rotation of the polarizer, rotation of the phase plate, and the use of MRR, each pixel of which has a micro polarizer with a certain orientation of the polarization axis [16]. The first and second methods have limited use

due to the presence of a mechanical system for rotating optical elements and the need to use three or four consecutive frames. Fig. 3 shows different polarization states of optical radiation, which can be fully described by the four Stokes parameters.

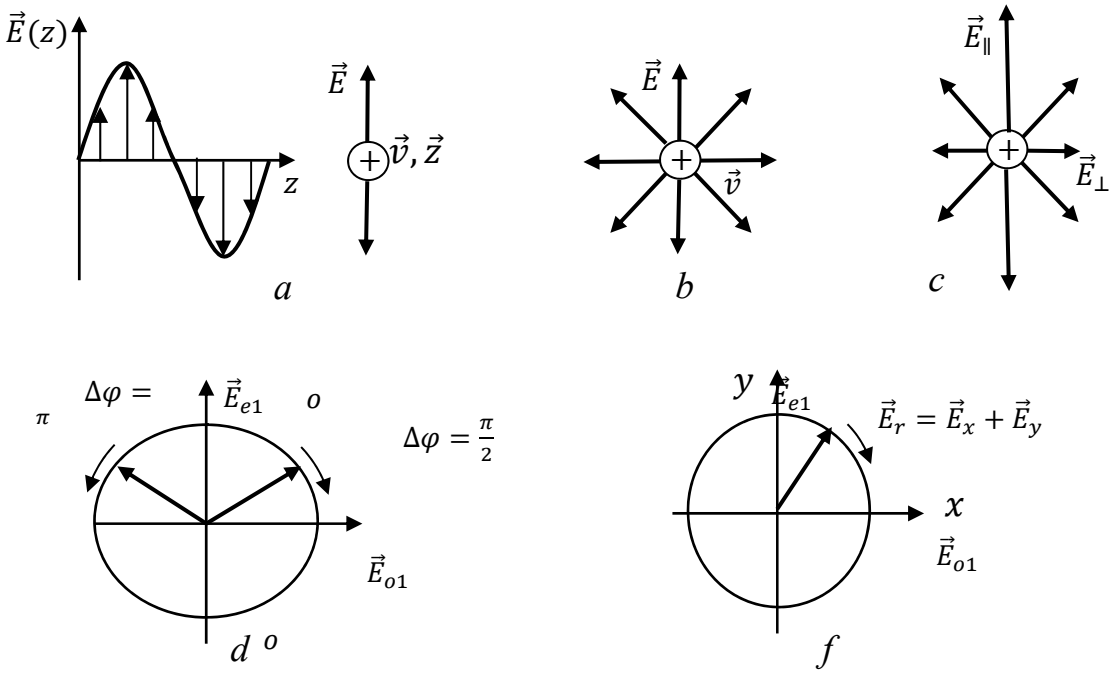

Fig. 3. State of radiation polarization: a – linearly polarized; b – natural; c – partially polarized; d – elliptically polarized; f – circularly polarized

The first Stokes parameter S_0 determines the total optical intensity. The second Stokes parameter S_1 determines the preference of the recorded optical signal for horizontal polarization over vertical polarization. The third Stokes parameter S_2 determines the preference of the recorded optical signal with linear polarization oriented along 45° over linear polarization along 135°, which are measured relative to the horizontal direction. The fourth Stokes parameter S_3 characterizes the superiority of right-circular polarization over left-circular polarization.

The Stokes parameters can be determined with the aid of two orthogonal electric radiation fields E_x and E_y, which are defined by the equations

$$E_x(t) = E_{x0}\exp[j(2\pi\nu t - \varphi_x)] \text{ i } E_y(t) = E_{y0}\exp\big[j(2\pi\nu t - \varphi_y)\big], \qquad (2)$$

where E_{x0} , E_{y0} and φ_x , φ_y are constant amplitudes and initial phases of these fields, respectively; ν is radiation frequency. The electric radiation field that passed through a linear polarizer with the

polarization axis in the θ direction and a phase plate with a delay by the angle $\varepsilon = \varphi_x - \varphi_y$, is determined by equation (3):

$$E_1(\theta, \varepsilon) = E_x \cos\theta + E_y \exp(j\varepsilon)\sin\theta. \quad (3)$$

Let us consider the features of using polarizers and phase plates in PT optical systems.

Polarizers for the IR region of the spectrum

A polarizing optical element is any optical element that changes the state of radiation polarization [15]. Polarizers and phase plates (phase retarders) are polarizing optical elements.

General provisions

A polarizer is an optical element designed to create light regardless of the properties of the incoming light. The desired state of polarized light can be linear, circular, or elliptically polarized (Fig. 3), and an optical element designed to create one of these states is called a linear, circular or elliptical polarizer. Polarizers use such optical phenomena as absorption, refraction, birefringence and diffraction of radiation.

The linear polarizer has two transmission parameters: the basic main transmittance T_1 and the secondary main transmittance T_2. The parameter T_1 is defined as the ratio of the intensity at the output of the polarizer $I_{p,max}$ to the intensity at the input I_0, when the incident beam is linearly polarized in the oscillation azimuth, which provides the maximum transmittance. Similarly, the parameter T_2 is determined for the minimum transmittance. Thus

$$T_1 = \frac{I_{p,max}}{I_0}; T_2 = \frac{I_{p,min}}{I_{,0}}. \quad (4)$$

The ratio $R_t = T_1/T_2$ is called *the main transmittance (extinction coefficient)* of the polarizer. For high-quality polarizers, this coefficient can reach 10^5. The average value of the main transmittances is called the total transmittance

$$T_t = \frac{T_1+T_2}{2}. \quad (5)$$

The parameter T_t is defined as the ratio of the intensity at the output of the polarizer to the intensity of the input unpolarized beam.

For a perfect polarizer, Malus`s law has the form

$$I_{id}(\theta) = \frac{1}{2} I_0 \cos^2\theta. \quad (6)$$

For a real polarizer, Malus`s law is given by

$$I_r(\theta) = I_{90} + (I_0 - I_{90})\cos^2\theta. \quad (7)$$

Wire grid polarizers

In the IR region of the spectrum, polarizers in the form of a flat grid formed by parallel wires (wire grid polarizer, WGP) are widely used [15, 16]. Such a polarizer forms linearly polarized radiation in a plane perpendicular to the wires. The distance between the wires must be less than the wavelength. The wire grid is applied to the substrate, the surface of which has an anti-reflection coating. Radiation that is polarized parallel to the wires is reflected. The grating period of IR polarizers is usually 0.5 μm or more.

Since reflection and absorption losses reduce the transmittance of wire gratings, an anti-reflection coating is applied to the substrate. Therefore, its quality and achromacity are important factors in the production of wire gratings. Commercial wire grating polarizers have a basic transmittance (20 – 10000) for linear polarization of radiation in transmission mode in the spectral range from 1.5 μm to millimeter wavelengths.

Typical technical characteristics of wire polarizers are given in Table 1.

Table 1

Technical characteristics of a wire polarizer

Parameters at λ = 5 μm	Technical characteristics
Transmission efficiency, T_1, %	90
Transmission of unwanted radiation, T_2, %	0.4
Degree of polarization, $(T_1 - T_2)/(T_1 + T_2)$, %	99
Extinction ratio, T_1/T_2	225

In [17], an IR wire polarizer is considered, which consists of a grating with a period of 400 nm on a photocurable film 30 μm thick. The grating is made of gold using thermal spraying and film imprinting in high humidity conditions. The polarizer has a transverse magnetic transmission of more than 75% in the range of wavelengths (4 – 5.5) μm and an extinction ratio of more than 20 dB in the range (2.5 – 7.5) μm. The maximum extinction ratio is more than 28 dB for a wavelength of 6.5 μm. Such a film polarizer with high transmittance is cheaper compared to conventional IR polarizers.

In [16], the process of manufacturing a wire polarizer for pixels of a micro bolometric (MBM) MRR is described. A wire grid made of gold is applied to a substrate that has low losses for the wavelength of the incident wave, that is, the small imaginary and real parts of the refractive index *n*, k [18] should have minimum values. The ideal solution to this problem is the mechanical placement of a gold grid in the air, which is technologically impossible. Therefore, substrates with different refractive indices were used (Fig. 4).

Numerical simulation of the propagation of TM and TE fields for various wire grids (period, metal thickness, substrate materials and wavelengths) was carried out using the theory of diffraction gratings [19]. If the electric field vector is parallel to the boundary between two media, then we speak about the TE-polarization of the wave. If the magnetic field vector is parallel to the boundary between two media, then the radiation is considered to be TM-polarized. The purpose of this simulation is to find the geometric dimensions of the grating, when the extinction ratio of the TM/TE field at the polarizer output exceeds 100:1, the TM transmission value exceeds 80 %.

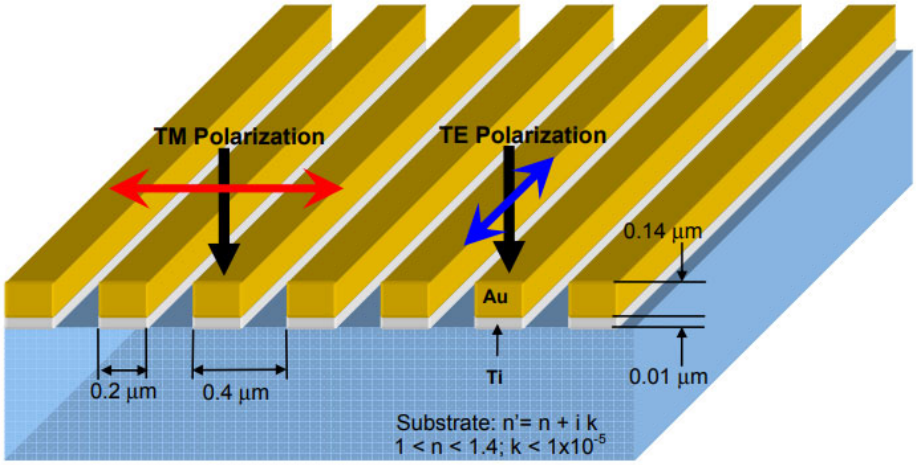

Fig. 4. Illustration of a gold wire grid polarizer on a substrate with a low refractive index for n and k and different geometric dimensions [15]

A simplified version of the PT optical system uses a rotating phase plate behind which a fixed linear polarizer is located, which allows obtaining several consecutive images to determine the Stokes parameters over the entire field of view. An alternative method is the field of view which is spatially divided into superpixels, in each of which the Stokes parameters are determined simultaneously. Each superpixel cell has a separate wire micro polarizer with a certain orientation of the polarization plane.

The key element of the PT optical system is a quarter-wave plate designed for the appropriate spatial division of the image. Various physical phenomena can be used in such plates: reflection at the Brewster`s angle, birefringence, diffraction of radiation on a wire grating with a small period. Such subwavelength gratings have an effective refractive index that depends on the polarization of the incoming radiation. This effect is known as birefringence and can be used to create a wave plate.

In [16], the results of a project at Sandia National Laboratories (Albuquerque, New Mexico, USA) to develop a long-wavelength infrared micro polarization device for polarimetric imaging are presented. Information about the polarization state of radiation from the object and the background can help detect and recognize objects of interest for various remote sensing tasks and for military applications. While traditional sequential polarimetric images create scenes with polarization information using a series of acquired images, the use of a MRR, each pixel of which has a polarizer with a certain orientation of the polarization plane, allows, through processing of pixel signals, to determine the distribution in the image plane of all four Stokes parameters simultaneously.

Fig. 5 shows the MRR superpixel model, which consists of four cells with separate micro polarizers with different orientations of the polarization plane. The orientation of the wires in each cell is different, which results in each cell forming a polarizer whose optical axis forms angles of 0°, 45°, 90° and 135° with the optical axis of the retarder. Thus, the use of a superpixel allows simultaneous reception of signals at the output of individual cells for different polarization angles in one frame. The processing of these signals makes it possible to calculate the components of the Stokes vector, which determines the polarization characteristics of the radiation of the observation object [16]:

$$S_0 = 1; S_1 = \{2I(0°,0) - [I(0°,0) + I(90°,0)]\}/[I(0°,0) + I(90°,0)];$$

$$S_2 = \{2I(45°,0) - [I(0°,0) + I(90°,0)]\}/[I(0°,0) + I(90°,0)];$$

$$S_3 = \{2I(135°,\pi/2) - [I(0°,0) + I(90°,0)]\}/[I(0°,0) + I(90°,0)].$$

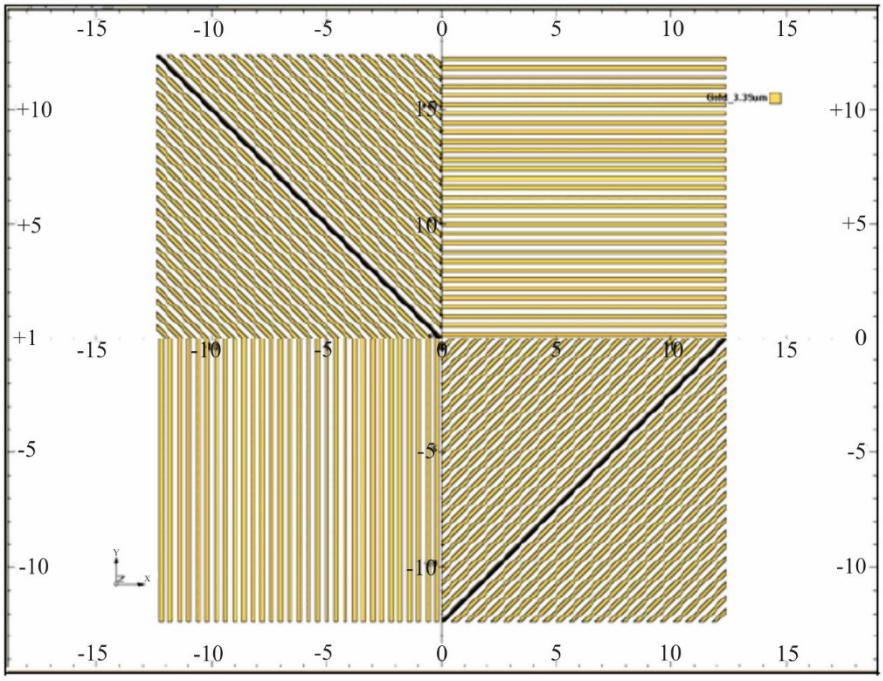

Fig. 5. Model of MBM superpixel model

Commercial IR polarizers are commercially available from some optical companies, such as Edmund & Tydex. Such polarizers are designed for linear polarization of radiation in the transmission mode in the spectral range from 1.5 μm to millimetre wavelengths. They are a type of diffraction grating and are cut into a crystalline or polymer substrate. The polarizer grating is a set of triangular profile strokes. An aluminium coating is applied to one of the faces of each stroke. Depending on the material of the substrate, polarizers are made using a diffraction grating technology.

The Edmund Optics company supplies the market with polarizers using a special holographic technique, owing to which the distance between the wires is micrometers [20]. Compared to conventional methods, the holographic method creates a finer groove spacing that optimizes

performance for short wavelengths. Holographic wire polarizers are created from barium fluoride (BaF_2), zinc selenide (*ZnSe*), thallium bromo-iodide (KRS-5) and germanium (*Ge*).

Table 2 shows the characteristics of wire polarizers, and Fig. 6 depicts the appearance of a polarizer [20].

Table 2

Technical characteristics of wire polarizers

Substrate material	*ZnSe*	*Ge*	KRS-5
Spectral range, μm	(1.5 – 14)	(8 – 14)	(2 – 30)
Standard aperture, mm	D25 × 25	D25 × 25	D34
Frame size for standard aperture, mm	D42 × 8	D42 × 8	-
Effective transmittance, T_1	65- 70 % with one-sided anti-reflection coating 50 % without coating	>50 % with one-sided anti-reflection coating	60 %
Transmission of unwanted polarization, T_2	<0.1 % for 10 μm	<0.1 % for 10 μm	-
Degree of polarization $(T_1 - T_2)/(T_1 - T_2)$	>99 % for 10 μm	>99 % for 10 μm	
Manufacturer	TYDEX	TYDEX	Edmund Optics

For physical and mathematical simulation of wire polarizers, the period of which is much shorter than the wavelength, the theory of coupled waves is used [16, 19].

a)

b)

Fig. 6. KRS-5 polarizer (a) and phase plate (b) from dmund Optics company [18]

Quarter-wave plate

In [16] demonstrated the possibility of manufacturing and using wire polarizers and wire achromatic phase plates that provide the required extinction ratio and phase delay. Test results of micro polarization superpixel arrays indicate that each element (polarizer and phase plate) is manufactured on its own substrate, as it is too sensitive to crosstalk.

This crosstalk is a consequence of diffraction from the periodic structures of micro polarizers and/or microwave plates. Diffracted light propagates inside the substrate to the next element or into free space. To reduce the effect of this phenomenon on the temperature and spatial separation, it is proposed to integrate micro polarizers into the MRR matrix structure during its manufacture. The birefringent wave plate is manufactured on its own substrate and is compatible with the active zone of the integrated “micro polarizer-pixel” structure. The wave plate must have a two-sided anti-reflection coating. This approach significantly complicates the process of manufacturing the optical-electronic system of PT.

A quarter-wave plate (retarder) can be made in the form of a rhombic prism or a wave plate. Such optical elements are often called compensators, for instance, the Babinet-Soleil compensator. Retarders can be designed for a certain wavelength or for a wide range of the spectrum (achromatic compensators).

Phase retarders based on uniaxial crystals

Changing the phase difference in compensators can be achieved by using anisotropic uniaxial crystals, in which the optical axis is parallel to the crystal faces:

$$\Delta\varphi = \varepsilon = \frac{2\pi}{\lambda} d(n_e - n_o). \quad (8)$$

The optical path difference is due to two parameters: plate thickness d and birefringence $(n_e - n_o)$. For positive crystals $n_e > n_o$. An extraordinary beam with a refractive index n_e is polarized parallel to the optical axis, and an ordinary beam with a refractive index n_o is polarized perpendicular to the optical axis.

The slow axis is the direction in the medium with the highest refractive index n_e, that is, for a uniaxial positive medium it will be its optical axis. *The fast axis* is the direction in the medium with the smallest refractive index n_o.

The most common commercial retarders are quarter-wave and half-wave plates, which provide a phase difference between E_s and E_p components equal to $\pi/2$ and π. A quarter-wave retarder produces circular polarization when the azimuth of linearly polarized incident light makes an angle of 45° with the fast axis. A half-wave retarder forms linearly polarized light, the plane of polarization of which is rotated by an angle of 2θ, when the azimuth of partially polarized incident light is at an angle of θ relative to the fast axis.

IR achromatic retarder

Fig. 7 shows the diagram of operation of a prismatic retarder, in which there is no deviation of the beam [13]. In the optical element, there are two total internal reflections (TIR) at points A_1, B_1 and A_2, B_2 and reflection at the air-metal interface at points C_1, C_2.

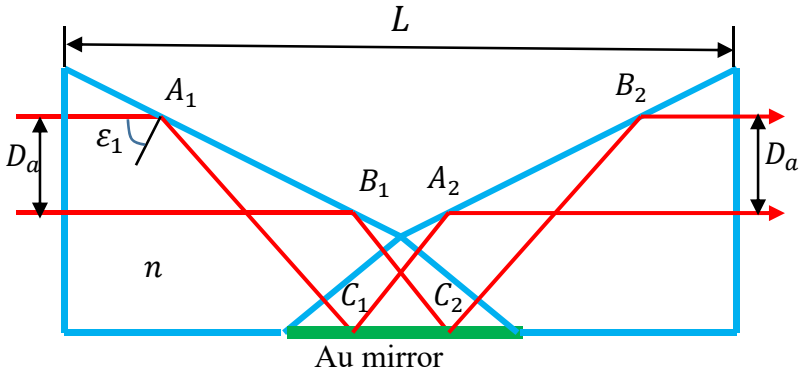

Fig. 7. Infrared achromatic prismatic retarder

The operating principle of the prism is based on the fact that between the plane-polarized components E_s and E_p of the input radiation there are significant phase shifts at TIR points. These phase changes (phase difference) are calculated by the formulae [13]

$$\delta_{pr,s} = 2\text{arctg}\frac{\sqrt{n^2\sin^2\varepsilon_1 - 1}}{n\cos\varepsilon_1}, \tag{9}$$

$$\delta_{pr,p} = 2\text{arctg}\frac{n\sqrt{n^2\sin^2\varepsilon_1 - 1}}{\cos\varepsilon_1}, \tag{10}$$

where ε_1 is the angle of incidence, and n is the refractive index of the prism material (Fig.7).

The linear delay associated with TIR is a net phase shift between the two components E_s and E_p:

$$\Delta_{pr} = \delta_{pr,p} - \delta_{pr,s}. \tag{11}$$

Moreover, phase shifts between E_s and E_p components are observed during reflection from metal:

$$\Delta_{met} = \delta_{met,p} - \delta_{met,s}. \tag{12}$$

Then the total delay for two TIRs and reflection from the metal is equal to

$$\Delta\varphi = 2\Delta_{pr} + \Delta_{met}. \tag{13}$$

The refractive indices of optical materials that transmit radiation well in the IR range of the spectrum are higher than the refractive indices for the visible range. As a rule, for the IR range they are greater than 2.0, and for the visible range they are within (1.4 – 1.7). The higher refractive indices for the IR range result in larger phase delays between the E_s and E_p components for a given angle of incidence than for the visible range. A prismatic retarder for IR radiation, which has more than two TIRs, will have large dimensions, which causes certain difficulties in its application.

Prisms are made from homogeneous materials in which there is no birefringence. Zinc selenide, zinc sulphide, germanium and gallium arsenide satisfy such requirements in the IR range of the spectrum. For the manufacture of mirror surfaces use gold, silver, copper and aluminium. Preference is given to gold, which has a high reflection coefficient in the IR range and significant resistance to corrosion.

The angles of incidence at the entrance and exit of the two prisms were chosen to reduce the Fresnel reflection losses. Table 3 show the parameters of a retarder made of zinc selenium and a gold mirror, which provides a change in the optical length by $\lambda/4$ in the range (8 – 14) μm. The calculation was made or a wavelength of 10 μm [14].

Table 3

Numerical data of an IR achromatic retarder

Wavelength λ, μm	Refractive index ZnSe, n	Refractive index Au, n	Extinction index Au, κ	Total phase delay δ, degree
8	2.418	4.93	57.6	89.91
10	2.407	7.62	71.5	90.02
12	2.394	10.8	85.2	90.04
14	2.378	14.5	98.6	89.98

The use of a subwavelength wire grating leads to the formation of birefringence, which provides the desired phase difference, as well as dispersion, which helps to design an achromatic phase plate [16]. Effective medium theory simulates the subwavelength grating as a thin film with an effective index determined by the grating materials and the polarization of the incident radiation.

For the production of commercial IR retarders, the Edmund Optics company uses wire gratings operating in the zero order of diffraction [20]. Compared to multi-order phase plates, zero-order plates provide increased transmission and lower sensitivity to temperature changes.

These plates are produced with a λ/4 or λ/2 phase delay over a wide spectral range and are ideal for a variety of IR instruments.

The characteristics of a commercial phase plate are given in Table 4, and its appearance is depicted in Fig. 6b.

Table 4

Characteristics of the Edmund Optics phase plate

Delay	λ/4
Spectral range, μm	(3 – 9)
Frame diameter, mm	25.4
Aperture, mm	10
Thickness, mm	8
Phase plate material	Cadmium thiogalate
Transmittance	0.5

Recommendations for choosing IR polarizer and phase plate

The above studies show the following:

1. For practical use in PT, wire polarizers (WP) are primarily suitable, which have a number of advantages compared to polarizers based on Brewster`s reflection law, namely:

- have relatively high transmittance;
- form radiation with a high degree of polarization;
- have small dimensions and weight. The main disadvantages of WP are: considerable chromatic distortion (dispersion); technological complexity of their production, which determines their high cost.

2. Phase plate (retarder) can be made with the use of:

- birefringence, which is problematic for the spectral region (8 – 14) μm;
- the law of total internal reflection and reflection of radiation at the air-metal interface. However, such a phase plate has large overall dimensions, which complicates its use in small-size thermal imagers;
- diffraction of radiation on a wire diffraction grating. Such a diffraction grating of a certain structure provides a phase delay of 90º in a wide spectral range.

3. A promising direction for the creation of PT is the use of MBM, each pixel of which has a wire micro polarizer with a certain orientation of the polarization plane. Four adjacent pixels form a superpixel, which makes it possible to simultaneously determine four parameters of the Stokes vector without using an optical-mechanical scanning system. The use of MBM with micro polarizers has significant advantages:

* absence of an optical-mechanical system for scanning (rotating) a polarizer or a phase plate;

- the ability to simultaneously measure all Stokes parameters in one image frame;
- a simplified electronic system for processing signals from MRR pixels to determine the parameters of the Stokes vector;
- small dimensions of the optical system and low power consumption of the PT.

The main disadvantages of PTs that use MBMs with micro polarizers are:

- technological difficulties of manufacturing such MBMs with micro polarizers and the high cost of such matrices;
- additional image distortions caused by the diffraction of radiation after passing through the diffraction grating and its propagation inside the substrate to the next element.

Conclusions

A deep understanding of the physical processes of infrared radiation transformation in a polarimetric thermal imager allows one to study the optical system of the thermal imager and justify the choice of a polarizer and a phase plate to effectively obtain the polarization characteristics of radiation from the observation object and the background.

It is expedient to use commercial wire polarizers as an infrared polarizer. To conduct laboratory studies of the polarization properties of radiation, Brewster`s law of reflection from a germanium plate can be used.

In polarimetric thermal imagers operating in a wide spectral range, it is necessary to use commercial retarders based on a wire diffraction grating as an infrared achromatic phase plate. An infrared prismatic retarder can be used for experimental research.

A promising direction in the creation of a modern polarimetric thermal imager is the use of a micro bolometric matrix, each pixel of which has a wire micro polarizer with a certain orientation of the polarization plane. Four adjacent pixels form a superpixel, which makes it possible to simultaneously determine the four parameters of the Stokes vector without using an optical-mechanical scanning system.

Further research should be directed to the development of a mathematical model of PT, which would make it possible to calculate the temperature and spatial separation, to substantiate the methods of their increase, which is important for environmental monitoring, monitoring of natural resources, thermal observation systems of wide application [21, 22].

References

1. Anatychuk L. I. (2020). Efficiency criterion of thermoelectric energy converters using waste heat. *J.Thermoelectricity*, 4, 59 - 63.
2. Anatychuk L. I., Havryliuk M. V., Lysko V. V. (2021). Automation and computerization of processes of measuring thermoelectric parameters of materials forming part of generator and cooling thermoelectric modules. *J.Thermoelectricity*, 3, 63 - 70.
3. Vollmer Michael and Mollman Klaus-Peter (2018). *Infrared thermal imaging. Fundamentals, research and applications.* Second Ed. Wiley – VCH, Weinheim, Germany.
4. Tooley R. D. (1990). Man-made target detection using infrared polarization. Polarization considerations for optical systems II. – *International Society for Optics and Photonics*, 1166, 52 - 60.
5. Zhang Y., Shi Z. G., Qiu T. W. (2017). Infrared small target detection method based on decomposition of polarization information. *Journal of Electronic Imaging*, l 33004, №. 1.
6. Tymchik G. S., Kolobrodov V. H., Mykytenko V. I., Sokol B. V. (2020).Temperature resolution of computer-integrated polarization thermal imager. *J. Thermoelectricity*, 4, 22 - 37.
7. Kaplan Herbert (2007). *Practical applications of infrared thermal sensing and imaging equipment.* 3rd ed. SPIE Press (Washington).
8. Yang Bin, Wu Taixia, Chen Wei, Li Yanfei, Knjazhihin Yuri, et al. (2017). Polarization remote sensing physical mechanism, key methods and application. *The International Archives of the Photogrammetry, Remote Sensing and Spatial Information Sciences.* Wuhan, China, XLII-2/W7, 956 - 960.
9. Gurton K. P., Yuffa A. J., Videen G. W. (2014). Enhanced facial recognition for thermal imagery using polarimetric imaging. *Optical Society of America*, 39 (13), 3857 - 3859.
10. Gurton K. P., Felton M. (2012). Remote detection of buried land-mines and IEDs using LWIR polarimetric imaging. *OSA*, 20 (20), 22344 - 22359.
11. Russell A. Chipman, Lam Wai-Sze Tiffany, Garam Young (2019). *Polarized light and optical systems*. Taylor & Francis Group, LLC.

12. Kolobrodov, V. G. (2020). Computer modeling technologies of optical system of polarizing thermal imager. *Visnyk NTUU KPI Seriia - Radiotekhnika Radioaparatobuduvannia*, (83), pp 69 - 74. doi: 10.20535/RADAP.2020.83.69 - 74.
13. Sun Zunyi, Jin Weiqi, Kang Guoguo, Li Li, Yang Jianguo (2022). A temperature-controlled mid-wave infrared polarization radiation source with adjustable degree of linear polarization. *Measurement*, Volume 196, 111210. Doi.org/10.1016/j.measurement.2022.111210.
14. Peterson J., Jensen G. L., Kristi J. A., and Shaw J.A. (2000). Polarimetric imaging using continuously spinning polarizer element. *Proc. SPIE*, 4133, 292 - 300.
15. Goldstein D. H. (2011). *Polarized Light*. Third edition. CRC Press is an imprint of Taylor & Francis Group. London New York.
16. Kemme Shanalyn A. (2006). Micropolarizing device for long wavelength infrared polarization imaging. Sandia National Laboratories. Albuquerque, New Mexico (USA).
17. Yamada Itsunari, Akiyama Tsuoshi. (2019). Infrared wire-grid polarizer with an ultrathin photoimprinted polymer film. *Optical Engineering*, 58(5), 057104, doi: 10.1117/1.OE.58.5.057104.
18. Kolobrodov V. G., Mykytenko V. I., Tymchyk G. S. (2020). Polarization model of thermal contrast observation objects. *J.Thermoelectricity*, 1, 36 - 49.
19. Born M., Wolf E. *Principles of optics. 7th ed*. Cambridge University Press. Wire grid (reflective) polarizers. Retrieved from https://www.edmundoptics.com/c/wire-grid-reflective-polarizers/1337.
20. Globa L., Dovgiy S., Kopiika O. and Kozlov O. (2021). Approach to building uniform information platform for the national automated ecological information and analytical system, In: *CEUR Workshop Proceedings*, 3021, 53 - 65.
21. Globa L., Dovgiy S., Kopiika O. and Kozlov O. Approach to uniform platform development for the ecology digital environment of Ukraine. *Book: Progress in Advanced Information and Communication Technology and Systems*. 83 - 100 DOI: 10.1007/978-3-031-16368-5

Submitted 08.02.2022

Колобродов В. Г., *докт. техн. наук, професор*
Микитенко В. І., *докт. техн. наук, доцент*
Тимчик Г. С., *докт. техн. наук, професор*
Колобродов М.С.

ПІДВИЩЕННЯ ЧУТЛИВОСТІ КОМП'ЮТЕРНО-ІНТЕГРОВАНИХ ТЕПЛОВІЗОРІВ В ДОСЛІДЖЕННЯХ ТЕРМОЕЛЕКТРИЧНИХ ЯВИЩ ТА ДИСТАНЦІЙНИХ СПОСТЕРЕЖЕННЯХ

Робота присвячена обґрунтуванню вибору поляризаційних оптичних елементів для тепловізійних дистанційних спостережень та вимірювань. Виконано порівняльний аналіз основних методів отримання поляризаційних зображень: з допомогою обертання поляризатора, обертання фазової пластинки і з використанням комбінованих матричних приймачів інфрачервоного випромінювання з мікро поляризаторами. Для аналізу використано спрощені математичні моделі перетворення сигналів в основних оптичних елементах поляриметричних тепловізорів – лінійних поляризаторах та фазових (чверть-хвильових) пластинках. Показана перевага дротяних поляризаторів порівняно з поляризаторами на основі відбивання. Також обґрунтовано, що серед різних фізичних ефектів, що викликають фазові затримки - подвійне променезаломлення, повне внутрішнє відбивання і відбивання випромінювання на межі повітря-метал, дифракція на дротяній дифракційній ґратці – найбільш прийнятним є використання останнього ефекту. Бібл. 21, рис. 7.

Ключові слова: поляриметричні тепловізори, вектори Стокса, поляризатор, чверть-хвильова пластинка

References

1. Anatychuk L. I. (2020). Efficiency criterion of thermoelectric energy converters using waste heat. *J.Thermoelectricity*, 4, 59 - 63.
2. Anatychuk L. I., Havryliuk M. V., Lysko V. V. (2021). Automation and computerization of processes of measuring thermoelectric parameters of materials forming part of generator and cooling thermoelectric modules. *J.Thermoelectricity*, 3, 63 - 70.
3. Vollmer Michael and Mollman Klaus-Peter (2018). *Infrared thermal imaging. Fundamentals, research and applications.* Second Ed. Wiley – VCH, Weinheim, Germany.
4. Tooley R. D. (1990). Man-made target detection using infrared polarization. Polarization considerations for optical systems II. – *International Society for Optics and Photonics*, 1166, 52 - 60.
5. Zhang Y., Shi Z. G., Qiu T. W. (2017). Infrared small target detection method based on decomposition of polarization information. *Journal of Electronic Imaging*, l 33004, №. 1.
6. Tymchik G. S., Kolobrodov V. H., Mykytenko V. I., Sokol B. V. (2020).Temperature resolution of computer-integrated polarization thermal imager. *J. Thermoelectricity*, 4, 22 - 37.
7. Kaplan Herbert (2007). *Practical applications of infrared thermal sensing and imaging equipment.* 3rd ed. SPIE Press (Washington).
8. Yang Bin, Wu Taixia, Chen Wei, Li Yanfei, Knjazhihin Yuri, et al. (2017). Polarization remote sensing physical mechanism, key methods and application. *The International Archives of the Photogrammetry, Remote Sensing and Spatial Information Sciences.* Wuhan, China, XLII-2/W7, 956 - 960.
9. Gurton K. P., Yuffa A. J., Videen G. W. (2014). Enhanced facial recognition for thermal imagery using polarimetric imaging. *Optical Society of America*, 39 (13), 3857 - 3859.
10. Gurton K. P., Felton M. (2012). Remote detection of buried land-mines and IEDs using LWIR polarimetric imaging. *OSA*, 20 (20), 22344 - 22359.

11. Russell A. Chipman, Lam Wai-Sze Tiffany, Garam Young (2019). *Polarized light and optical systems*. Taylor & Francis Group, LLC.
12. Kolobrodov, V. G. (2020). Computer modeling technologies of optical system of polarizing thermal imager. *Visnyk NTUU KPI Seriia - Radiotekhnika Radioaparatobuduvannia*, (83), pp 69 - 74. doi: 10.20535/RADAP.2020.83.69 - 74.
13. Sun Zunyi, Jin Weiqi, Kang Guoguo, Li Li, Yang Jianguo (2022). A temperature-controlled mid-wave infrared polarization radiation source with adjustable degree of linear polarization. *Measurement*, Volume 196, 111210. Doi.org/10.1016/j.measurement.2022.111210.
14. Peterson J., Jensen G. L., Kristi J. A., and Shaw J.A. (2000). Polarimetric imaging using continuously spinning polarizer element. *Proc. SPIE*, 4133, 292 - 300.
15. Goldstein D. H. (2011). *Polarized Light*. Third edition. CRC Press is an imprint of Taylor & Francis Group. London New York.
16. Kemme Shanalyn A. (2006). Micropolarizing device for long wavelength infrared polarization imaging. Sandia National Laboratories. Albuquerque, New Mexico (USA).
17. Yamada Itsunari, Akiyama Tsuoshi. (2019). Infrared wire-grid polarizer with an ultrathin photoimprinted polymer film. *Optical Engineering*, 58(5), 057104, doi: 10.1117/1.OE.58.5.057104.
18. Kolobrodov V. G., Mykytenko V. I., Tymchyk G. S. (2020). Polarization model of thermal contrast observation objects. *J.Thermoelectricity*, 1, 36 - 49.
19. Born M., Wolf E. *Principles of optics. 7th ed*. Cambridge University Press. Wire grid (reflective) polarizers. Retrieved from https://www.edmundoptics.com/c/wire-grid-reflective-polarizers/1337.
20. Globa L., Dovgiy S., Kopiika O. and Kozlov O. (2021). Approach to building uniform information platform for the national automated ecological information and analytical system, In: *CEUR Workshop Proceedings*, 3021, 53 - 65.
21. Globa L., Dovgiy S., Kopiika O. and Kozlov O. Approach to uniform platform development for the ecology digital environment of Ukraine. *Book: Progress in Advanced Information and Communication Technology and Systems*. 83 - 100 DOI: 10.1007/978-3-031-16368-5

Submitted 08.02.2022

DOI: 10.63527/1607-8829-2022-1-82-92

S. O. Filin, *dok. techn sciences*
Wiktor Wiśniewski

West Pomeranian University of Technology,
Szczecin al. Piastow 17, Szczecin, 70-310, Poland;
e-mail: sergiy.filin@zut.edu.pl

THERMOELECTRIC REFRIGERATOR FOR SLEEPING CAR COMPARTMENTS

In this article, a thermoelectric refrigerator's design was presented, the cooling unit of which is integrated into a corner cabinet in the sleeping car compartment of PKP Intercity model 308A. The design of the cooling unit provides for several execution options. The refrigerator has an innovative two-level power supply system, which allows reducing energy consumption. The refrigerator cabinet is divided into two chambers "serving" two adjacent compartments. The thermoelectric unit of the refrigerator cools both chambers simultaneously. The application of the invention allows increasing the comfort level of rail transport passengers. Bibl. 11, Fig. 9, Table 1.
Key words: thermoelectric transport refrigerator, two-level power supply system, thermoelectric unit.

Introduction

The research presented in the article shows the solution that may be used to improve the comfort of passengers travelling in sleeping cars, as a rule, in the period from April to October. For several years, a significant warming of the climate has been observed [1]. This leads to higher temperatures during warm periods (e.g. summer period in Europe). That fact influences the train passengers' need to store chilled drinks or food, flowers or temperature-sensitive medicines during the trip. Possibility to sore these goods will increase the comfort of passengers traveling on longer routes, as well as contribute to raising the standards of passenger transportation in these compartments. Modern trends in the development of the use of thermoelectric coolers in transport are described in detail in the subject literature [2], [3]. Among the new applications, it is worth noting the bar with a thermoelectric coolers installed on board the Boeing-747 (Fig. 1).

A thermoelectric cooler is considered to be the most rational solution among other coolers used in vehicles, due to the numerous advantages of this cooling method [4]. One of the advantages of its implementation in transport means is the possibility to adjust the power supply voltage of the thermoelectric unit to the voltage applied in networks of railway cars, and the use of modern methods of two-level temperature regulation in thermoelectric coolers [5]. All this allows avoiding the use of complex, unreliable and expensive energy systems [4].

Fig. 1. Thermoelectric cooler in the bar of the Boeing-747 aircraft [2]

A particularly advantageous place for locating a thermoelectric cooler in a compartment is a cabinet (ordinary or corner), placed above the sink (Fig. 2).

Fig.2. Triple sleeping compartments for cars 305Ab (left) and 308A (right)

A cooler designed in this way, as compared to the solution of installing refrigerators in each compartment separately, i.e. without a specially allocated place [6], is a rational solution for compartments, because it does not reduce the usable area, is characterized by a lower cost of implementation and a lower energy consumption.

General information about sleeping cars manufactured in Poland

The sleeping compartment for a 305Ab car, manufactured at the *Zakłady Cegielskiego* factory in Poznan since 2004, as well as sleeping compartments of other models, are equipped, among other things, with three beds, a wash basin and a single-door cabinet with a wooden housing (Fig. 2). This cabinet has internal dimensions 49 x 17.5 x 59 mm (width x depth x height), is equipped with a lock with a ball latch, in the middle of the back wall there is a mirror, on the top wall – a lighting lamp, on the side wall there is an electric socket for connecting a razor. The interior space of the cabinet is divided by a horizontal shelf. The conductor, before the start of the trip, usually puts into it, for example, uncooled mineral water (a 0.5 l PET bottle for each passenger), a roll or a hygiene kit (towel + soap). There is no refrigerator in the compartment, the only refrigerator in the car is located in the conductor's compartment and is not available for direct use by passengers. The same applies to restaurant cars, where the refrigerator is built into the kitchen section [7].

A more modern sleeping car, for which the refrigerator's design was proposed, is a sleeping car model 308A. In 2013, the PKP Intercity company signed a contract for the implementation of the project called «Upgrading of PKP Intercity rolling stock Przemyśl – Szczecin - Stage II». Modernization of 10 sleeping cars was ordered, and the execution was entrusted to company PESA from the city of Bydgoszcz. The first car was put on the test tracks in 2015 (Fig. 3).

Fig.3. Sleeping car model 308A
at the railway station Szczecin Główny

Moreover, within the mentioned project the cars manufactured in 1977-1981 were modernized. This tender also included the installation of new bogies for the cars. New strollers of the type 39AN were installed that were without pneumatic cushion on flexible springs. In addition, a sliding door was installed in the car. The sleeping car has 9 public compartments and one compartment for the conductor. Each compartment has 3 (folding) beds, located horizontally, one above the other [8]. This is a typical range of the middle-class sleeping compartments. 3 passengers being seating in a space of about 8 m^3 deal with a high density which causes an additional increase in temperature in the compartment. A comparison of selected transport means is presented in Table.

Table

The density of people per cubic meter of the car

Transport means	**Type (model)**	**Number of persons in a cabin (incl. crew)**	**Interior dimensions (approximate), m**	**Interior volume, m^3**	**Density, persons/m^3**
Aircraft	Boeing 737-700	126 (4)	20x5x1.8	200	0.63
Autocar	Setra 500	69 (2)	13.5x2.4x2.8	90.7	0.76
Railway	308A Entire car	28 (2)	24.5x2.9x4.2	298.41	0.094
	Triple compartment	3	1.66x1.94x2.5	8.051	0.372

As can be seen from Table 1, the density of people per cubic meter in a fully equipped compartment of a railway car is more seven times lower for the whole car compared to air or bus transport and for a single sleeping compartment is almost half that of air or bus transport, which brings additional advantages, namely: greater safety during the coronavirus pandemic. A smaller number of people per cubic meter accordingly reduces the probability of infection, for example, with the SARS-CoV-2 virus or any other virus.

Another fact is in favour of the railway transport: CO_2 emissions per passenger are only 24 g/km. [9] This is more than 3 times less than in road transport (102 g/km) and about 10 times less than an air transport (244 g/km).

The modernization of a railway car 308 A included, among other things, its adaptation for the transportation of people with disabilities; one special compartment for two people with a toilet was adapted for wheelchair users. A manual ramp on the side of this compartment enabled a wheelchair user to enter a railway car 308 A [8].

Description of the refrigerator and the design option choice

The two-chamber thermoelectric refrigerator for a railway car model 305Ab was designed in several versions, which differed in the location of the unit (on the side or on top of refrigerator) and

the orientation of the partition (e.g., longitudinal, that is, parallel to the wall separating the two compartments of the car, or transverse – perpendicular to this wall).

In the first version, the refrigerator is placed in the hole of wall 1 that divides the adjacent compartments of the railway car, near the outer wall 2 of the car, from which it is separated by an air duct 3 (Fig. 4a). Inside the refrigerator there is a partition 3-4 mm thick, made of plastic, located along wall 1. Partition 4 divides the internal space of the refrigerator into two chambers of equal volume. Access to separate chambers in each compartment of the car is possible due to the doors 5 and 5'. Walls 6 of the refrigerator contain heat-insulating material inside. The cooling unit consists of a cold heat sink 7, transitional elements 8 and 9 made of aluminium, a thermoelectric module 10, a hot heat sink 11 with a cover 12 and a fan 13. The unit and, in particular, heat sink 7, are located symmetrically in relation to the surface of partition 4, which ensures cooling of both chambers with the same cooling capacity. On the one hand, partition 4 is placed between the fins of the cold heat sink (as shown in Fig. 4), which provides additional stability of its position and facilitates the assembly of the refrigerator.

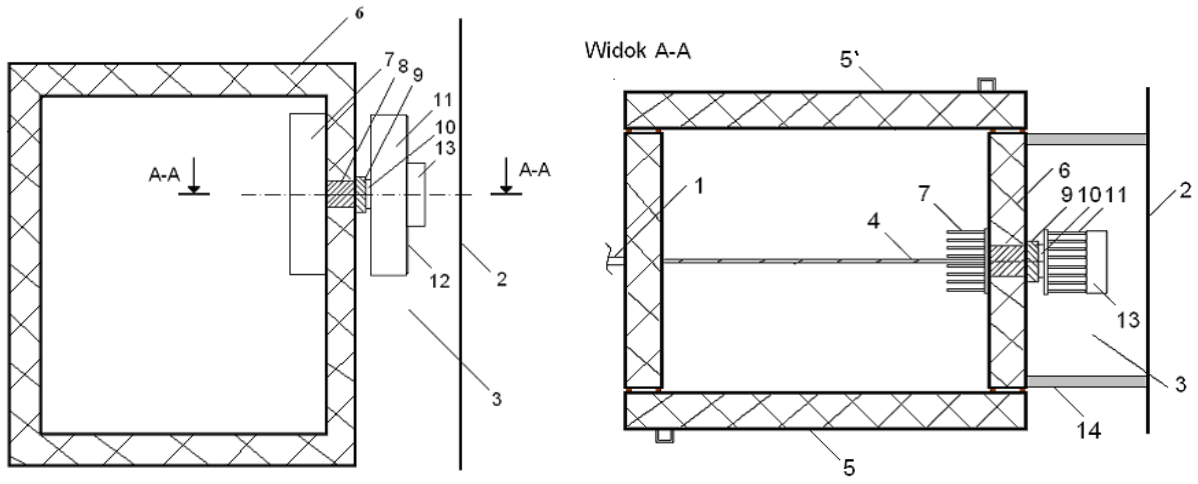

a *b*

Fig.4. Schematic drawing of a two-chamber thermoelectric refrigerator for a car 305Ab [10] with a lateral arrangement of the unit and a longitudinal partition: 1 – intercompartment wall, 2 – outer wall of the car, 3 – air duct, 4 - partition, 5, 5` - doors, 6 – fixed walls of the refrigerator, 7 – cold heat sink, 8, 9 – transition element, 10 - module, 11 – hot heat sink, 12 - cover, 13 - fan, 14 – duct wall

In another version of designed refrigerator, the unit is placed in the upper wall of the body (Fig. 5). The partition 4 is installed perpendicular to wall 1, which divides the compartments of the railway car; this way two chambers are created. Partition 4 has a thickness of 2-3 mm. The dimensions of the doors are adapted to the dimensions of the chambers. In this version, heat dissipates from the hot heat sink into the space above the refrigerator, which is isolated from the compartment of the railway car and connects to the ventilation channel of the car passing under its ceiling. To increase the useful capacity of the chambers, the fins of the heat sink 7 are installed in the recess made in the upper wall, as shown in Fig. 5.

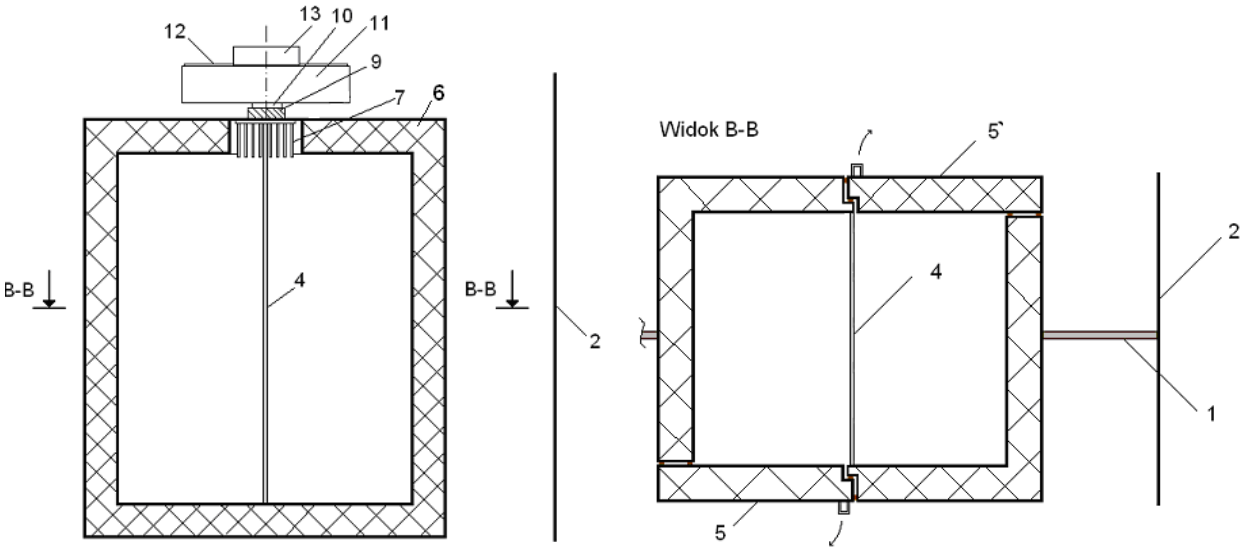

Fig. 5. Schematic drawing of a two-chamber thermoelectric refrigerator for a car 305Ab [10] with the upper arrangement of the unit and a longitudinal partition. Positions as in Fig. 4

The corner cabinet in the sleeping compartment of a car 308A has 3 shelves. After removing the upper shelf (Fig. 6, yellow arrow), the space formed between the ceiling and the lower shelf can be used as a chamber for thermoelectric refrigerator.

Fig.6. Corner cabinet in a compartment of a car 308A

When placing the unit near the partition of the compartment at the level of the luggage shelf, it is necessary to isolate it from the luggage and thus provide additional protection of the unit. This problem can be avoided by removing the middle shelf instead of the top one. Then the hot side of the unit will be placed in the space between the upper shelf and the ceiling of the cabinet.

The corner cabinet after inserting the partition and making the structural changes shown in Fig. 7, has the following internal dimensions:

- width: 260 mm (obtained by adding a replaceable partition);
- height: 340 mm (after removing the middle shelf and raising the upper one);
- depth: 200 mm (averaged from the two bases of the trapezoid).

The cabinet designed in this way can accommodate a 1.5-liter bottle.

By replacing the wall between the compartments with the intercompartment partition, an increase in the volume of the refrigerating chamber may be obtained. The graphic comparison of two options is shown in Fig. 7. Due to the very low probability of opening both doors of the refrigerator at the same time, the proposed solution does not impair the sound isolation between adjacent car compartments.

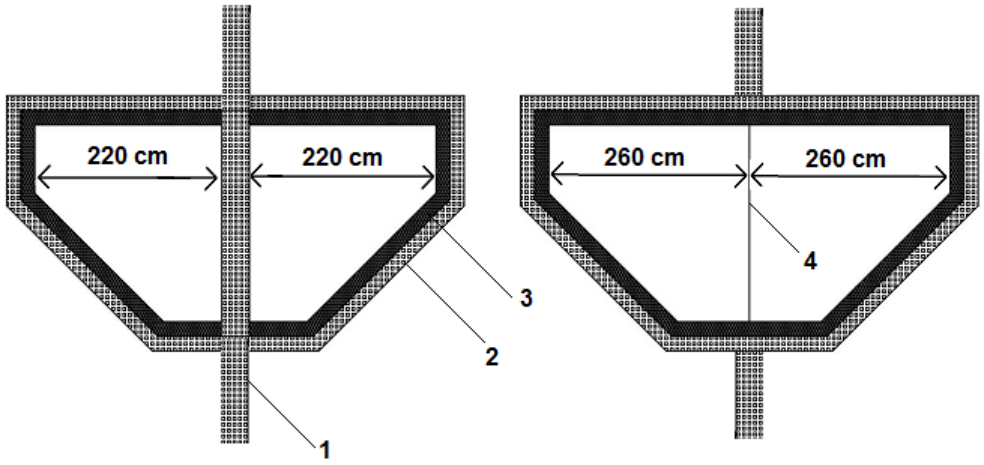

Fig.7. Comparison of the width of the refrigerating chamber:
a – without a hole in the intercompartment wall of the car, b – with the use of intercompartment partition:
1 - partition, 2 – furniture board, 3 – thermal insulation,
4 – intercompartment partition

In case the thermoelectric unit is located on the upper shelf of the corner cabinet, it is necessary to reduce the height of the cabinet doors, in order to obtain better air circulation that cools the hot heat sink of the unit.

Figs. 8 and 9 present fragments of a thermoelectric refrigerator design for the car compartment of the model 308A. The calculated value of the thermal load of one refrigerating chamber in this version was 11.5 W. Within the framework of the project [11], the type of thermoelectric module was chosen, the necessary heat exchange surfaces of heat exchangers were calculated under the accepted operating conditions of the refrigerator.

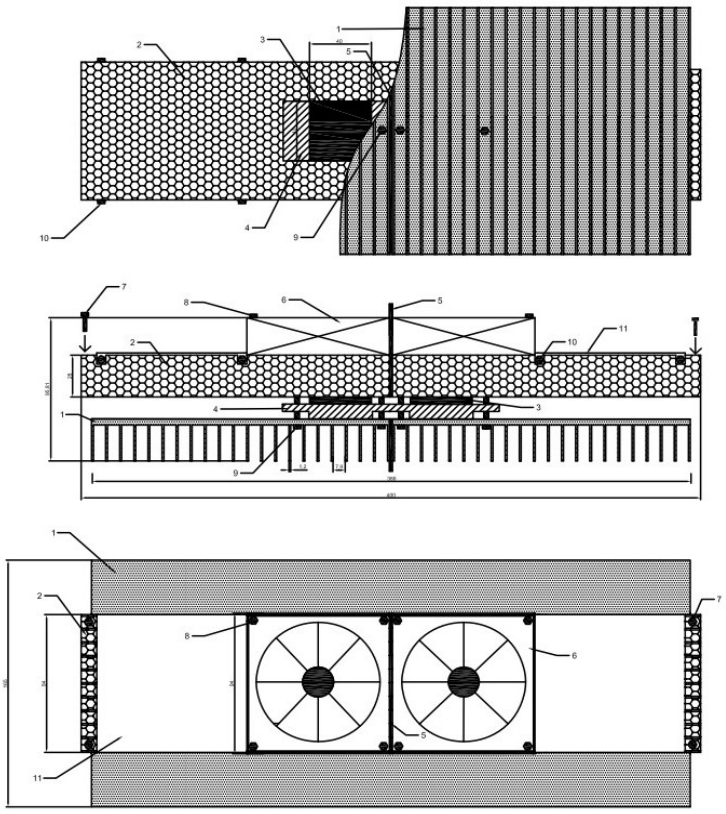

Fig.8. Unit of a two-chamber thermoelectric refrigerator for a car 308A [11]:
1 – cold side heat exchanger, 2 – hot side heat exchanger, 3 – thermoelectric module; 4 – transition element, 5 –partition, 6 – fan, 7, 8, 9 – screws, 10 – thermal insulation, 11 – cabinet wall

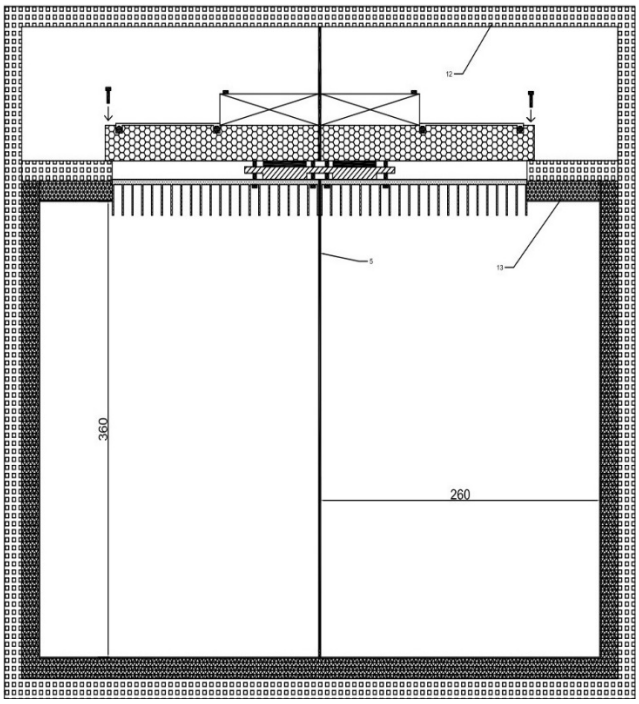

Fig. 9. Vertical section of the refrigerator for a car 308A.
Positions as in Fig. 8

Conclusions

1. The global trend of increasing travel comfort is observed, especially when traveling using rail transport over long distances. Therefore, it is important to provide passengers with the opportunity to use a refrigerator in sleeping compartment.
2. The use of a thermoelectric cooler may be the rational solution to equip the compartments with the cooling devices.
3. The article presents several versions of the design of thermoelectric refrigerator that may be used to cool products in adjacent compartments of railway car.
4. The research results may be of interest to producers of thermoelectric refrigerators and railway cars, who may consider implementation of the proposed solutions.

References

1. Climate warming accelerates (Ocieplanie klimatu przyspiesza). No limits, 1, 2020, pp.16 - 25 (in Polish), https://us.edu.pl/no-limits-ocieplanie-klimatu-przyspiesza/ (Accessed: 28.08.2021).
2. Pierwsza klasa w Emirates deklasuje konkurencję, https://mrluxury.pl/2017/12/29/pierwsza-klasa-emirates-deklasuje-konkurencje/ (Accessed: 28.08.2021).
3. Jasińska B., Filin S. Economical transport thermoelectric refrigerators with two-level temperature control: the experience of creation and test results. *J. Thermoelectricity*, 3, 2015, 38 - 44.
4. Fairbanks J. W. Thermoelectric Applications Review. European Thermoelectric Conference. Odessa, Ukraine, September 10 - 13, 2007, https://ect2007.thermion-company.com/ect2007.its.org/system/files/u1/pdf/10.pdf (Accessed: 20.09.2021).
5. Filin S., Owsicki A. Principles of design and operation of thermoelectric refrigerators (Zasady projektowania i eksploatacji chłodziarek termoelektrycznych). ZAPOL, Szczecin, 2010 (in Polish).
6. Filin S., Jasińska B., Zakrzewski B., Chmielowski M. Patent RP no. 224189. Way to reduce energy consumption of thermoelectric refrigerator and thermoelectric refrigerator (Sposób redukcji zużycia energii przez chłodziarkę termoelektryczną i chłodziarka termoelektryczna), Published 06.12.2016 (in Polish).
7. Railway dining car. Patent GB 224461 B61D37/00, 13.11.1924.
8. https://bazawagonow.pl/308A.html (Accessed: 20.09.2021).
9. PKP z dumą informuje, że mniej truje. Samochód konta pociąg - sprawdź teraz różnicę w emisji CO_2 (spidersweb.pl) (Accessed: 02.06.2021).
10. Filin S., Zakrzewski B. Patent RP nr 217390. Publ. 08.08.2014. Wagon especially sleeping, equipped with thermoelectric refrigerator.
11. Wiśniewski W. Design of a thermoelectric refrigerator for sleeping compartments of railway carriages. (Projekt chłodziarki termoelektrycznej dla przedziałów sypialnych wagonów kolejowych). Bachelor Diploma Project, West Pomeranian University of Technology in Szczecin, Szczecin, 2021.

Submitted 01.03.2022

Філін С.О., доктор техн. наук
Вишнівський Віктор

Західньопоморський технологічний університет у Щецині
алея Піастів 17, Щецін, 70-310, Польща;
e-mail: sergiy.filin@zut.edu.pl

ТЕРМОЕЛЕКТРИЧНИЙ ХОЛОДИЛЬНИК ДЛЯ КУПЕ СПАЛЬНИХ ВАГОНІВ

У цій статті представлено конструкцію термоелектричного холодильника, холодильний агрегат якого інтегрований в кутову шафу в спальному купе вагона PKP Intercity моделі 308A. Конструкція холодильного агрегату передбачає кілька варіантів виконання. Холодильник має інноваційну дворівневу систему живлення, що дозволяє зменшити споживання енергії. Холодильна шафа розділена на два відділення, які «обслуговують» два сусідніх купе. Термоелектричний блок холодильника охолоджує обидві камери одночасно. Застосування винаходу дозволяє підвищити комфорту пасажирів залізничного транспорту. Бібл. 11, рис. 9, табл. 1.

Ключові слова: транспортний термоелектричний охолоджувач, дворівнева система живлення, термоелектрична установка.

References

1. Climate warming accelerates (Ocieplanie klimatu przyspiesza). No limits, 1, 2020, pp.16 - 25 (in Polish), https://us.edu.pl/no-limits-ocieplanie-klimatu-przyspiesza/ (Accessed: 28.08.2021).
2. Pierwsza klasa w Emirates deklasuje konkurencję, https://mrluxury.pl/2017/12/29/pierwsza-klasa-emirates-deklasuje-konkurencje/ (Accessed: 28.08.2021).
3. Jasińska B., Filin S. Economical transport thermoelectric refrigerators with two-level temperature control: the experience of creation and test results. *J. Thermoelectricity*, 3, 2015, 38 - 44.
4. Fairbanks J. W. Thermoelectric Applications Review. European Thermoelectric Conference. Odessa, Ukraine, September 10 - 13, 2007, https://ect2007.thermion-company.com/ect2007.its.org/system/files/u1/pdf/10.pdf (Accessed: 20.09.2021).
5. Filin S., Owsicki A. Principles of design and operation of thermoelectric refrigerators (Zasady projektowania i eksploatacji chłodziarek termoelektrycznych). ZAPOL, Szczecin, 2010 (in Polish).
6. Filin S., Jasińska B., Zakrzewski B., Chmielowski M. Patent RP no. 224189. Way to reduce

energy consumption of thermoelectric refrigerator and thermoelectric refrigerator (Sposób redukcji zużycia energii przez chłodziarkę termoelektryczną i chłodziarka termoelektryczna), Published 06.12.2016 (in Polish).

7. Railway dining car. Patent GB 224461 B61D37/00, 13.11.1924.
8. https://bazawagonow.pl/308A.html (Accessed: 20.09.2021).
9. PKP z dumą informuje, że mniej truje. Samochód konta pociąg - sprawdź teraz różnicę w emisji CO_2 (spidersweb.pl) (Accessed: 02.06.2021).
10. Filin S., Zakrzewski B. Patent RP nr 217390. Publ. 08.08.2014. Wagon especially sleeping, equipped with thermoelectric refrigerator.
11. Wiśniewski W. Design of a thermoelectric refrigerator for sleeping compartments of railway carriages. (Projekt chłodziarki termoelektrycznej dla przedziałów sypialnych wagonów kolejowych). Bachelor Diploma Project, West Pomeranian University of Technology in Szczecin, Szczecin, 2021.

Submitted 01.03.2022

ARTICLE SUBMISSION GUIDELINES

For publication in a specialized journal, scientific works are accepted that have never been printed before. The article should be written on an actual topic, contain the results of an in-depth scientific study, the novelty and justification of scientific conclusions for the purpose of the article (the task in view).

The materials published in the journal are subject to internal and external review which is carried out by members of the editorial board and international editorial board of the journal or experts of the relevant field. Reviewing is done on the basis of confidentiality. In the event of a negative review or substantial remarks, the article may be rejected or returned to the author(s) for revision. In the case when the author(s) disagrees with the opinion of the reviewer, an additional independent review may be done by the editorial board. After the author makes changes in accordance with the comments of the reviewer, the article is signed to print.

The editorial board has the right to refuse to publish manuscripts containing previously published data, as well as materials that do not fit the profile of the journal or materials of research pursued in violation of ethical norms (for instance, conflicts between authors or between authors and organization, plagiarism, etc.). The editorial board of the journal reserves the right to edit and reduce the manuscripts without violating the author's content. Rejected manuscripts are not returned to the authors.

Submission of manuscript to the journal

The manuscript is submitted to the editorial office of the journal in paper form in duplicate and in electronic form on an electronic medium (disc, memory stick). The electronic version of the article shall fully correspond to the paper version. The manuscript must be signed by all co-authors or a responsible representative.

In some cases it is allowed to send an article by e-mail instead of an electronic medium (disc, memory stick).

English-speaking authors submit their manuscripts in English. Russian-speaking and Ukrainian-speaking authors submit their manuscripts in English and in Russian or Ukrainian, respectively. Page format is A4. The number of pages shall not exceed 15 (together with References and extended abstracts). By agreement with the editorial board, the number of pages can be increased.

To the manuscript is added:

1. Official recommendation letter, signed by the head of the institution where the work was carried out.

2. License agreement on the transfer of copyright (the form of the agreement can be obtained from the editorial office of the journal or downloaded from the journal website – Dohovir.pdf). The license agreement comes into force after the acceptance of the article for publication. Signing of the license agreement by the author(s) means that they are acquainted and agree with the terms of the agreement.

3. Information about each of the authors – full name, position, place of work, academic title, academic degree, contact information (phone number, e-mail address), ORCID code (if available). Information about the authors is submitted as follows:

authors from Ukraine - in three languages, namely Ukrainian, Russian and English;

authors from the CIS countries - in two languages, namely Russian and English;

authors from foreign countries – in English.

4. Medium with the text of the article, figures, tables, information about the authors in electronic form.

5. Colored photo of the author(s). Black-and-white photos are not accepted by the editorial staff. With the number of authors more than two, their photos are not shown.

Requirements for article design

The article should be structured according to the following sections:

- *Introduction*. Contains the problem statement, relevance of the chosen topic, analysis of recent research and publications, purpose and objectives.
- *Presentation of the main research material* and the results obtained.
- *Conclusions* summing up the work and the prospects for further research in this direction.
- *References*.

The first page of the article contains information:

1) in the upper left corner – UDC identifier (for authors from Ukraine and the CIS countries);

2) surname(s) and initials, academic degree and scientific title of the author(s);

3) the name of the institution where the author(s) work, the postal address, telephone number, e-mail address of the author(s);

4) article title;

5) abstract to the article – not more than 1 800 characters. The abstract should reflect the consistent logic of describing the results and describe the main objectives of the study, summarize the most significant results;

6) key words – not more than 8 words.

The text of the article is printed in Times New Roman, font size 11 pt, line spacing 1.2 on A4 size paper, justified alignment. There should be no hyphenation in the article.

Page setup: "mirror margins" – top margin – 2.5 cm, bottom margin – 2.0 cm, inside – 2.0 cm, outside – 3.0 cm, from the edge to page header and page footer – 1.27 cm.

Graphic materials, pictures shall be submitted in color or, as an exception, black and white, in .opj or .cdr formats, .jpg or .tif formats being also permissible. According to author's choice, the tables and partially the text can be also in color.

Figures are printed on separate pages. The text in the figures must be in the font size 10 pt. On the charts, the units of measure are separated by commas. Figures are numbered in the order of their arrangement in the text, parts of the figures are numbered with letters – a, b, .. On the back of the figure, the title of the article, the author (authors) and the figure number are written in pencil. Scanned images and graphs are not allowed to be inserted.

Tables are provided on separate pages and must be executed using the MSWord table editor. Using pseudo-graph characters to design tables is inadmissible.

Formulae shall be typed in Equation or MatType formula editors. Articles with formulae written by hand are not accepted for printing. It is necessary to give definitions of quantities that are first used in the text, and then use the appropriate term.

Captions to figures and tables are printed in the manuscript after the references.

Reference list shall appear at the end of the article. References are numbered consecutively in the order in which they are quoted in the text of the article. References to unpublished and unfinished works are inadmissible.

Attention! In connection with the inclusion of the journal in the international bibliographic abstract database, the reference list should consist of two blocks: CITED LITERATURE and REFERENCES (this requirement also applies to English articles):

CITED LITERATURE – sources in the original language, executed in accordance with the

Ukrainian standard of bibliographic description DSTU 8302:2015. With the aid of VAK.in.ua (http://vak.in.ua) you can automatically, quickly and easily execute your "Cited literature" list in conformity with the requirements of State Certification Commission of Ukraine and prepare references to scientific sources in Ukraine in understandable and unified manner. This portal facilitates the processing of scientific sources when writing your publications, dissertations and other scientific papers.

REFERENCES – the same cited literature list transliterated in Roman alphabet (recommendations according to international bibliographic standard APA-2010, guidelines for drawing up a transliterated reference list "References" are on the site http//www.dse.org.ua, section for authors).

To speed up the publication of the article, please adhere to the following rules:

- in the upper left corner of the first page of the article – the UDC identifier;
- family name and initials of the author(s);
- academic degree, scientific title;

begin a new line, Times New Roman font, size 12 pt, line spacing 1.2, center alignment;

- name of organization, address (street, city, zip code, country), e-mail of the author(s);

begin a new line 1 cm below the name and initials of the author(s), Times New Roman font, size 11 pt, line spacing 1.2, center alignment;

- the title of the article is arranged 1 cm below the name of organization, in capital letters, semi-bold, font Times New Roman, size 12 pt, line spacing 1.2, center alignment. The title of the article shall be concrete and possibly concise;
- the abstract is arranged 1 cm below the title of the article, font Times New Roman, size 10 pt, in italics, line spacing 1.2, justified alignment in Ukrainian or Russian (for Ukrainian-speaking and Russian-speaking authors, respectively);
- key words are arranged below the abstract, font Times New Roman, size 10 pt, line spacing 1.2, justified alignment. The language of the key words corresponds to that of the abstract. Heading "Key words" - font Times New Roman, size 10 pt, semi-bold;
- the main text of the article is arranged 1 cm below the abstract, indent 1 cm, font Times New Roman, size 11 pt, line space spacing 1.2, justified alignment;
- formulae are typed in formula editor, fonts Symbol, Times New Roman. Font size is "normal" – 12 pt, "large index" – 7 pt, "small index" – 5 pt, "large symbol" – 18 pt, "small symbol" – 12 pt. The formula is arranged in the text, center aligned and shall not occupy more than 5/6 of the line width, formulae are numbered in parentheses on the right;
- dimensions of all quantities used in the article are represented in the International System of Units (SI) with the explication of the symbols employed;
- figures are arranged in the text. The figures and pictures shall be clear and contrast; the plot axes – parallel to sheet edges, thus eliminating possible displacement of angles in scaling; figures are submitted in color, black-and-white figures are not accepted by the editorial staff of the journal;
- tables are arranged in the text. The width of the table shall be 1 cm less than the line width. Above the table its ordinary number is indicated, right alignment. Continuous table numbering throughout the text. The title of the table is arranged below its number, center alignment;

• references should appear at the end of the article. References within the text should be enclosed in square brackets behind the text. References should be numbered in order of first appearance in the text. Examples of various reference types are given below.

Examples of LITERATURE CITED

Journal articles

Anatychuk L.I., Mykhailovsky V.Ya., Maksymuk M.V., Andrusiak I.S. Experimental research on thermoelectric automobile starting pre-heater operated with diesel fuel. *J.Thermoelectricity*. 2016. №4. P.84–94.

Books

Anatychuk L.I. *Thermoelements and thermoelectric devices. Handbook.* Kyiv, Naukova dumka, 1979. 768 p.

Patents

Patent of Ukraine № 85293. Anatychuk L.I., Luste O.J., Nitsovych O.V. Thermoelement.

Conference proceedings

Lysko V.V. *State of the art and expected progress in metrology of thermoelectric materials.* Proceedings of the XVII International Forum on Thermoelectricity (May 14-18, 2017, Belfast). Chernivtsi, 2017. 64 p.

Authors' abstracts

Kobylianskyi R.R. *Thermoelectric devices for treatment of skin diseases*: extended abstract of candidate's thesis. Chernivtsi, 2011. 20 p.

Examples of REFERENCES

Journal articles

Gorskiy P.V. (2015). Ob usloviakh vysokoi dobrotnosti i metodikakh poiska perspektivnykh sverhreshetochnykh termoelektricheskikh materialov [On the conditions of high figure of merit and methods of search for promising superlattice thermoelectric materials]. *Termoelektrichestvo - J.Thermoelectricity,* 3, 5 – 14 [in Russian].

Books

Anatychuk L.I. (2003). *Thermoelectricity. Vol.2. Thermoelectric power converters*. Kyiv, Chernivtsi: Institute of Thermoelectricity.

Patents

Patent of Ukraine № 85293. Anatychuk L. I., Luste O.Ya., Nitsovych O.V. Thermoelements [In Ukrainian].

Conference proceedings

Rifert V.G. Intensification of heat exchange at condensation and evaporation of liquid in 5 flowing-down films. In: *Proc. of the 9th International Conference Heat Transfer.* May 20-25, 1990, Israel.

Authors'abstracts

Mashukov A.O. *Efficiency hospital state of rehabilitation of patients with color carcer.* PhD (Med.) Odesa, 2011 [In Ukrainian].